Phonon thermodynamics and elastic behavior of GaN and GaAs at high temperatures and pressures

Thesis by
Jane E. Herriman

In Partial Fulfillment of the Requirements for the
Degree of
Doctor of Philosophy

CALIFORNIA INSTITUTE OF TECHNOLOGY
Pasadena, California

2020
Defended February 14, 2020

Jane E. Herriman
ORCID: 0000-0003-4769-1403

for my parents,
who drove tens of thousands of miles for my education

ACKNOWLEDGEMENTS

I've been tremendously fortunate in the amount and quality of support I've received over the last several years as a graduate student. The traversal I took through graduate school was far from linear, and the encouragement, insights, and guidance I received from many others at various junctures helped inform the decisions I made. I'm happy with where I now am, and so I find myself grateful to many people.

First, I'm thankful to have been mentored by my advisor, Brent Fultz. He is gentle, thoughtful, and obviously invested in his students' well-being and professional development. He has been consistently supportive of my academic and career decisions, even as they became increasingly unconventional and involved leaving Caltech for LLNL and a startup. He had a lot of opportunities to say "no" and he never did. He always supported me, ultimately letting my decisions be mine.

Multiple transitions I made were made smoother by the support of the DOE SCGF staff, especially Ping Ge, and the folks with CDAC, especially Steve Gramsch. I feel like I wouldn't have gotten very far without Olle Hellman, who helped me through conceptually tough terrain while I camped out in his office. Through him I met Nina Shulumba, who offered not only guidance but energy and enthusiasm that was hard to match. I'd furthermore like to thank everyone in the Fultz group for their help, particularly Lisa Mauger and Sally June Tracy, who included me in their research and taught me the ropes early on, and to the technical support staff at Livermore Computing and NERSC who provided excellent service, especially Rebecca Hartman-Baker.

I'm grateful to have had the opportunity to spend the last few years of my Ph.D. at LLNL. I'm particularly grateful to Erik Draeger and Becky Springmeyer, who have facilitated my stay at the lab and provided support in various ways, and Xavier Andrade, who helped me learn more about scientific software development.

Of course, I never would have ended up in graduate school in the first place if it weren't for a few excellent teachers along the way who taught me to enjoy science — most notably my high school chemistry and physics teachers, Ms. Webb and Mrs. Macaulay, and one of my college chemistry professors, Karen Stump.

A defense wouldn't be a defense without its committee members. Thank you to Jennifer Jackson, who took me to Argonne National Lab with her group on multiple experiments; Keith Schwab, who I enjoyed working with as his TA for solid state

physics; Bill Johnson, who taught me thermodynamics; and Alfredo Correa, my current mentor at LLNL.

There are many more family, friends, administrators, and teachers who smoothed the way — especially during times of duress — more than I can say. Many of my days were brightened by Logan Brown, Viki Chernow, Heather Duckworth, Emel Hajjem, and Carlos Laguna. I am especially grateful for the support of Candice Yono, Sacha Verweij, and Linnea Larson. Thank you all!

ABSTRACT

The work herein studies how high temperatures and pressure impact the properties of four materials: two phases of Gallium Nitride (GaN) and two phases of Gallium Arsenide (GaAs). The particular phases we study are the wurtzite and zinc blende phases of each chemical composition. The *properties* we study concern (1) the phonon thermodynamics and (2) the elastic behavior. In particular, phonons were calculated at simultaneously elevated temperature and pressure, and elastic constants were calculated as functions of pressure at 0 K.

Our studies of phonon thermodynamics included comparing the results of phonon calculations accounting for full temperature effects to the results of a quasiharmonic approximation (QHA) for each material, allowing us to assess the importance of explicitly anharmonic contributions to the phonons with changing temperature and pressure. In GaN, the QHA gave reasonable results for the temperature dependence of the phonon DOS at zero pressure, but unreliably predicted the combined effects of temperature and pressure. Pressure was found to change the explicit anharmonicity, altering the thermal shifts of phonons, and more notably qualitatively changing the evolution of phonon lifetimes with increasing temperature. These effects were largest for the optical modes, and phonon frequencies below approximately 5 THz were adequately predicted with the QHA. In GaAs, the QHA failed to account for temperature-induced phonon frequency shifts at all pressures. As in GaN, the QHA was not able to predict the combined effects of temperature and pressure. In GaAs, the QHA clearly became less reliable with elevated pressure. In particular, the number of three-phonon processes increased with pressure, thereby increasing the temperature-driven broadening of phonon spectral lineshapes.

So, why did pressure change the possible three-phonon processes in both GaN and GaAs, but cause them to net increase in GaAs? In all materials, the frequencies of phonon branches were sensitive to pressure to varying degrees. Showing the greatest contrast, transverse acoustic modes in all four materials softened with increasing pressure, whereas all other modes stiffened, albeit at different rates. If the frequencies of all modes scaled uniformly with pressure, we might expect that phonon decay channels consisting of equivalent input and output total phonon frequencies would persist independent of pressure; non-uniform frequency scaling, however, destroys some phonon decay channels and creates others in order to conserve energy. The dissimilar atomic masses of Ga and N create a phonon bandgap in GaN that increased

with pressure. The increasing phonon bandgap frequently pushed some of the high frequency optical modes out of range of previously available down-conversion processes, ultimately causing GaN to become more quasiharmonic with pressure. More similar atomic masses in GaAs, however, prevent GaAs from exhibiting a true phonon bandgap; in this case, pressure was not able to drive the acoustic and optical branches away from each other, and instead created more opportunities for conversion.

Our understanding of the elastic behavior of each material derived from both calculations of the elastic constants and from additional information we could extract from the phonons. We used elastic constants to study elastic anisotropy and to predict the onset of elastic instability using the Born stability criteria. In GaN, elastic anisotropy increased with pressure until reaching elastic instabilities at 65 GPa (wurtzite) and 40 GPa (zinc blende). In GaAs, elastic anisotropy again increased with pressure through the onset of lattice instability, but the Born stability criteria failed to accurately predict this instability. Instead, pressure caused instabilities of shorter-wavelength transverse acoustic modes in both phases of GaAs that preceded the onset of instability predicted by the Born stability criteria, which depend on elastic constants and thereby only long wavelength phonons. In particular, pressure drove the frequencies of shorter-wavelength transverse acoustic phonon instabilities down until they reached 0 THz, inducing instability at 18 GPa (wurtzite) and 20 GPa (zinc blende). Interestingly, temperature caused a significant stabilization of these phonon modes, however, slowing their softening with pressure.

PUBLISHED CONTENT AND CONTRIBUTIONS

1. Herriman, J. E. & Fultz, B. Phonon thermodynamics and elastic behavior of GaAs at high temperatures and pressures. *Physical Review B* (submitted 2020).
   J.E.H. participated in the data generation, analysis, conceptualization and writing of the manuscript.

2. Herriman, J. E., Hellman, O. & Fultz, B. Phonon thermodynamics and elastic behavior of GaN at high temperatures and pressures. *Physical Review B* **98,** 214105. https://link.aps.org/doi/10.1103/PhysRevB.98.214105 (21 Dec. 2018).
   J.E.H. participated in the data generation, analysis, conceptualization and writing of the manuscript.

TABLE OF CONTENTS

LIST OF ILLUSTRATIONS

LIST OF TABLES

Chapter 1

INTRODUCTION

Friends, family, and polite strangers frequently ask me what materials science is. The confusion arises from a couple sources. For one, most people did not have a materials science course in either high school or college, though they may have taken biology, chemistry, and/or physics. So, the term "materials science" remains unfamiliar, though people may actually be familiar with areas of materials science — like metallurgy or the creation of new plastics. Beyond that, materials science is sometimes tricky to define because it is extremely broad and overlaps with multiple areas of the physical sciences and engineering. Materials scientists study the properties and behaviors — whether biological, chemical, mechanical, thermodynamic, etc. — of materials. As a result, some materials scientists will have much more in common with mechanical engineers than the material scientists working in materials chemistry or materials physics. Regardless of their particular focus, materials scientists work to improve our understanding of material properties, ultimately enabling us to predict and tune those properties. Because materials are the bedrock on which advanced technologies are built, material advances enable broad technological advances.

The work discussed in this dissertation lies within computational materials physics. Materials physics broadly refers to the study of physical phenomena within materials, e.g. the mechanisms governing heat transfer, radiation damage, and electronic conduction. Better understanding these phenomena can help us to achieve desirable responses from materials. That this work is "computational" indicates the type of tools I have used to obtain my data. Rather than running physical experiments in a laboratory, I have generated data by running simulations from a laptop, frequently in communication with a supercomputer at either Lawrence Berkeley National Lab or at Lawrence Livermore National Lab. Computational tools have the benefits of facilitating the relatively quick traversal of large parameter spaces and the relatively easy traversal of experimentally difficult, or even intractable, regions of parameter spaces. For example, decreasing the lattice parameter of a simulated material may be done quickly and in arbitrarily small or large steps, whereas serial experimental compression requires expensive equipment (such as diamond anvil cells), more time (even given experienced researchers), and arguably greater patience. Addition-

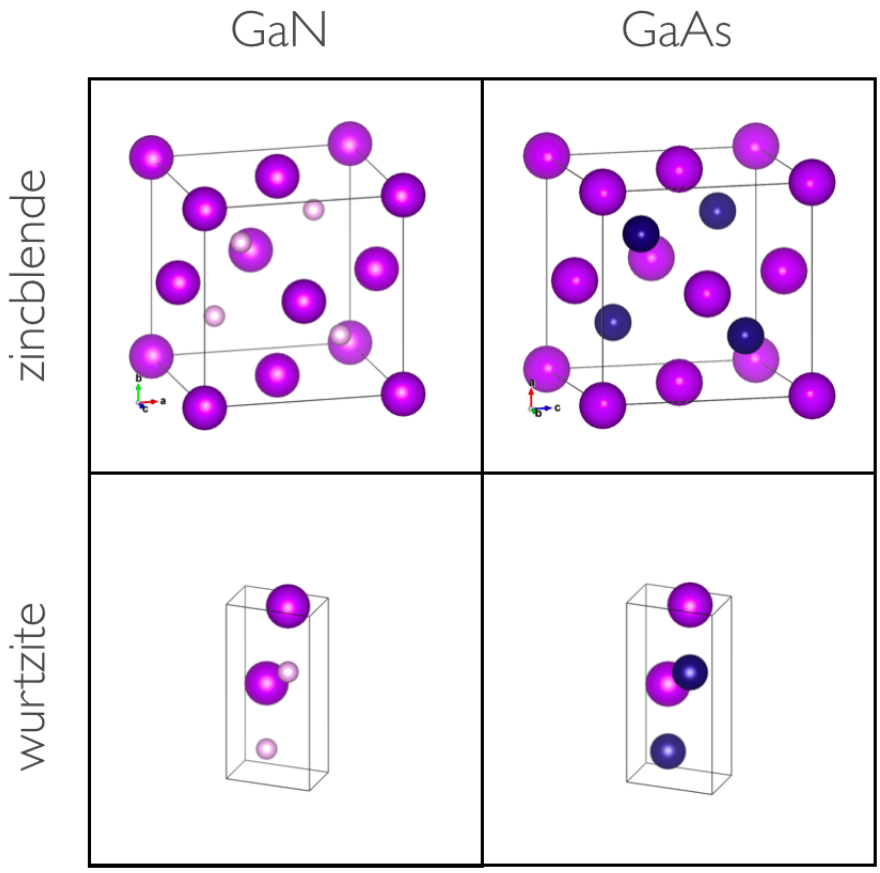

Figure 1.1: The four materials shown — spanning two chemical compositions and two structures — are discussed in the following work.

ally, extreme conditions such as jointly and significantly elevated temperature and pressure can be more accessible computationally than experimentally.

No area of science and engineering would meaningfully advance without models and approximations. Models wrap concrete observations about the natural world into abstractions that describe the behavior or properties we have observed. These models allow us to make estimations and predictions about the natural world, relieving us of the need to measure every aspect of every system that interests us. Yet, as George Box (co-author of the Box-Muller transform discussed later in this thesis) would frequently remind us, "All models are wrong (but some are useful)." The danger of models is in applying them beyond the limits of their utility — of wrongly distilling the trends they summarize to truths.

My research is primarily concerned with the failures of a model known as the "quasiharmonic approximation" (QHA) that is used to account for the impact of

temperature and pressure on thermodynamic properties of materials. We refer to failures of this model as "explicitly anharmonic effects". Explicitly anharmonic effects often increase with temperature and even at modest temperatures can significantly impact the thermal expansion or thermal conductivity of a material, for example. We are interested in better understanding the limitations of the QHA and the relationships between its failures and the underlying characteristics of the materials we use it to model. Composition and crystal structure are the underlying characteristics that define materials, and so we have attempted to better understand how failures of the QHA relate to material composition and structure. Two chemical compositions — Gallium Nitride (GaN) and Gallium Arsenide (GaAs) — and two structures — wurtzite and zinc blende — were chosen for investigation so that we could compare the temperature and pressure driven evolution of anharmonic effects while fixing either composition or structure. These materials in particular — shown in Figure 1.1 — were chosen because both GaAs and GaN are polytypic, such that the structures chosen represent an equilibrium and a metastable structure for each chemical composition under ambient conditions.

In what follows, Chapter 2 presents background, including a section on the thermodynamic properties most relevant to this thesis — phonon spectra and elastic constants — and another on temperature models and approximations. Chapter 3 presents research and results on GaN, and Chapter 4 presents research and results on GaAs. Finally, Chapter 5 provides a summary of this work and possibilities for future directions.

Chapter 2

BACKGROUND

2.1 Phonons

2.1.1 What is a phonon?

We can think of crystalline materials – like most metals, semiconductors, and minerals – as arrangements of atoms – which we might envision as billiard balls – on an infinitely repeating lattice. In classical physics, we assume that at 0 K these atoms sit at their equilibrium positions within the lattice without moving; then, with elevated temperature, the atoms begin to vibrate, gaining the ability to move progressively farther from their equilibrium positions as temperature and energy of the system increase. In quantum physics we learn about “zero point motion" – that atoms are actually already vibrating at 0 K. And so it turns out that atoms are always vibrating, even in a hypothetical temperatureless state.

It turns out these vibrations are discretized. They can actually be resolved into individual packets of energy with frequencies that are characteristic of the particular material considered. Each discrete vibration is a phonon. Phonons travel through a material as waves, but it is sometimes useful to imagine them as particles.

Phonons can be either longitudinal or transverse. Longitudinal phonons exhibit atomic motion parallel to their wavevectors (the directions they travel) and transverse phonons exhibit atomic motion perpendicular to their wavevectors. Therefore, in 3D, there are two transverse phonon modes for every longitudinal phonon mode.

2.1.2 How to read phonon spectra

The two types of spectra shown throughout this dissertation are phonon densities of states (DOS) and phonon dispersion relations. Phonon DOS, such as in Figure 2.1 provide information about all the possible phonon states in a material as a function of frequency. We normalize the DOS to have an area of 1, so the height of the curve at any given frequency provides information about the relative, rather than absolute, number of states available. Note that higher frequency states will become more frequently occupied at elevated temperatures, and therefore that the existence of a state in the DOS does not indicate the occupation of that state.

Phonon dispersion relations, such as in Figure 2.2, provide information about the fre-

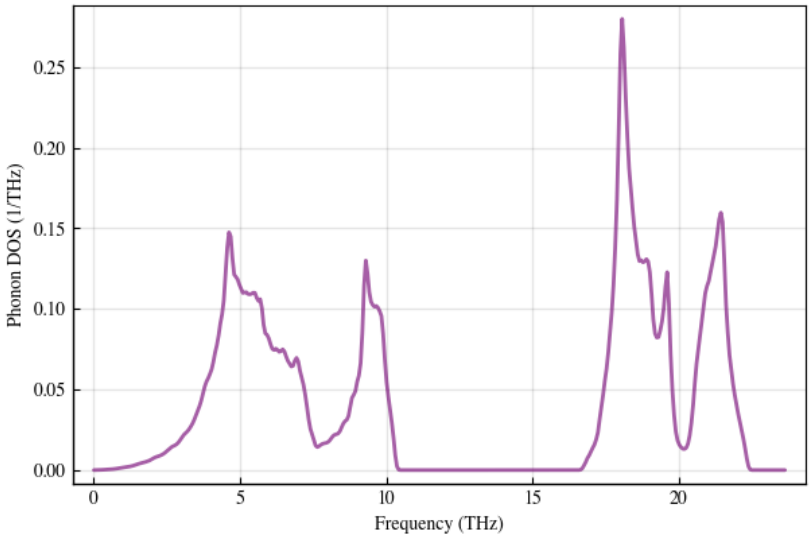

Figure 2.1: An example of phonon densities of states for wurtzite GaN.

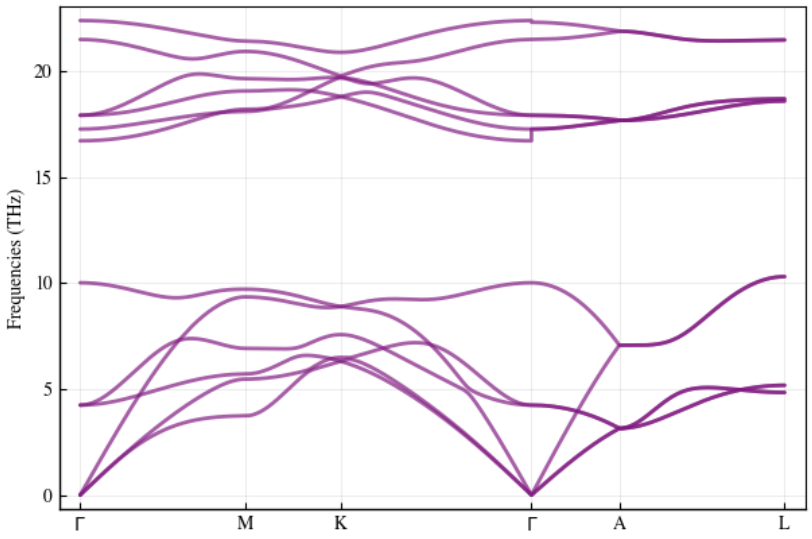

Figure 2.2: An example of phonon dispersion relations for wurtzite GaN.

structure	HSP	coordinates
wurtzite	Γ	$(0,0,0)$
	A	$(0,0,\frac{1}{2})$
	K	$(\frac{2}{3},\frac{-1}{3},0)$
	L	$(\frac{1}{2},0,\frac{1}{2})$
	M	$(\frac{1}{2},0,0)$
zinc blende	Γ	$(0,0,0)$
	K	$(\frac{3}{8},\frac{3}{8},\frac{3}{4})$
	L	$(\frac{1}{2},\frac{1}{2},\frac{1}{2})$
	X	$(0,\frac{1}{2},\frac{1}{2})$

Table 2.1: Momentum space coordinates are provided for each of the high symmetry points (HSP) used to plot phonon dispersion relations in this work.

quencies of phonon states traveling with particular crystal momenta. High symmetry points in momentum space are denoted by characters on the horizontal axis, with the particular coordinates of these high symmetry points in the wurtzite and zinc blende phases detailed in Table 2.1. Phonon states are resolved into $3N$ branches for each point in momentum space, given a material with N atoms in the basis. (Note that Figure 2.2 has 12 branches, indicating a 4 atom basis.) These branches break into 3 acoustic and $3N-3$ optical branches. Acoustic branches tend to be lower energy than optical branches and their frequencies approach 0 THz in the long wavelength limit. The dispersion of optical branches are qualitatively quite different, taking on nonzero values even at the Γ point and often appearing more constant given varying crystal momentum.

2.2 Models of thermodynamic properties

2.2.1 Harmonic approximation

Physics students are first introduced to the harmonic approximation (HA) in the context of a simple harmonic oscillator in which a ball is typically tethered to an infinitely massive wall via a spring. That spring has an equilibrium, or relaxed, length, and the ball has no reason to move as long as the spring remains relaxed. In this state, the ball and spring have zero potential and zero kinetic energy. Perturbing the spring — either compressing it to a shorter length or stretching it to an elongated

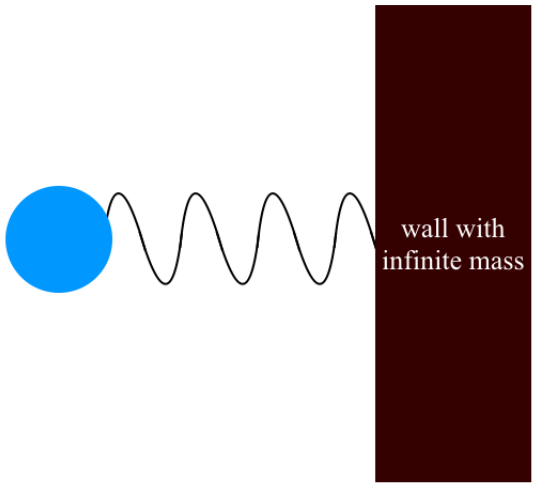

Figure 2.3: A harmonic oscillator is usually first introduced as a ball connected to an infinitely massive wall by a spring that governs its movement according to Hooke's law.

one — injects potential energy into the system. When released, the spring exerts a restoring force that pulls the length of the spring back to its original length; in the process, the potential energy is converted to kinetic energy as the ball begins to move. By the time the ball and spring return to their relaxed positions, the potential energy has returned to zero, but now the kinetic energy of the system is elevated. The ball keeps moving until it runs out of kinetic energy again, having converted that kinetic energy into the potential energy of either a compressed or stretched spring. A harmonic spring repeats this cycle forever, without any energy dissipation, as the ball moves back and forth, passing its equilibrium position. The force on the ball, $\vec{F}_{HA}$, is governed by Hooke's law

$$\vec{F}_{HA} = -k\vec{x} \tag{2.1}$$

where $\vec{x}$ is the displacement of the ball from its equilibrium position and k is the spring constant describing the stiffness of the spring. The potential energy of the spring is

$$U_{HA} = \frac{1}{2}kx^2 \tag{2.2}$$

In a lattice dynamics formalism, we model solid state materials as systems of balls and springs that respectively represent atoms and the chemical bonds that hold them

together. These spring-like interatomic bonds determine how the atoms vibrate about their equilibrium positions. In the HA, the springs connecting neighboring atoms generate restoring forces that are linear with displacement. All vibrations in a material are the result of atoms moving according to Hooke's law, without any damping terms. The vibrations will occur forever and are assumed to be linear combinations of non-interacting resonant phonon modes. Zero thermal resistance and infinite thermal conductivity result from phonons with infinite lifetimes.

A HA also assumes that phonon spectra (like phonon DOS and phonon dispersion relations) do not change with temperature. Therefore it is acceptable to calculate the phonon properties of a material at 0 K and assume those properties are relevant at all other temperatures. Note that, even in a harmonic model, the phonon free energy will change as a function of temperature. The phonon free energy, F_{vib}, is equivalent to $-TS_{vib}$ where T is the temperature and S_{vib} is the phonon entropy. Therefore the magnitude of the free energy should increase with increasing temperature, even if the phonon entropy were fixed. Additionally, the phonon entropy itself changes with temperature, even given a fixed phonon DOS, because the phonon entropy is a function of the Planck distribution

$$n(\epsilon_i, T) = \frac{1}{e^{\frac{\epsilon_i}{k_B T}} - 1} \tag{2.3}$$

Here $n(\epsilon_i, T)$ is the phonon occupancy of a phonon mode of energy ϵ_i at temperature T. A harmonic vibrational entropy[1] can be written as

$$S_{vib}(T) = 3k_B \int_0^\infty g(\epsilon)[(n(\epsilon)+1)\ln(n(\epsilon)+1) - n(\epsilon)\ln(n(\epsilon))]d\epsilon \tag{2.4}$$

The phonon free energy is therefore the sum total of the energies of all the phonons populated in a material. F_{vib} accounts for both the available phonon modes in a material (as given by a phonon DOS) and the likelihood that there is adequate energy in the system to populate any of those modes. So, even though a HA assumes that the phonon DOS is fixed with temperature, it acknowledges that increasing temperature allows higher energy phonon modes in a system to be populated more frequently, increasing the magnitude of the phonon entropy.

Usually the HA works better at lower temperatures than at higher temperatures. At lower temperatures, atomic displacements are smaller and Hooke's law is more accurate for small displacements. Another way of looking at this is that fewer

phonons are populated at low temperatures, and so the likelihood that they interact with other phonons is lower. At higher temperatures, however, as more phonons populate the material, the likelihood that they encounter other phonons increases. Scattering events that result in dampening of higher energy phonon modes become more common. When this occurs, shortened phonon lifetimes result in, equivalently, broadened phonon linewidths, thermal resistance, and finite thermal conductivity.

2.2.2 Quasiharmonic approximations

The equilibrium volume of a material is the volume that minimizes its free energy. The Helmholtz free energy of a system, F, is

$$F = U - TS \tag{2.5}$$

where U is the internal energy, T is the temperature, and S is the entropy. We will approximate the Helmholtz free energy of a material as the sum of U_0, the internal, or ground state energy, of its atoms sitting statically on a lattice, and the phonon free energy

$$F = U_0 - TS_{vib} = U_0 + F_{vib} \tag{2.6}$$

(Often F is reported per atom, and an average is given for materials with different atom types.)

Because the phonon free energy scales with temperature — even given a fixed, harmonic (temperature-independent) phonon DOS — minimizing the free energy function in Equation 2.6 to determine the equilibrium volume of a material should lead to temperature-dependent material volumes. We should thereby expect the assumption of fixed, temperature-independent volumes in a HA to fail, even if we did not know about thermal expansion from experimentation. Quasiharmonic approximations (QHAs) admit this failure of the HA, acknowledging temperature-induced volume changes while assuming harmonic, non-interacting phonons. Changes in volume change the phonon spectra, but in a QHA, these temperature-induced volume changes are the only reason the phonon spectra are expected to change. In other words, all effects of temperature on the phonon DOS and phonon dispersion relations are assumed to be the result of thermal expansion (rarely, negative thermal expansion).

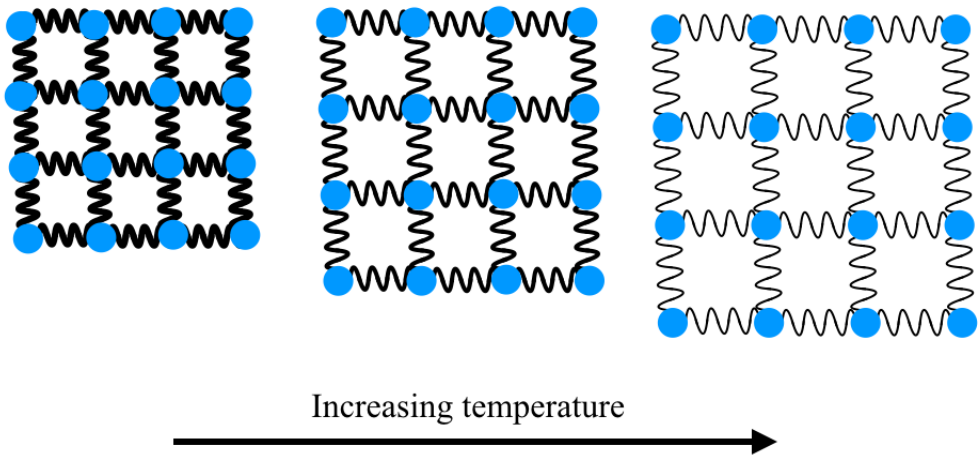

Figure 2.4: In a QHA we can imagine weakening springs as accompanying thermal expansion. Here we depict blue atoms sitting on a square lattice in which springs connect nearest neighbors. Darker, thicker springs are "stiffer" and store more potential energy for fixed displacement than their lighter counterparts.

Intuition from our ball and spring model tells us that a crystal lattice would expand if the springs connecting balls at lattice sites "softened" slightly, becoming more loose or less "springy". The magnitude of the spring constants for an expanding material should decrease, decreasing the potential energy the springs store (for fixed atomic displacements). Extending this intuition to the phonon DOS, we expect that phonon frequencies will typically decrease or "soften" with increasing volume. Conversely, a material would contract if stiffening springs drew neighboring balls closer together. In this case, the magnitude of the spring constants (often called "force constants" in the context of lattice dynamics) should increase, and the phonon frequencies will typically increase or "stiffen" with decreasing volume. Therefore, the "typical" situation is that rising temperature leads to thermal expansion and reduced phonon frequencies, whereas reducing temperature leads to thermal contraction and increased phonon frequencies; similarly, increasing pressure typically increases phonon frequencies.

There are at least a few approaches we could take to accounting for volume changes in quasiharmonic phonon calculations. First, as we did in Lisa Mauger's work on cementite[2], a computationally-determined 0 K equilibrium volume could be scaled to match experimentally-fobserved thermal expansion. Second, thermal expansion could be determined with purely computational inputs, using 0 K harmonic phonons. In this case, harmonic phonon calculations should be performed for many volumes,

allowing for (quasi)harmonic phonon energies to be determined as a function of both volume and temperature. For a given temperature, the volume yielding the lowest free energy should be treated as the equilibrium volume. Third, thermal expansion could be determined with purely computational inputs, using temperature-dependent phonons. *How* to generate temperature-dependent phonons is the topic of the next section. For now, take for granted that, given temperature-dependent phonon calculations, one can minimize the free energy as a function of temperature and volume to determine the equilibrium volume at a given temperature and then calculate harmonic phonons (using the 0 K potential) in a cell that was expanded using temperature-dependent phonons. In the work on GaAs and GaN that follows, this third approach was used when we wanted to make comparisons between fully temperature-dependent and quasiharmonic phonons. In some sense, this approach gives the QHA more credit than it is due. Most researchers using a purely QHA would not likely have expended resources to calculate explicitly anharmonic effects on thermal expansion. As a result, they would probably underestimate the amount of thermal expansion expected by a given temperature and make a worse approximation.

2.2.3 Explicit anharmonicity and TDEP

In both HA and QHAs, the potential energy contains only quadratic terms, reflecting forces that are linear with displacements per Hooke's law. We could write this potential energy between a pair of atoms as

$$U(x) = cx^2 \tag{2.7}$$

where x denotes the displacement between those atoms from their relaxed separation and c is some positive constant[3]. As temperature increases, higher order terms will be needed to describe the potential felt by atoms in a lattice. If we consider anharmonic effects between our pair of atoms, their potential energy could be written as

$$U(x) = cx^2 - gx^3 - fx^4 \tag{2.8}$$

[3]

with higher order terms $-gx^3$ and $-fx^4$ representing third and fourth order anharmonic terms. These terms come from failures to Hooke's law that arise with greater displacements from equilibrium. Another way of thinking about the origin

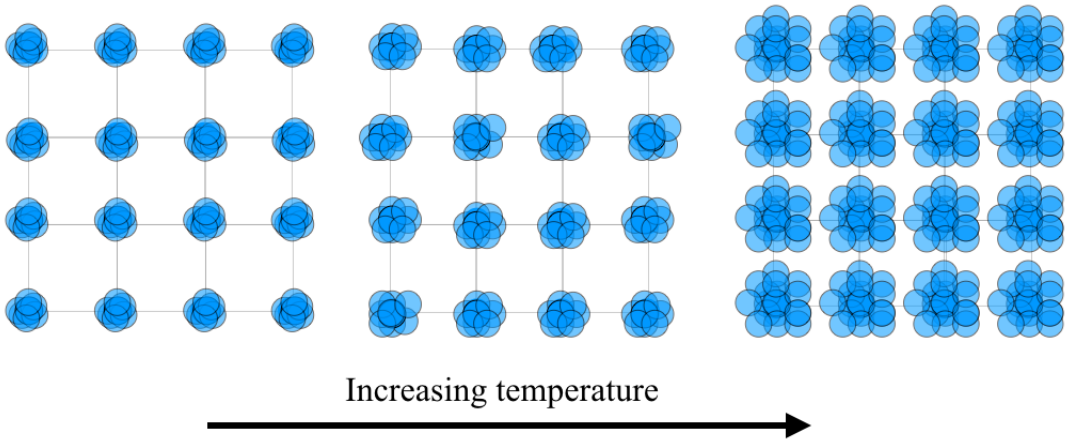

Figure 2.5: Here I depict atoms vibrating about their equilibrium positions on a square lattice, with increasing temperature from left to right. At higher temperatures, atoms become more significantly displaced from equilibrium on average. For simplicity thermal expansion is not shown and the lattice size remains fixed.

of these terms is to consider the changing environment that an atom on a crystal lattice experiences as temperature increases.

Any atom on the lattice shown in Figure 2.5 will surely experience different interactions with its neighboring atoms in each of the different subpanels. The interactions an atom will experience change not merely because that atom varies from its equilibrium position more, but also because each of its neighbors move farther from *their* equilibrium positions, causing them to occupy a greater time-averaged volume. These effects are purely anharmonic, unlike the quasiharmonic lattice effects depicted in Figure 2.4.

So how can we move beyond a QHA and account for a more complex, temperature-dependent and anharmonic potential? In nature these anharmonic potentials simply exist, and fortunately, sufficiently sophisticated simulation methods allow us to recreate them — for example, with ab initio molecular dynamics. With a good lattice dynamics formalism — such as the one used in the Temperature Dependent Effective Potential (TDEP) method — we can capture and describe the potential recreated through simulation.

The high level overview of TDEP is that it imposes a ball and spring model on a material, given information about how forces evolve in response to changing atomic displacements. TDEP calculates second, third, and possibly higher order force constants to describe atomic interactions and then these force constants are used to

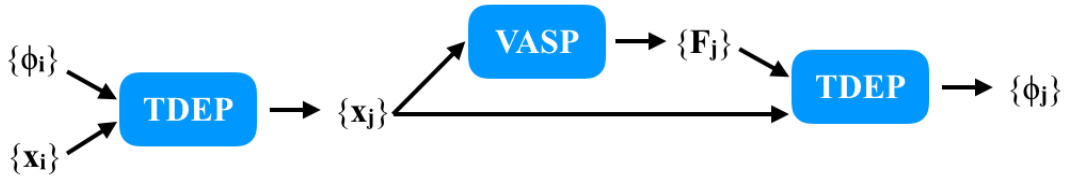

Figure 2.6: This image depicts my workflow using VASP and TDEP, as described in the text.

determine other thermodynamic properties. If molecular dynamics is used to generate force-displacement data, TDEP can be used simply for post-processing. In this case, the molecular dynamics simulation software (such as that offered by VASP[4, 5], Abinit[6], or LAMMPS[7]) will not only output interatomic forces resulting from particular atomic configurations, but will also generate atomic configurations representative of a particular temperature. We refer to this as "sampling phase space". MD software samples the phase space of a material by moving the positions of atoms forward in time according to Newton's laws and the existing forces in the system at the current time step. Many steps must be performed in order to gather adequate statistics and gain adequate information about the material's phase space. MD is therefore computationally intensive. Alternatively, temperature-representative atomic configurations can be generated via TDEP, using a method that we refer to as "sTDEP". I used sTDEP to generate my atomic configurations prior to feeding those configurations to VASP to determine the resulting interatomic forces. In my case, TDEP serves as both pre and post processing software for VASP calculations, depicted in Figure 2.6.

In what follows, I'll describe a few aspects of how TDEP works, including how it generates atomic configurations per sTDEP, how it solves for force constants, and how it determines phonon linewidths using those force constants.

"Stochastic Sampling" with the Temperature Dependent Effective Potential (TDEP) method

Force constants are one of TDEP's outputs, but for sTDEP they are also an input. Figuring out how to get started with sTDEP is therefore not always straightforward. You end up needing to seed sTDEP with preliminary force constants that serve as a "best guess" of what you think the force constants should be. For example, I seeded my GaAs calculations with results from my GaN work, and I seeded my GaN work with the results of a colleague on a different crystal structure. Absent

these resources, I probably would have generated a first batch of force constants using atomic displacements from some method other than TDEP — such as a very short MD run in VASP. If your best guess isn't great but is at least physically reasonable (i.e. you are using force constants with the correct symmetries for the crystal system), that's probably fine. You'll want to take an iterative approach here. In one iteration, seed sTDEP with force constants, use those force constants to generate atomic configurations that you can feed to VASP to generate force data for the calculation of better force constants. Repeat this approach until your input and output force constants are fairly similar.

Each iteration of sTDEP requires the (current best version of the) force constants and relaxed unit/supercells of your system. sTDEP will use the super cell as a template to create different snapshots of your material with temperature-representative thermal displacements; force constants will be given for the unit cell only, which TDEP will map onto the supercell to simulate the elevated temperature. For example, say we have a unit cell of 2 atoms and a supercell of 100 atoms. The supercell of 100 atoms will contain some arrangement of 50 unit cells (though the relative geometries of the cells may make it hard to see exactly how the supercell breaks down into those 50 unit cells). The force constant data describes how each of the two prototype atoms in the unit cell interact with each of many (a user-determined number) neighboring atoms in the nearby unit cells of an infinitely periodic system. Each of the 100 atoms in the supercell will have some relaxed position vector, $\vec{r}_i$, separated from like atoms by integer sums of lattice vectors. sTDEP uses the force constants, relaxed supercell position and lattice vectors, and a user-specified temperature to generate many snapshots of supercells at the user-specified temperature. Each of these snapshots has the same volume and same number of atoms as the input supercell, but the relaxed position vectors, $\{\vec{r}_i\}$, have been thermally displaced by vectors, $\{\vec{u}_i\}$, and replaced by $\{\vec{r}_i' = \vec{r}_i + \vec{u}_i\}$. Vectors $\{\vec{u}_i\}$ reflect the atomic displacements we might expect to see in a material at the user-specified temperature, given the phonon modes that are likely to be populated at that temperature.

Stochastic sampling with TDEP uses Bose-Einstein statistics, information about the phonon modes of the system (their eigenvectors and expected amplitudes), and a bit of randomness to generate many snapshots of temperature-elevated supercells, each with their own set of position vectors, $\{\vec{r}_i'\}$. To understand this, let's start by looking at how sTDEP uses information about s^{th} phonon mode to displace the i^{th} atom of a super cell. (sTDEP is explained more succinctly in Section 4.2.) A Bose-Einstein

distribution tell us the expected number of bosons, such as phonons, with frequency ω_s and degeneracy $g(\omega_s)$ at temperature T via

$$n_s = \frac{g(\omega_s)}{e^{\frac{\hbar\omega_s - \mu}{k_B T}} - 1} \tag{2.9}$$

$$n_s = \frac{1}{e^{\frac{\hbar\omega_s}{k_B T}} - 1} \tag{2.10}$$

which reduces to a Planck distribution when the chemical potential, μ, is zero and then furthermore to the form shown in Equation 2.3 for single degeneracy. Once we know the thermal occupation of the s^{th} mode, we can use that information to figure out the expectation value of the amplitude of the s^{th} phonon mode at the site of the i^{th} atom, i.e. the maximum displacement of atom i from its equilibrium position caused by the s^{th} phonon. The expectation value, or thermal average, of the normal mode amplitude of the s^{th} phonon on the i^{th} atom is

$$\langle A_{is} \rangle = \sqrt{\frac{\hbar(2n_s + 1)}{2m_i\ \omega_s}} \tag{2.11}$$

Here we see that the expected amplitude increases with the occupation of phonon s and decreases for increasingly massive (m_i is mass) atoms, which have more inertia and may be thought of as "more difficult" to move. We could scale the eigenvector of the i^{th} atom and s^{th} mode, $\vec{\epsilon}_{ij}$, by the thermal average of the normal mode amplitude to displace the i^{th} atom — in which case our thermal displacement would be $u_{is} = \langle A_{is} \rangle\, \vec{\epsilon}_{ij}$ — but then we would have no way to generate *different* snapshots of atom i being thermally displaced. So instead, we multiply $\langle A_{is} \rangle\, \vec{\epsilon}_{ij}$ by a normally distributed pseudo-random number, Z, between 0 and 1; this allows us to sample the oscillation of the i^{th} atom with the s^{th} phonon at various points. Z is generated by a Box-Muller transform on two uniformly distributed pseudo-random numbers, ξ_1 and ξ_2

$$Z = \sqrt{-2 \ln \xi_1} \sin 2\pi\xi_2 \tag{2.12}$$

We can now write the displacement of the i^{th} atom in a supercell from its equilibrium position by its s^{th} phonon mode as

$$\vec{u}_{is} = Z \langle A_{is} \rangle \vec{\epsilon}_{is} \tag{2.13}$$

Simply summing over all phonon modes gives a total displacement for this atom. Up to $3N$ phonon modes will populate a supercell of N atoms, giving

$$\vec{u}_i = \sum_{s=1}^{3N} \vec{u}_{is} = \sum_{s=1}^{3N} Z \langle A_{is} \rangle \vec{\epsilon}_{is} \tag{2.14}$$

We create a single "snapshot" using this approach to generate displacements for all N atoms in a supercell, and we create many such snapshots to sample the Born-Oppenheimer surface and approximate its canonical ensemble.

Force Constant Determination

TDEP uses thermal displacements and the resulting interatomic forces to determine the force constants of a material using a model Hamiltonian,

$$\hat{H}_M = U_0 + \sum_{i=1}^{N} \frac{\vec{p}_i}{2m_i} + \frac{1}{2!} \sum_{i=1}^{N} \sum_{j=1}^{N} \sum_{\alpha=1}^{3} \sum_{\beta=1}^{3} \phi_{ij}^{\alpha\beta} u_i^{\alpha} u_j^{\beta} + \frac{1}{3!} \sum_{i=1}^{N} \sum_{j=1}^{N} \sum_{k=1}^{N} \sum_{\alpha=1}^{3} \sum_{\beta=1}^{3} \sum_{\gamma=1}^{3} \phi_{ijk}^{\alpha\beta\gamma} u_i^{\alpha} u_j^{\beta} u_k^{\gamma} \tag{2.15}$$

for a system of N atoms, where i, j, and k denote atomic indices and α, β, and γ denote Cartesian indices. Simplistically the first term U_0 may be thought of as the internal energy of the material, i.e. the energy of its atoms sitting statically at their equilibrium positions. The second term adds the kinetic energy of the nuclei as they vibrate. Both the third and fourth terms account for potential energy resulting from atoms being displaced from their equilibrium positions, modeled as the interactions of neighboring atoms connected by springs with force constants ϕ. The third term uses second order force constants, ϕ_{ij} to model energies arising from pairwise interactions, and the fourth term uses third order force constants, ϕ_{ijk} to model energies arising from three-body interactions. Note that $\hat{H}_M$ explicitly accounts for three-phonon processes but not higher order interactions; TDEP could in principle account explicitly for N-body interactions given adequate statistics and computational resources, but we have only used up to third order force constants in this work. In practice, the first term U_0 also includes effects from the quartic parts of the potential when Equation 2.15 does not include them explicitly.

How does a model Hamiltonian help solve for force constants? By the time we are ready to calculate force constants, we have data connecting a set of forces, $\vec{f}^{BO}$, to the atomic displacements that caused them. In reality, electrostatic interactions generate these forces, and we need information about the electronic wavefunction of a material to quantify interatomic forces. (*Ab initio* software like VASP determines both the wavefunctions and resulting forces.) When we "use a model Hamiltonian", we pretend the source of the known forces in the material is actually a set of 3D springs. We do this essentially by equating our known forces, $\vec{f}^{BO}$, to equations that would determine our model forces, $\vec{f}^{M}$. Per $\hat{H}_M$, the force on the i^{th} atom along the α^{th} Cartesian axis is

$$f_{i\alpha}^{M} = -\sum_{j=1}^{N}\sum_{\beta=1}^{3}\phi_{ij}^{\alpha\beta}u_{j}^{\beta} - \frac{1}{2}\sum_{j=1}^{N}\sum_{k=1}^{N}\sum_{\beta=1}^{3}\sum_{\gamma=1}^{3}\phi_{ijk}^{\alpha\beta\gamma}u_{j}^{\beta}u_{k}^{\gamma} \tag{2.16}$$

Since we know $f_{i\alpha}^{BO}$, we should be able to solve for ϕ_{ij} and ϕ_{ijk} if we simply looked for the closest solution to

$$f_{i\alpha}^{BO} = -\sum_{j=1}^{N}\sum_{\beta=1}^{3}\phi_{ij}^{\alpha\beta}u_{j}^{\beta} - \frac{1}{2}\sum_{j=1}^{N}\sum_{k=1}^{N}\sum_{\beta=1}^{3}\sum_{\gamma=1}^{3}\phi_{ijk}^{\alpha\beta\gamma}u_{j}^{\beta}u_{k}^{\gamma} \tag{2.17}$$

In practice, TDEP exploits the symmetries of a material to reduce the total number of unknowns and reformulate the problem in terms of fewer "irreducible" force constants. Practically the problem is expressed as an overdetermined linear system,

$$\vec{F}^{M} = \mathbf{C}(\vec{u})\vec{\Phi} \tag{2.18}$$

where $\vec{F}^{M}$ is a $3N \times 1$ vector storing the 3-component forces on all N atoms, $\vec{\Phi}$ is a $N_\phi \times 1$ vector storing the N_ϕ irreducible force constants, and $\mathbf{C}(\vec{u})$ is a $3N \times N_\phi$ coefficient matrix that connects the irreducible force constants to the forces via the displacements. Formally we want to minimize $||\vec{F}^{BO} - \vec{F}^{M}||$ to solve for $\vec{\Phi}$, which amounts to

$$\vec{F}^{BO} = \mathbf{C}(\vec{u})\vec{\Phi} \tag{2.19}$$

$$\mathbf{C}(\vec{u})^{-1}\vec{F}^{BO} = \mathbf{C}(\vec{u})^{-1}\mathbf{C}(\vec{u})\vec{\Phi} \tag{2.20}$$

$$\vec{\Phi} = \mathbf{C}(\vec{u})^{-1}\vec{F}^{BO} \tag{2.21}$$

The least squares solution of $\vec{\Phi}$ is then used to recover all second and third order force constants.

Phonon Self-Energy

Once we have the force constants of a material, we can begin calculating material properties such as the phonon self energy, which gives us a window into the anharmonicity of a material.

The self-energy of phonon s is

$$\Sigma_s(\Omega) = \Delta_s(\Omega) + i\Gamma_s(\Omega) \tag{2.22}$$

where the real portion $\Delta_s(\Omega)$ gives the phonon frequency shift, and the imaginary component $\Gamma_s(\Omega)$ allows us to calculate phonon lifetimes. Phonon lifetimes, τ_s, are calculated as $\frac{1}{2\Gamma_s(\Omega)}$ and tell us how likely it is that a phonon will interact with another phonon. As the imaginary component of the phonon self energy increases, so do the number of phonon-phonon interactions; as a result, individual phonon lifetimes decrease, driving down the thermal conductivity, which is an averaged quantity.

Discussions of phonon lifetimes and phonon linewidths are often interchangeable, in part because phonon lifetimes are not directly measurable. Phonon linewidths are a description of the spectral broadening that occurs in measuring phonon spectra through various methods, like Raman scattering, neutron scattering, or inelastic x-ray scattering, due to finite phonon lifetimes. Therefore, phonon linewidths have historically served as an experimental indicator of phonon lifetimes. The relationship between phonon linewidths and phonon lifetimes is clear in a simple case: in the frequency domain, an infinitely persisting phonon could be represented by a δ function — a width-less peak somehow having an area of 1. If we add a dampening term to this phonon such that it no longer lives forever, the frequency domain peak describing it will broaden, assuming a finite width and finite height. Often the broadened peak can be modeled as a Lorentzian, in which case the full width half max (FWHM) of the peak is equal to $2\Gamma_s(\Omega)$, or $\frac{1}{\tau_s}$. So, the phonon lifetime can, in this case, be derived directly from the phonon spectra. On the other hand, spectral broadening does not always create perfect Lorentzians, and then the

connection between phonon lifetimes/phonon self energies and their linewidths is less straightforward. TDEP simply reports the imaginary component of the self energy of each mode, $\Gamma_s(\Omega)$, as its linewidth. This allows for an easy overlay of information about phonon lifetimes with the phonon dispersion relations.

TDEP uses the third order force constants $\phi_{ijk}^{\alpha\beta\gamma}$ to calculate a three phonon matrix with elements $\phi_{ss's''}$ that describe the degree of coupling between phonons s, s', and s''. Elements $\phi_{ss's''}$ are used to calculate $\Gamma_s(\Omega)$.

The three phonon matrix elements are defined as

$$\phi_{ss's''} = \sum_{ijk} \sum_{\alpha\beta\gamma} \frac{\epsilon_s^{i\alpha} \epsilon_{s'}^{j\beta} \epsilon_{s''}^{k\gamma}}{\sqrt{m_i m_j m_k} \sqrt{\omega_s \omega_{s'} \omega_{s''}}} \phi_{ijk}^{\alpha\beta\gamma} e^{i(\vec{q}\vec{r}_i + \vec{q'}\vec{r}_j + \vec{q''}\vec{r}_k)} \tag{2.23}$$

such that $\phi_{ss's''}$ accounts for all possible three body atomic interactions and enforces conservation of momentum.

The imaginary component of the phonon self energy is then defined as

$$\Gamma_s(\Omega) = \frac{\hbar\pi}{16} \sum_{s's''} |\phi_{ss's''}|^2 \{(n_{s'} + n_{s''} + 1)\delta(\Omega - \omega_{s'} - \omega_{s''}) + (n_{s'} - n_{s''})\{\delta(\Omega - \omega_{s'} + \omega_{s''}) - \delta(\Omega + \omega_{s'} - \omega_{s''})\}\} \tag{2.24}$$

The three δ functions in Equation 2.24 pick out scattering events where energy would be conserved; each of the δ functions looks for a different way of combining two of the three phonons considered to generate the third. Once a scattering event that conserves energy has been identified, it is weighted by the thermal occupations of the participating phonons. As such, Equation 2.24 determines $\Gamma(\Omega)$ by accounting for and weighting all possible ways that phonons s' and s'' could couple to phonon s.

2.3 Elastic Properties

2.3.1 Elastic Constants

In Voigt notation, the energy of a crystal under strain, $E(\epsilon)$, may be Taylor expanded as

$$E(\bar{\epsilon}) = E(0) + \sum_{i=1}^{6} \frac{\partial E}{\partial \epsilon_i} |_0 \ \epsilon_i + \frac{1}{2V} \sum_{i,j=1}^{6} \frac{\partial^2 E}{\partial \epsilon_i \partial \epsilon_j} \epsilon_i \epsilon_j \tag{2.25}$$

When the crystal is relaxed with respect to a given strain, we can ignore the stress, $\sigma_k = 0$ such that

$$\frac{\Delta E}{V} = \frac{E(\bar{\epsilon}) - E(0)}{V} = \frac{1}{2V} \sum_{i,j=1}^{6} \frac{\partial^2 E}{\partial \epsilon_i \partial \epsilon_j} \epsilon_i \epsilon_j \tag{2.26}$$

or equivalently as

$$\frac{\Delta E}{V} = \frac{1}{2V} \sum_{i,j=1}^{6} C_{ij} \epsilon_i \epsilon_j \tag{2.27}$$

where the elastic constants are the elements C_{ij} of the elastic tensor $\bar{C}$, such that $C_{ij} = \frac{\partial^2 E}{\partial \epsilon_i \partial \epsilon_j}$

Elastic constants allow us to characterize the elasticity of a material by calculating the material's energetic response to deformation in the same way that a spring constant allows us to calculate a spring's energetic response to deformation. Given that a ball and spring model underpins our formalism for phonons (see Section 2.2.1), this analogy should cue us to a connection between elastic constants and phonon behavior.

It turns out that, in the long wavelength limit, where we can model a material as a continuous solid without worrying about the individual atoms or their periodicity, elastic constants can provide us with much of the information we might have gotten from atomic force constants. For example, it is possible to predict phonon frequencies of the acoustic modes in the long wavelength limit by computing from the elastic constants a dynamical matrix $\bar{M}$ of which the elements are

$$M_{ik} = \sum_{j,l} C_{ijkl} k_j k_l \tag{2.28}$$

The eigenvalues of $\bar{M}$ are the squares of the phonon frequencies, ω, scaled by the density ρ, which we obtain when we apply the dynamical matrix to eigenvector $\vec{u}$:

$$\bar{M}\vec{u} = \rho\omega^2\vec{u} \tag{2.29}$$

The connection between the low energy, long wavelength acoustic phonon modes and elastic constants of a material means that pressure or temperature-driven changes

to the frequencies of the acoustic modes often indicate changing elastic constants and changing elastic anisotropy.

The Born stability criteria, discussed in Chapters 3 and 4, are used to assess the elastic stability of a material by evaluating the values of the material's elastic constants. The relevance of the elastic stability and the use of these stability conditions to give meaningful information about a material assume that a material first becomes unstable when one of the acoustic phonon modes experiences an instability in the long wavelength regime. If a short wavelength phonon were to exhibit an instability before any of the long wavelength phonon modes did so, the instability would neither impact the elastic constants nor the Born stability conditions. Per the Born stability criteria, the material would wrongly appear to be stable.

2.3.2 Bulk and Shear Moduli

We can think of the bulk modulus, K, as the resistance of a material to compression and the shear modulus, G, as the response of a material to forces that are parallel to its surface(s). Elastic constants can be used to place upper and lower bounds on the bulk and shear moduli. For each quantity, Voigt estimates assume constant strain, creating an upper bound, and Reuss estimates assume constant stress, creating a lower bound. We can calculate Voigt and Reuss bounds on the bulk modulus as

$$K_V = \frac{1}{9}\{C_{11} + C_{22} + C_{33} + 2(C_{12} + C_{23} + C_{31})\} \tag{2.30}$$

$$K_R = \frac{1}{S_{11} + S_{22} + S_{33} + 2(S_{12} + S_{23} + S_{31})} \tag{2.31}$$

where $\bar{S}$ is the inverse of the elastic tensor, $\bar{S} = \bar{C}^{-1}$.

Similarly, the Voigt and Reuss bounds on the shear modulus are

$$G_V = \frac{1}{15}\{C_{11} + C_{22} + C_{33} - (C_{12} + C_{23} + C_{31}) + 3(C_{44} + C_{55} + C_{66})\} \tag{2.32}$$

$$G_R = \frac{15}{4(S_{11} + S_{22} + S_{33}) - 4(S_{12} + S_{23} + S_{31}) + 3(S_{44} + S_{55} + S_{66})} \tag{2.33}$$

Chapter 3

GALLIUM NITRIDE

3.1 Introduction

GaN is a wide-band-gap semiconductor used in optoelectronic devices such as light-emitting diodes (LEDs). Under ambient conditions GaN adopts the wurtzite structure, composed of two interpenetrating hexagonal close-packed lattices of Ga and N atoms. Like other III-V materials, GaN is polytypic, and zinc blende GaN is metastable at ambient conditions (see Fig. 3.1). The zinc blende structure consists of interpenetrating face-centered cubic lattices, differing from the wurtzite structure only in the relative positioning of ionic planes; wurtzite has ABABAB... stacking; zinc blende has ABCABC... stacking.[8] Zinc blende GaN is technologically relevant because its metastability allows it to be grown under ambient conditions, [9] and it is more easily doped than wurtzite GaN. [10]

At elevated pressures, III-V materials tend to transform to either the β-Sn structure for more covalent compounds or the rocksalt structure for more ionic compounds. [11] With pressure GaN transforms to the rocksalt structure, changing from tetrahedral to octahedral coordination. Calculations and measurements show that the transformation pressure in GaN is between 30 and 50 GPa. [11, 12] There has been

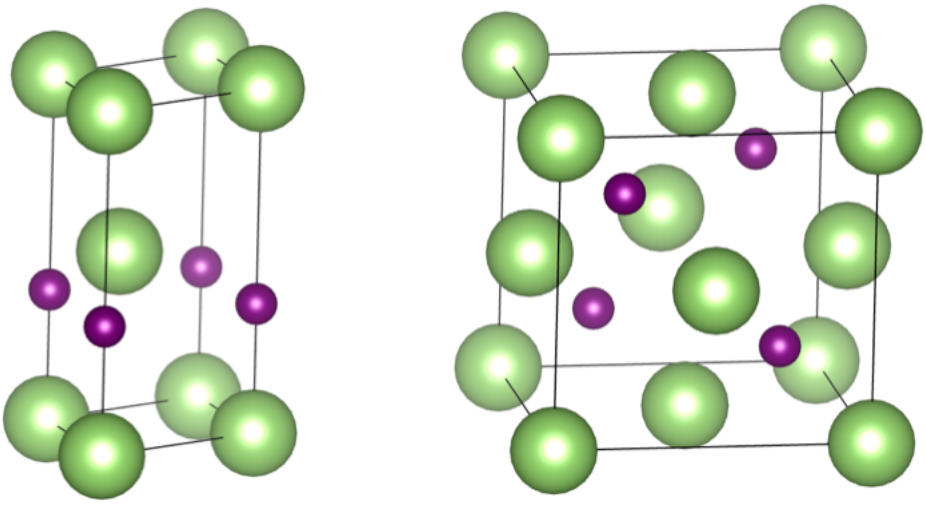

Figure 3.1: Unit cells of the wurtzite (left) and zinc blende (right) structures, with underlying hexagonal and cubic lattices.

much discussion in the literature of the transformation pathway from the wurtzite to rocksalt structure, resulting in a consensus that GaN adopts an intermediate tetragonal structure. [8, 13–15]

Calculations of thermodynamic functions at elevated temperatures are a greater challenge than calculations at elevated pressures. The quasiharmonic approximation (QHA) is a common approach, where the effects of temperature on the phonon frequency ω_i are included through the thermal expansion β, and the mode Grüneisen parameter γ_i (Eq. 3.3). In a QHA the harmonic nature of the phonons is preserved. Since harmonic phonons do not interact, they have infinite lifetimes and the thermal conductivity is infinite. The potential energy surface of a crystal does not vary with temperature in a QHA. The QHA assumes that all effects of temperature originate from changes in volume, with phonons having the same response as from pressure. A QHA therefore ignores explicit anharmonicity from phonon-phonon interactions caused by cubic or quartic perturbations to the potential energy. These explicit anharmonic effects can be important even at low temperatures, however, and typically grow with temperature. Explicit anharmonicity can alter thermal expansion,[16] elastic anisotropy,[2] phase stability,[17] and, of course, transport properties. [17] It is not yet well understood when the QHA is adequate, or if it can be extended to better include anharmonic effects. One useful test is if the accuracy of the QHA varies with pressure.

The present study reports an investigation of phonon frequencies and lifetimes in wurtzite and zinc blende GaN as functions of temperature and pressure, and elastic anisotropy as a function of pressure. The methods and results are described in Sections 3.2 and 3.3. After first discussing effects of pressure at 0 K and of temperature at 0 GPa, it is shown that the effects of T and P on phonons are not additive, and for phonon linewidths there is a marked interdependence of effects from T and P. We also report that the elastic anisotropy increases with pressure in both wurtzite and zinc blende GaN, until each structure reaches an elastic instability at 40 and 65 GPa, respectively. Section 3.4 discusses the explicit anharmonicity and the reliability of a QHA for phonon properties, and how the elastic anisotropy gives upper bounds on the pressures at which wurtzite and zinc blende GaN can persist as thermodynamically metastable phases (when rocksalt GaN is the equilibrium structure).

3.2 Computational

Ab initio calculations were performed on GaN using density functional theory[18] (DFT) as implemented in the Vienna Ab-initio Simulation Package [4, 5] (VASP), using a projector augmented wave method[19], the local density approximation (LDA), and a plane wave cutoff of 600 eV. Total energies and elastic constants were calculated for static lattices using a two-atom zinc blende primitive unit cell and a four-atom wurtzite primitive unit cell with 22×22×22 and 20×20×12 k-point meshes, respectively. For phonon calculations, 4×4×4 and 5×5×4 k-point meshes were used for zinc blende and wurtzite supercells with 216 and 192 atoms, respectively. All k-point meshes were generated with a Monkhorst-Pack scheme[20].

Helmholtz free energies, $F(V,T)$, were calculated as

$$F(V,T) = E_0(V) + F_{ph}(V,T)\,, \tag{3.1}$$

where $E_0(V)$ is the ground state total energy from VASP as a function of volume and $F_{ph}(V,T)$ is the phonon free energy at a particular volume and temperature. Finite temperature phonon properties were calculated using a version of the temperature dependent effective potential method TDEP.[21–23]. This version, s-TDEP, was stochastically-initialized, [24] and accounted for zero point motion. In brief, ensembles of supercells were populated with atoms that were given thermal displacements with phonon populations and polarizations from a quasiharmonic model, and the ensemble average of the energies was used to obtain the best "effective potential" of the form

$$\begin{aligned} H &= U_0 + \sum_i \frac{\mathbf{p}_i^2}{2m} + \frac{1}{2}\sum_{ij\alpha\beta} \Phi_{ij}^{\alpha\beta} u_i^\alpha u_j^\beta \\ &\quad + \frac{1}{3!}\sum_{ijk\alpha\beta\gamma} \Phi_{ijk}^{\alpha\beta\gamma} u_i^\alpha u_j^\beta u_k^\gamma\,. \end{aligned} \tag{3.2}$$

Optimized $\Phi_{ij}^{\alpha\beta}$ and $\Phi_{ijk}^{\alpha\beta\gamma}$ were obtained by minimizing the differences between the forces on the atoms in the ensemble and the forces obtained from the effective potential of Eq. 3.2. (The concept of an effective potential for phonons dates back many years and is reviewed in a delightful paper by Klein and Horton, [25] (also Hooton[26]), who explained in detail how the quartic term in the potential renormalizes the quadratic term in Eq. 3.2.) Force constant determinations account for long range interactions in polar materials that generate LO-TO splitting using Gonze and Lee's correction scheme [27, 28] and VASP Born effective charge tensors.

Phonon properties were calculated for wurtzite and zinc blende GaN at 0 and 1120 K at each of three pressures: 0, 30, and 60 GPa in wurtzite GaN and 0, 15, and 30 GPa in zinc blende GaN (pressures confirmed to be within their ranges of elastic stability). To determine equilibrium material structures at these pressures and temperatures, Helmholtz free energies, $F(V,T)$, were calculated for each material and temperature as a function of volume. Free energies were evaluated only at volumes within the regime of elastic stability in each material; the free energy was evaluated at 14 volumes corresponding to pressures below 64 GPa in wurtzite GaN and at 10 volumes corresponding to pressures below 36 GPa in zinc blende GaN. These energy-volume relationships were fitted with a Birch-Murnaghan equation of state to determine pressure as a function of volume at fixed temperature. Pressures and temperatures of interest were then evaluated by computing phonon properties on supercells of wurtzite and zinc blende GaN held at the corresponding volumes. In wurtzite GaN, aspect ratios were determined quasiharmonically by relaxing a unit cell of wurtzite GaN at volumes of interest with ground state DFT.

3.3 Results

3.3.1 Phonon property calculations

Temperature effects

Figure 3.2 shows phonon densities of states (DOS) for the zinc blende and wurtzite structures at 0 GPa. The phonons at 1120 K were calculated in two ways. The dotted curves labeled "QHA 1120K" were calculated for harmonic force constants with the equilibrium volumes for 1120 K, and a 0 K effective potential. The red curves "1120K" were calculated with force constants from the s-TDEP method, and include effects of both volume expansion and explicit anharmonicity. Comparing the phonon DOS "1120K" with "QHA 1120K" shows the effect of explicit anharmonicity. Evidently, the QHA gives a reasonable temperature dependence of the phonon DOS at 0 GPa. Figure 3.3 gives a more detailed look at how individual phonon dispersions shift with temperature. We see that while phonon frequency shifts occur for higher frequency phonon modes (as evidenced by offsets between blue and red curves), phonon frequencies of acoustic modes near the Γ point do not appear to change between 0 and 1120 K in either material, consistent with the phonon DOS of Fig. 3.2. Figure 3.4 shows again the phonon dispersions at 0 GPa for wurtzite and zinc blende GaN at 0 and 1120 K, now overlaid with phonon linewidth information. There is a substantial broadening of the optical modes at 1120 K, which comes from reduced phonon lifetimes in s-TDEP.

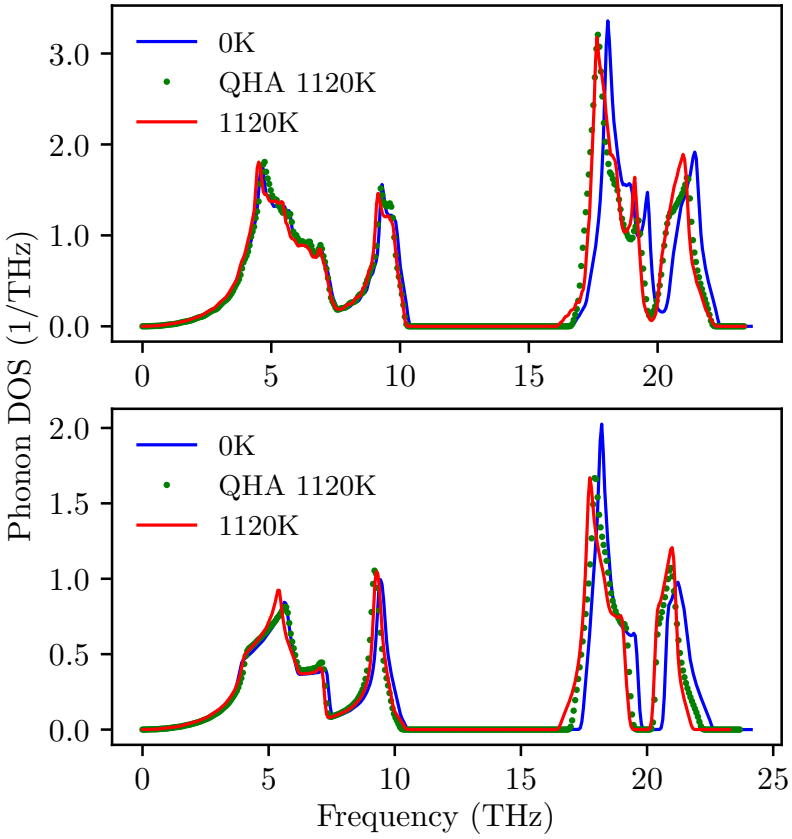

Figure 3.2: Phonon DOS at 0 GPa for wurtzite (top) and zinc blende (bottom) GaN at 0 K (blue), at 1120 K by the QHA (green dots), and at 1120 K by s-TDEP (red).

Pressure effects

Figure 3.5 shows the effects of pressure on the phonon DOS of the zinc blende and wurtzite structures at 0 K. (The Supplemental Information shows that the pressure-driven changes of the phonon DOS are qualitatively similar at 1120 K.) Above approximately 6 THz, phonon modes stiffen with increasing pressure, but below this frequency the phonons soften.

Mode Grüneisen parameters γ_i are defined as

$$\gamma_i = -\frac{V}{\omega_i}\frac{\partial \omega_i}{\partial V} \,. \tag{3.3}$$

The γ_i are commonly positive, so phonon stiffening is expected with increasing pressure. (In contrast, systems that exhibit negative thermal expansion have one

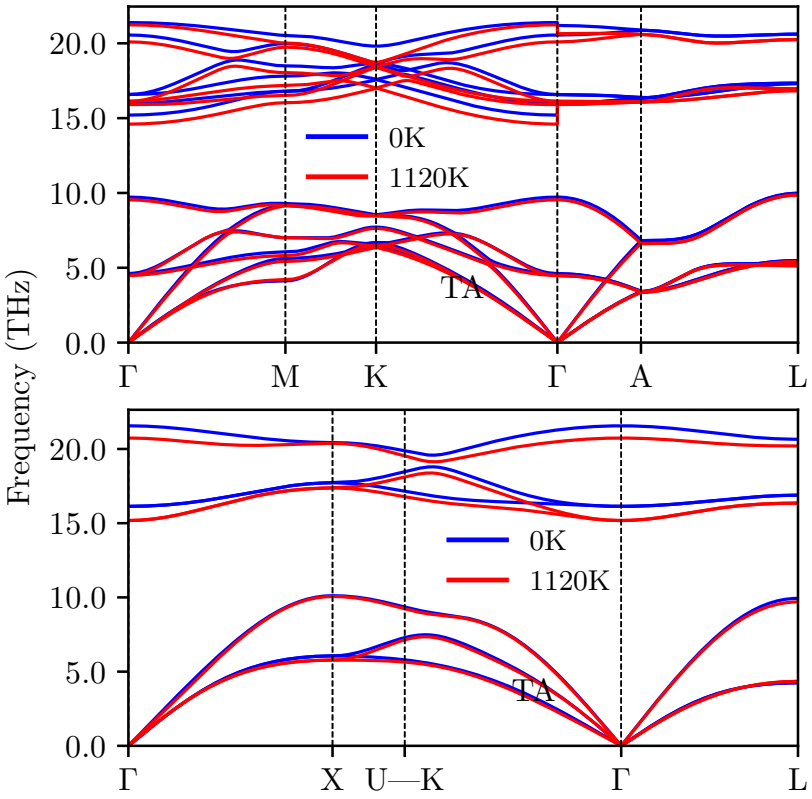

Figure 3.3: Phonon dispersions at 0 GPa for wurtzite (top) and zinc blende (bottom) GaN at 0 K(blue) and 1120 K (red). TA denotes the transverse acoustic branches.

or more mode Grüneisen parameters that are negative.) The mixture of phonon softening and stiffening with increasing pressure seen in Fig. 3.5, is reflected in Fig. 3.6 for mode Grüneisen parameters at 0 K for three pressures. The Grüneisen mode parameters of the transverse acoustic branches are negative for both structures of GaN, consistent with negative Grüneisen parameters for transverse acoustic modes reported in both the zinc blende [29–31] and wurtzite structures. [14, 15] The Grüneisen parameters for most other modes, including optical modes, are not large.

Figure 3.6 shows that the negative mode Grüneisen parameters become more negative with increasing pressure. A consequence is seen between the vertical black dashed lines in Fig. 3.5 — the leftward phonon frequency shift from the green to pink curves is greater than that from the black to green curves. In zinc blende GaN, the increase of 15 GPa from 15 to 30 GPa causes the phonon frequencies to decrease more than does the increase of 15 GPa from 0 to 15 GPa. In wurtzite GaN, the increase of 30 GPa from 30 to 60 GPa shifts the phonon frequencies obviously

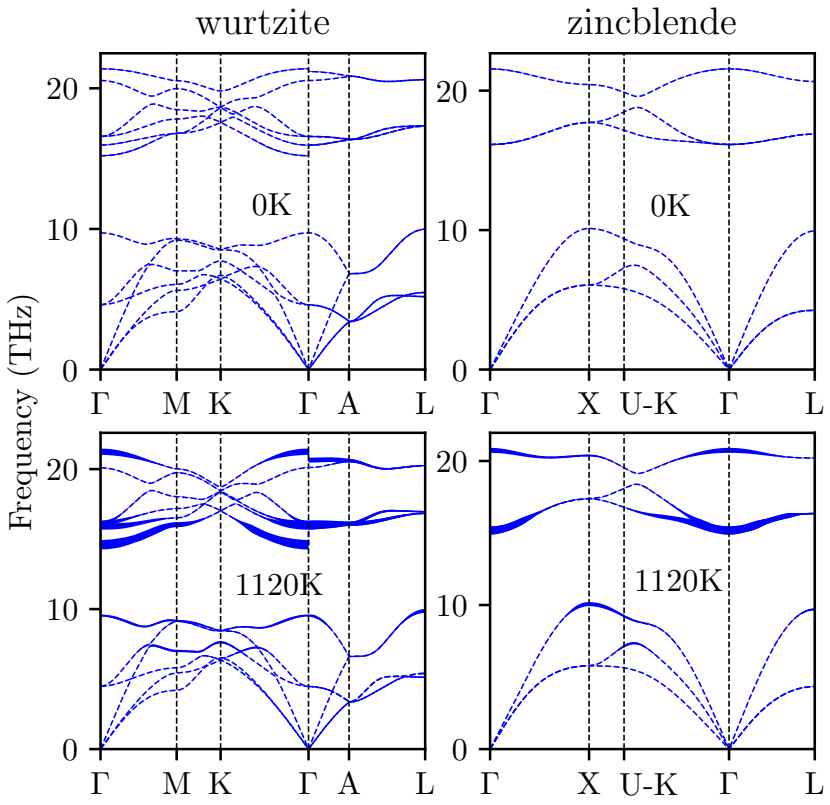

Figure 3.4: Phonon dispersions at 0 GPa for wurtzite (left) and zinc blende (right) GaN at 0 K (top) and 1120 K (bottom) vs. $\vec{k}$ along different directions in the Brillouin zone. Line thicknesses indicate the phonon linewidths, showing broadening of phonon modes at 1120 K.

more than the same pressure increase between 0 and 30 GPa.

Coupled temperature-pressure effects

Figure 3.8 shows an overlay of the 1120 K phonon DOS curves at 0 GPa with rescaled DOS curves from 30 GPa. Specifically, the 30 GPa DOS was rescaled linearly in frequency so its first moment is the same as the DOS at 0 GPa. This rescaling reveals changes in the shape of the DOS with pressure. These changes alter the intrinsic anharmonicity, as discussed later.

Figure 3.9 shows thermal broadenings of phonon linewidths for three pressures. The largest phonon broadenings occur near the Γ point for both structures of GaN, but these thermal broadenings change considerably with pressure.

The effects of pressure on the thermal broadening are markedly different for the

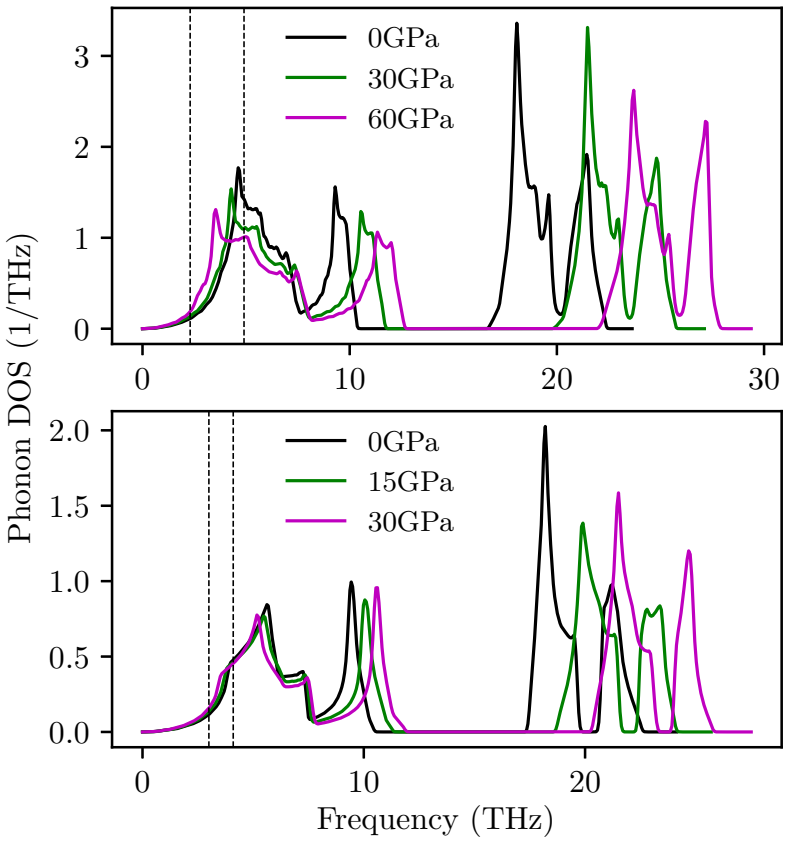

Figure 3.5: Phonon DOS at 0 K for wurtzite GaN at 0, 30, and 60 GPa (top), and for zinc blende GaN at 0, 15, and 30 GPa (bottom). Acoustic modes below 6 THz exhibit softening with increased pressure, whereas higher energy modes stiffen. Dashed vertical black lines delineate a feature in the DOS that softens with increasing pressure.

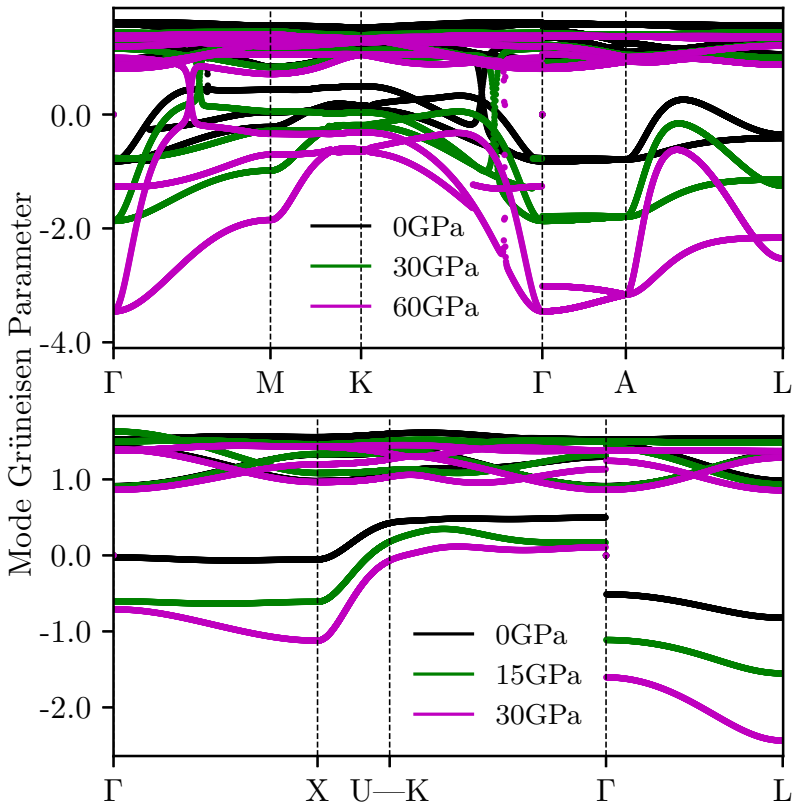

Figure 3.6: Mode Grüneisen parameters at 0 K for all phonon branches at three pressures in wurtzite (top) and zinc blende (bottom). In both panels, pressure increases from the black to green to pink. Pressure causes large changes in the negative Grüneisen parameters, which correspond to transverse acoustic modes.

different phonons — the shapes of the curves at 0 GPa are not simply rescaled with pressure. Furthermore, for individual phonons the effects of pressure are highly nonlinear. For example, the thermal broadenings of phonons near the Γ point of both structures are reduced by the first increase in pressure (from 0 to 30 GPa in wurtzite and from 0 to 15 GPa in zinc blende GaN), but for most phonons the reduction of thermal broadening is much greater as the pressure increases again, from 30 to 60 GPa in wurtzite GaN and from 15 to 30 GPa in zinc blende GaN. Curiously, the thermal broadening in the wurtzite structure from Γ to A to L is largest at 0 GPa, smallest at 30 GPa, and returns to an intermediate values at 60 GPa. The phonon thermal broadening changes qualitatively with pressure, with all phonons undergoing a different nonlinear response.

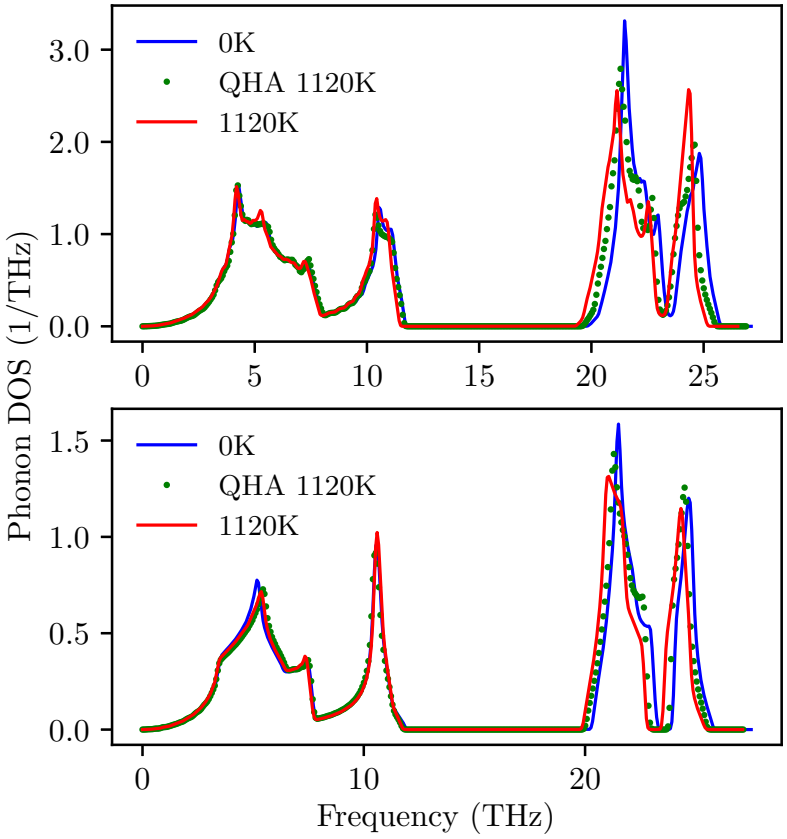

Figure 3.7: Similar to Fig. 3.2, phonon DOS at 30 GPa for wurtzite (top) and zinc blende (bottom) GaN at 0 K (blue), at 1120 K with the quasiharmonic approximation (green dots), and at 1120 K by s-TDEP (red).

3.3.2 Elastic constants and elastic instability

The universal elastic anisotropy index[32], A^U, was used to quantify the elastic anisotropy

$$A^U = 5\frac{G_V}{G_R} + \frac{K_V}{K_R} - 6\,, \tag{3.4}$$

where the subscripts R and V denote Reuss and Voigt averages, which provide lower and upper bounds, respectively, on the shear (G) and bulk (K) moduli. Using formulations summarized by Hill[33], Reuss and Voigt averages of the shear and bulk moduli were calculated using VASP elastic constants obtained from static lattices. (VASP determines the elastic tensor by applying finite distortions to a unit cell to determine stress-strain relationships.) Larger values of A^U indicate increasing elastic anisotropy, whereas $A^U = 0$ for an elastically-isotropic medium.

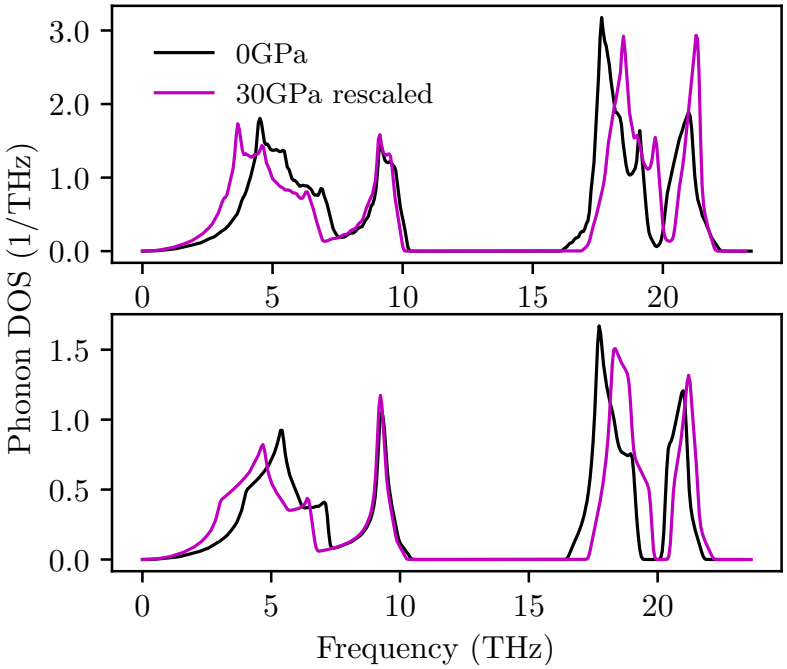

Figure 3.8: Phonon DOS at 1120 K for wurtzite (top) and zinc blende (bottom) GaN for 0 GPa (black) and 30 GPa with the mean frequency scaled to match that of the 0 GPa spectrum (magenta).

Figure 3.10 shows that for both wurtzite and zinc blende GaN, the elastic anisotropy first increases approximately linearly with pressure at low and moderate pressures. At high pressures, however, the elastic anisotropy increases rapidly, indicative of a pressure-induced lattice instability, *i.e.*, elastic collapse; this is shown in the Supplemental Information.

The pressures corresponding to the onset of elastic instabilities, P_{EI}, of zinc blende and wurtzite GaN are identified by criteria similar to the "Born stability criteria", but which account for finite pressures, as done previously. [34–37] For cubic crystals such as zinc blende, these elastic stability criteria are

$$B_{11} - B_{12} > 0, \quad B_{44} > 0, \quad B_{11} + 2B_{12} > 0 \, . \tag{3.5}$$

For hexagonal crystals, such as wurtzite, they are

$$B_{11} > |B_{12}|, \quad B_{44} > 0, \quad B_{33}(B_{11} + B_{12}) > 2B_{13}^2 \, . \tag{3.6}$$

In terms of the elastic constants C_{ij} and pressure P, the elastic stiffnesses, B_{ij}, are

$$B_{ii} = C_{ii} - P \text{ for } i = 1, 2, \ldots 6 \, , \tag{3.7}$$

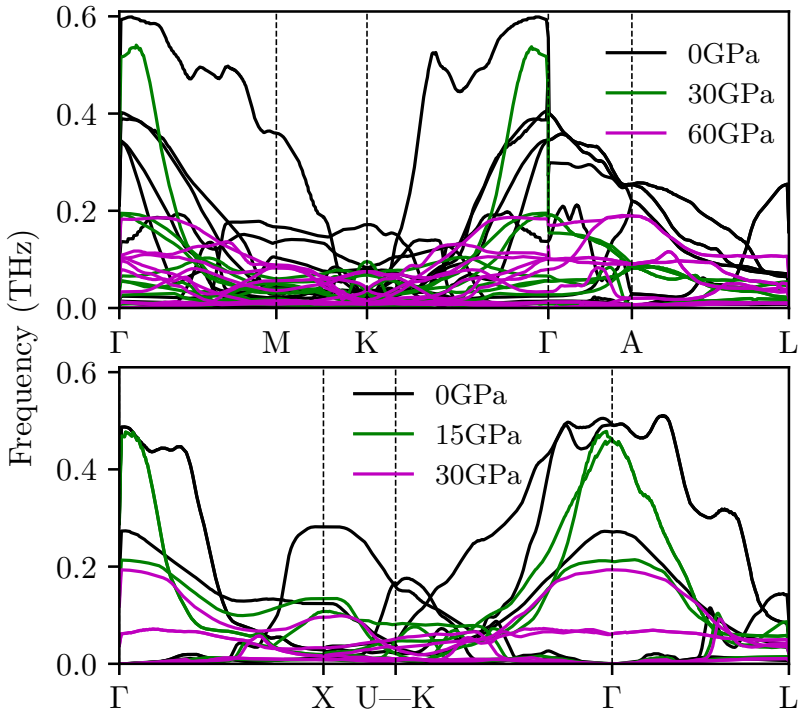

Figure 3.9: Change in phonon linewidths between 0 K and 1120 K at three pressures for wurtzite (top) and zinc blende (bottom) GaN. In each panel, pressure increases from the black to the green to the red curves.

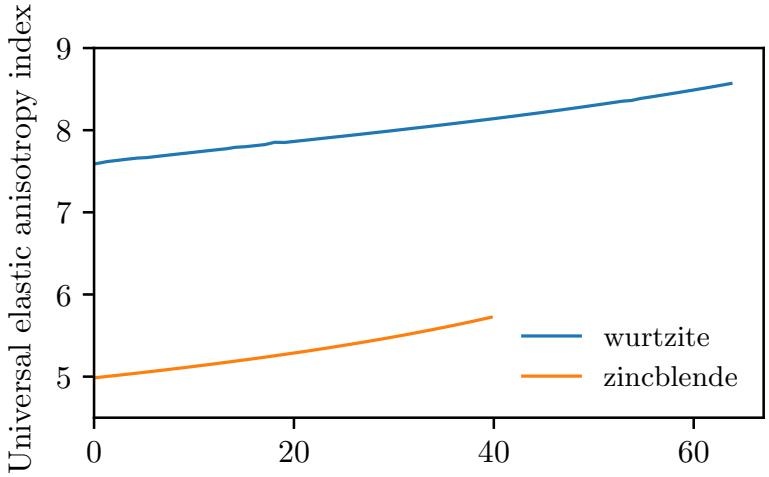

Figure 3.10: The universal elastic anisotropy index A^U of wurtzite and zinc blende GaN vs. pressure in the regime of elastic stability.

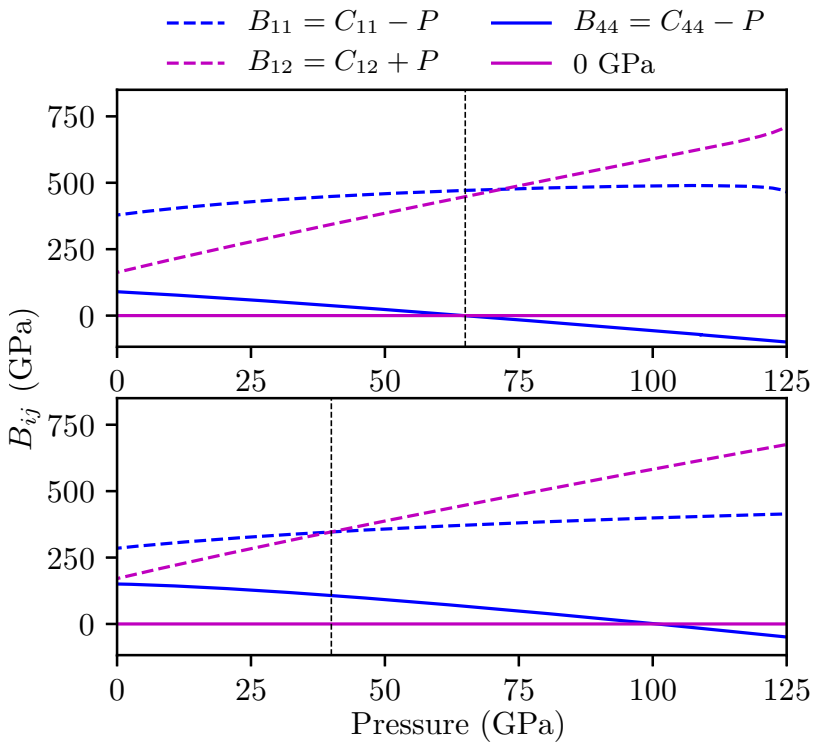

Figure 3.11: Here we see elastic stiffnesses plotted against pressure. In both panels, B_{11} and B_{12} cross over where dashed blue and magenta lines intersect, and B_{44} is no longer greater than 0 GPa where solid blue and magenta lines intersect. Wurtzite GaN (top) becomes elastically unstable when B_{44} crosses the 0 GPa line at approximately 65 GPa; zinc blende GaN (bottom) becomes elastically unstable when B_{11} and B_{12} cross over at 40 GPa. Vertical black lines identify P_{EI}.

$$B_{1j} = C_{1j} + P \text{ for } j = 2,3\ . \tag{3.8}$$

With increasing pressure, the first stability condition to fail is taken as the reason for an elastic instability. These conditions are explained further in the Supplemental Information. Using Eqs. 3.5 and 3.6, P_{EI} for the wurtzite and zinc blende structures are found to be 65 and 40 GPa, respectively. Zinc blende GaN becomes unstable when B_{12} exceeds B_{11}, *i.e.*, when the tetragonal shear modulus, $C_{11} - C_{12}$, becomes less than twice the pressure, $2P$. This is a "tetragonal shear instability."[36] Wurtzite GaN exhibits this same failure mechanism at 72 GPa, but first becomes elastically unstable when B_{44} becomes nonpositive, *i.e.*, when the pressure, P, exceeds C_{44}. The failures of these stability conditions are shown in Fig. 3.11.

These calculated values of P_{EI} fall within the range of approximately linear pressure dependence of the universal elastic anisotropy index (Fig. 3.10).

3.4 Discussion

3.4.1 Pressure-temperature coupling and the quasiharmonic approximation

Mode Grüneisen parameters (Eq. 3.3) are found by evaluating the volume dependence of phonon frequencies, and Grüneisen parameters as in Fig. 3.6 are the basis for the quasiharmonic approximation (QHA). The quasiharmonic model assigns a temperature dependence of the phonon frequency to the thermal expansion β as

$$\omega_{i,QHA}(V, T_0 + \Delta T) = \omega_{i,0}(1 - \beta\gamma_i\Delta T)\,, \tag{3.9}$$

where $\omega_{i,0}$ is the phonon frequency at the initial temperature T_0, and γ_i is the mode Grüneisen parameter of Eq. 3.3. The phonon densities of states in both wurtzite and zinc blende shift to lower frequencies (soften) with increasing temperature between 0 and 1120 K at fixed pressure. Figure 3.2 suggests that the quasiharmonic model may be adequate for understanding the temperature dependence of phonon thermodynamics at 0 GPa, although there are some differences compared to a more proper accounting of anharmonicity. The results of Fig. 3.7 suggest that the QHA for thermal shifts of phonons may be less reliable at higher pressures, however.

The s-TDEP method starts with quasiharmonic phonons for calculating the effective potential at elevated temperature. Using a supercell with atoms displaced by these phonons, it obtains the best force constants for an ensemble of supercells. The s-TDEP method obtains anharmonic phonon frequency shifts (often attributed to the cubic and quartic terms in the phonon self-energy [38, 39]) by renormalizing[25, 26] the interatomic forces of Eq. 3.2 for the T and V of interest.

In general, phonon frequencies depend on the average positions of nuclei and temperature (which moves them about their average positions), so $\omega = \omega(V, T)$. The Grüneisen parameter is proportional to the volume derivative, $\gamma \sim (\frac{\partial\omega}{\partial V})_T$, and the anharmonicity is proportional to the temperature derivative, $A \sim (\frac{\partial\omega}{\partial T})_V$. By taking derivatives of these quantities with respect to the other variable, and equating mixed derivatives as $(\frac{\partial^2\omega}{\partial T\partial V})_{VT} = (\frac{\partial^2\omega}{\partial V\partial T})_{TV}$, it can be shown that the temperature derivative of the Grüneisen parameter $(\frac{\partial\gamma}{\partial T})_V$ equals the volume derivative of the anharmonicity $(\frac{\partial A}{\partial V})_T$. The physical origins of these two effects must be the same.

Figure 3.8 helps explain why the intrinsic anharmonicity changes with pressure. If the shape of the DOS did not change with pressure, the number of channels for three- and four-phonon processes would change only slightly, and in proportion to the mean phonon shift. Figure 3.8 shows that this is not the case because pressure causes a significant change in the shape of the DOS. Negative Grüneisen parameters

cause the transverse acoustic modes to shift lower with respect to the mean, and the optical modes move higher. As these modes move apart with pressure, there are fewer three-phonon processes that can bridge them.

The resulting effects of pressure on explicit anharmonicity are evident in the phonon linewidths (which are, of course, zero in the QHA). Phonon linewidths are dominated by effects of cubic anharmonicity, since quartic anharmonicity gives no imaginary contribution to the phonon self-energy. [38, 39] Pressure-induced changes in three-phonon processes explain the pressure-driven differences in thermal phonon broadening seen in Fig. 3.9. At low or moderate temperatures, the line broadening of the optical modes $\omega(\vec{q})$ around the Γ point are dominated by down-conversion processes that have the kinematical factor

$$D_{\downarrow}(i,\vec{q}) = \frac{1}{N}\sum_{\vec{q}_1,\vec{q}_2,j_1,j_2} \Delta(\vec{q}-\vec{q}_1-\vec{q}_2)\delta(\omega-\omega_1-\omega_2)\,, \tag{3.10}$$

where $\omega(\vec{q}_1)$ and $\omega(\vec{q}_2)$ are acoustic phonons. As pressure is increased, Fig. 3.5 shows that the optical modes shift upwards proportionally faster than the acoustic modes. The ratio of energies of the bottom of the optical modes to the top of the acoustic modes changes from approximately 1.55 at 0 GPa to 1.71 at 60 GPa for wurtzite, and changes from 1.61 at 0 GPa to 1.66 at 30 GPa for zinc blende. If this were to reach 2.0, there would be zero terms in Eq. 3.10, but in three dimensions a change from 1.55 to 1.71 causes a large decrease in the number of possible three-phonon processes around the Γ-point. The effects of cubic anharmonicity on the thermal linewidths should therefore be reduced strongly with pressure. The observed decrease in thermal broadening with increasing pressure is consistent with this, indicating a reduction in cubic anharmonicity from three-phonon processes. As thermal broadening decreases, harmonic phonons become better eigenstates of the system.

At temperatures of order 1000 K and pressures of order 10 GPa it is not appropriate to consider only a quasiharmonicity $\propto P$, and an anharmonicity $\propto T$. These two contributions are not additive. The T-dependences of phonon frequency shifts and linewidths are pressure dependent; in other words, the effects of temperature and pressure on phonon frequencies have a coupling term $\propto TP$. Finally, the nonlinearity of the phonon shifts with pressure seen in Fig. 3.5 shows that a term proportional to P^2 may also be necessary to account for the phonon shifts at tens of GPa.

Both phonon frequency shifts and phonon linewidths are related to thermal conductivity. One implication of the failures of the QHA, and the anharmonicity at

elevated T and P, is that calculations of thermal conductivity must be performed at the at high T and P of interest.

3.4.2 Elastic anisotropy and lattice instabilities

By calculating elastic anisotropy as a function of pressure, we showed that elastic anisotropy in both wurtzite and zinc blende GaN increases with pressure. Both the zinc blende and wurtzite structures of GaN become elastically unstable, and cannot exist at pressures higher than 40 and 65 GPa, respectively. Rocksalt is the thermodynamically favored structure of GaN at elevated pressures, with zinc blende GaN predicted to transform to rocksalt GaN near 40 GPa, and wurtzite GaN observed to transform to rocksalt between 30 and 50 GPa. The predicted mechanism by which zinc blende transforms to rocksalt begins with a tetragonal distortion[8], which is consistent with our result that zinc blende GaN becomes elastically unstable due to tetragonal shear. A consensus in the literature is that wurtzite GaN forms a tetragonal intermediate structure prior to transforming to rocksalt. The work of Saitta, et al. [15], implicate softening of the C_{44} and C_{66} elastic constants in this transformation. This is consistent with our work, where softening of C_{44} and C_{66} with increasing pressure lead to failures of two elastic stability conditions in wurtzite GaN at 65 and 72 GPa, respectively.

Our result that elastic instability occurs at 65 and 40 GPa in wurtzite and zinc blende GaN, respectively, places upper bounds on the existence of these structures. In discussing the transformation pathway of wurtzite to rocksalt in AlN, InN, and GaN, one author ruled out the metastability of the wurtzite structure above the transformation pressure for AlN and InN, but not for GaN.[10] This same work calculated a coexistence pressure of 74 GPa for the SC16 and wurtzite structures of GaN, suggesting the possibility of wurtzite metastability up to at least 74 GPa. Our work shows that by 65 GPa, wurtzite GaN will be mechanically unstable, preventing such a thermodynamic metastability. Similarly, above 40 GPa, zinc blende GaN will no longer be thermodynamically metastable.

The phonon dispersion relations of GaN indicate that these results on elastic anisotropy and elastic stability of wurtzite and zinc blende GaN should not be significantly dependent on temperature.

In the long wavelength limit, the elastic constants may be determined as a function of force constants. Given this relationship between elastic constants and force constants, invariance of low-energy acoustic phonon branches equates to invariance

of the elastic constants. In Fig. 3.3, we see that the low-energy acoustic phonon modes are not sensitive to temperature; in particular, we see in Fig. 3.3 that the red and blue curves in each panel overlap nearly perfectly when the acoustic branches extending from the Γ point are linear. (As shown in the Supplemental Information, the low-energy acoustic modes are insensitive not only to the full effects of temperature but also to the temperature-driven volume changes between 0 and 1120 K.) Similarly we see in Fig. 3.2 that the phonon DOS at 0 and 1120 K overlap nearly perfectly below about 5 THz in both structures of GaN. As the elastic constants of either structure do not change significantly with temperature, temperature will not significantly alter the pressures at which these structures become elastically unstable, or the elastic anisotropy trends at 0 K.

3.5 Conclusions

For a pressure of 0 GPa, a simple quasiharmonic approximation, which attributes both temperature and pressure dependences of phonon self-energies to changes in volume, predicts temperature dependences of phonons in wurtzite and zinc blende GaN that are approximately correct. Effects of the explicit anharmonicity of phonons varies with pressure, and our results suggest a quasiharmonic approximation predicts thermal shifts of phonons less successfully by 30 GPa.

Pressure determines the degree to which temperature alters the lifetimes of optical phonons, owing to a decrease in the number of 3-phonon downscattering channels for optical modes. Accounting for the effects of T and P on the phonons in both zinc blende and wurtzite GaN over a range of T and P of approximately 1000 K and tens of GPa requires, at a minimum, that phonon frequencies have terms that depend on P (quasiharmonicity), T (explicit anharmonicity), PT, and P^2.

The elastic anisotropy was found to increase with pressure in both wurtzite and zinc blende GaN. An elastic instability was found in wurtzite GaN at 65 GPa and in zinc blende GaN at 40 GPa, providing upper bounds for the possible metastability of either phase, after rocksalt GaN becomes thermodynamically favorable. Thermal trends in long-wavelength phonons show that the pressures of elastic instability should be reliable to temperatures of 1120 K.

3.6 Supplemental Information

3.6.1 Elastic stability conditions

Origin of elastic stability conditions

A "stable" crystal structure must be stable both dynamically and elastically. Dynamical stability requires nonnegative phonon frequencies for all phonon modes and wavevectors; elastic stability requires that the elastic energy, E, is always positive.[40]

In the harmonic approximation, $i.e.$, at zero applied stress, the elastic energy of a crystal is quadratic with applied strains, ϵ_i, as follows

$$E = E_0 + \frac{1}{2} V_0 \sum_{i=1}^{6} \sum_{j=1}^{6} C_{ij} \epsilon_i \epsilon_j \ , \tag{3.11}$$

where E_0 is the equilibrium elastic energy, V_0 is the equilibrium volume, and C_{ij} are the elastic constants, $i.e.$, the elements of the elastic tensor in Voigt notation. The rightmost term in Eq. 3.11 accounts for the elastic energy of a crystal due to strain. We can only ensure E is positive if Eq. 3.11 is convex. This requires that the matrix $\mathbf{C}$ is positive definite, or equivalently that all the eigenvalues of $\mathbf{C}$ are positive.[40]

If $\mathbf{C}$ is positive definite, the determinant of $\mathbf{C}$ will be positive (because the determinant of a matrix may be calculated as the product of all eigenvalues of that matrix)

$$\det(\mathbf{C}) = \prod_{i=1}^{n} \lambda_i = \lambda_1 \lambda_2 \cdots \lambda_n \ . \tag{3.12}$$

Requiring $\det(\mathbf{C})$ to be positive allows us to derive necessary conditions for elastic stability shown below.[35]

Cubic stability conditions

$$C_{11} - C_{12} > 0, \ \ C_{44} > 0, \ \ C_{11} + 2C_{12} > 0 \ . \tag{3.13}$$

Hexagonal stability conditions

$$C_{11} > |C_{12}|, \ \ C_{44} > 0, \ \ C_{33}(C_{11} + C_{12}) > 2C_{13}^2 \ . \tag{3.14}$$

Elastic stability conditions at finite stress

Elastic stability conditions can be formed in terms of elements, B_{ij}, of the elastic stiffness tensor, **B**, to account for finite stress, where

$$B_{ij} = (\frac{\partial \sigma_i(\vec{y})}{\partial \epsilon_j})_{\vec{x}} \, , \tag{3.15}$$

where $\vec{x}$ and $\vec{y}$ respectively denote the coordinates of the system before and after deformation, and σ_i and ϵ_j denote elements of the stress and strain tensors.[36] [38]

The coefficients B_{ij} can be written in terms of the elastic constants C_{ij} and the external load τ. Note that we have until now used Voigt notation to reduce the orders of the $3 \times 3 \times 3 \times 3$ tensors $\tilde{\mathbf{B}}$ and $\tilde{\mathbf{C}}$ to 6×6 matrices **B** and **C**. Below we give the more general form for the elastic stiffnesses, $\tilde{B}_{ijkl}$, elements of the elastic stiffness tensor, $\tilde{\mathbf{B}}$ [36]

$$\begin{aligned} \tilde{B}_{ijkl} = \tilde{C}_{ijkl} \quad + \quad & \frac{1}{2}(\delta_{ik}\tau_{jl} + \delta_{jk}\tau_{il} \\ & + \delta_{il}\tau_{jk} + \delta_{jl}\tau_{ik} - 2\delta_{kl}\tau_{ij}) \, . \end{aligned} \tag{3.16}$$

With an isotropically applied stress, *i.e.*, hydrostatic pressure, τ_{ij} is proportional to δ_{ij}[35]

$$\tau_{ij} = -P\delta_{ij} \, . \tag{3.17}$$

Substituting Eq. 3.17 into Eq. 3.16 for $\tilde{B}_{ijkl}$ gives

$$\tilde{B}_{ijkl} = \tilde{C}_{ijkl} + \frac{P}{2}(2\delta_{ij}\delta_{kl} - \delta_{il}\delta_{jk} - \delta_{ik}\delta_{jl}) \, . \tag{3.18}$$

After substituting the values of δ_{ij} where

$$\delta_{ij} = \begin{cases} 1, & \text{if } i = j \ \& \ i \leq 3 \\ 0, & \text{otherwise} \, , \end{cases} \tag{3.19}$$

the tensor $\tilde{\mathbf{B}}$ can again be expressed as a symmetric matrix, **B**. Restricting the determinant of **B** to positive values as done for **C** in Section 3.6.1 gives elastic stability conditions at finite stress in terms of B_{ij}[35] where

$$B_{ii} = C_{ii} - P \text{ for } i = 1, 2, \ldots 6 \, , \tag{3.20}$$

$$B_{1j} = C_{1j} + P \text{ for } j = 2, 3 \, . \tag{3.21}$$

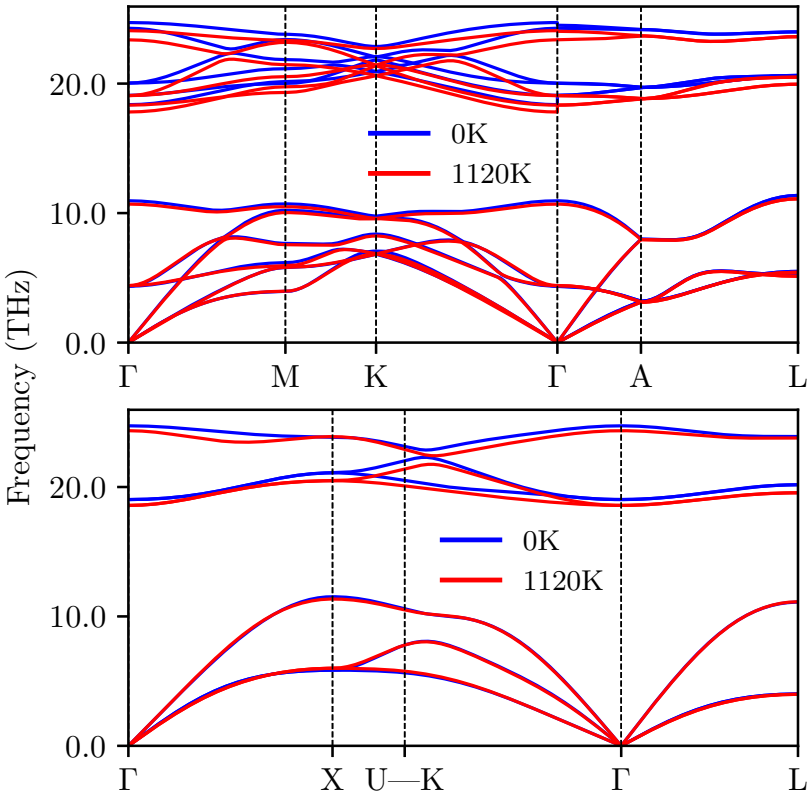

Figure 3.12: Similar to Fig. 3 of the main paper, phonon dispersions at 30 GPa for wurtzite (top) and zinc blende (bottom) GaN at 0 K (blue) and at 1120 K (red).

Cubic finite stress stability conditions

$$B_{11} - B_{12} > 0, \quad B_{44} > 0, \quad B_{11} + 2B_{12} > 0 \, . \tag{3.22}$$

Hexagonal finite stress stability conditions[37]

$$B_{11} > |B_{12}|, \quad B_{44} > 0, \quad B_{33}(B_{11} + B_{12}) > 2B_{13}^2 \, . \tag{3.23}$$

3.6.2 Additional data

This section includes plots complementing those in Section III A of the main paper on phonons in wurtzite and zinc blende GaN, showing pressure-driven behavior at elevated temperature or temperature-driven behavior at elevated pressure. A plot showing the universal elastic anisotropy index beyond the regime of elastic stability is also included.

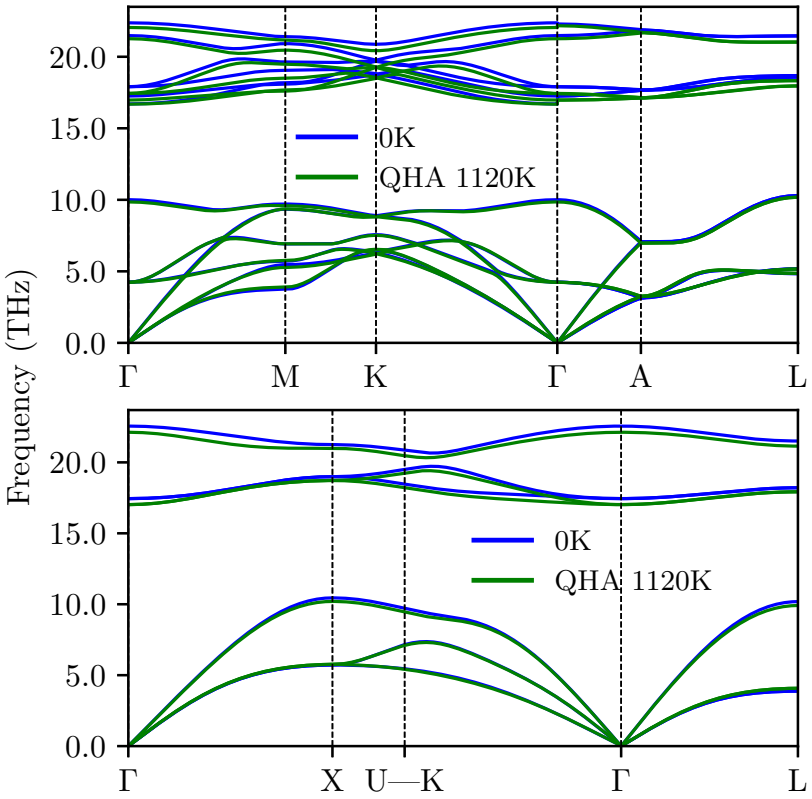

Figure 3.13: Somewhat similar to Fig. 3 of the main paper, phonon dispersions at 0 GPa for wurtzite (top) and zinc blende (bottom) GaN at 0 K (blue) and at 1120 K per a quasiharmonic approximation (green). Differences between the green and blue curves show the effects of temperature-driven volume changes on phonon modes.

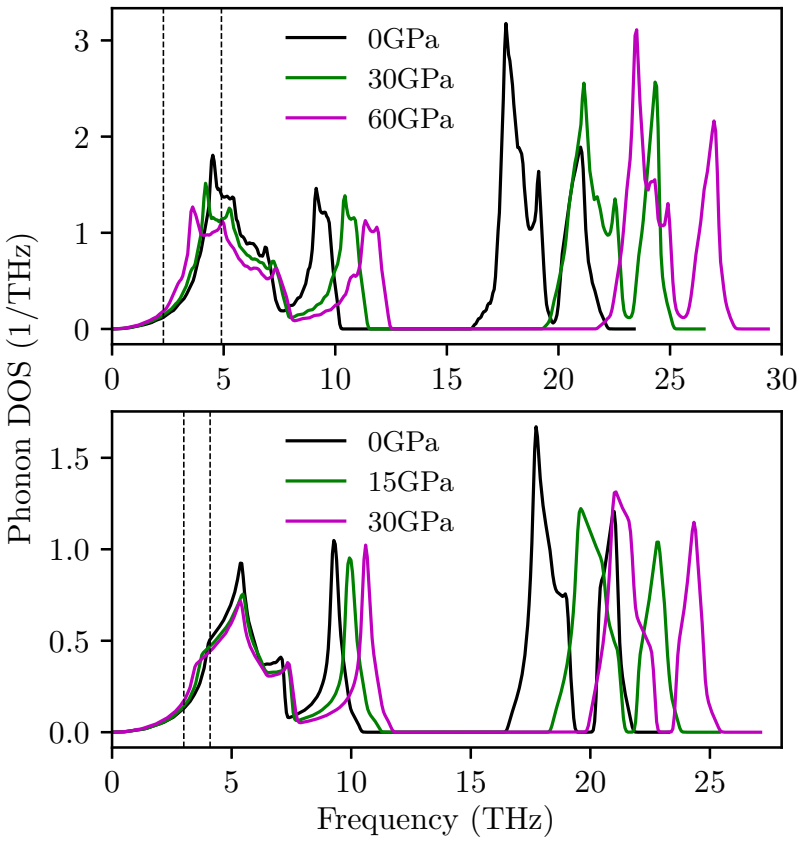

Figure 3.14: Similar to Fig. 5 of the main paper, phonon DOS at 1120 K for wurtzite GaN at 0, 30, and 60 GPa (top) and for zinc blende GaN at 0, 15, and 30 GPa (bottom). Dashed vertical black lines delineate a feature in the DOS that softens with increasing pressure.

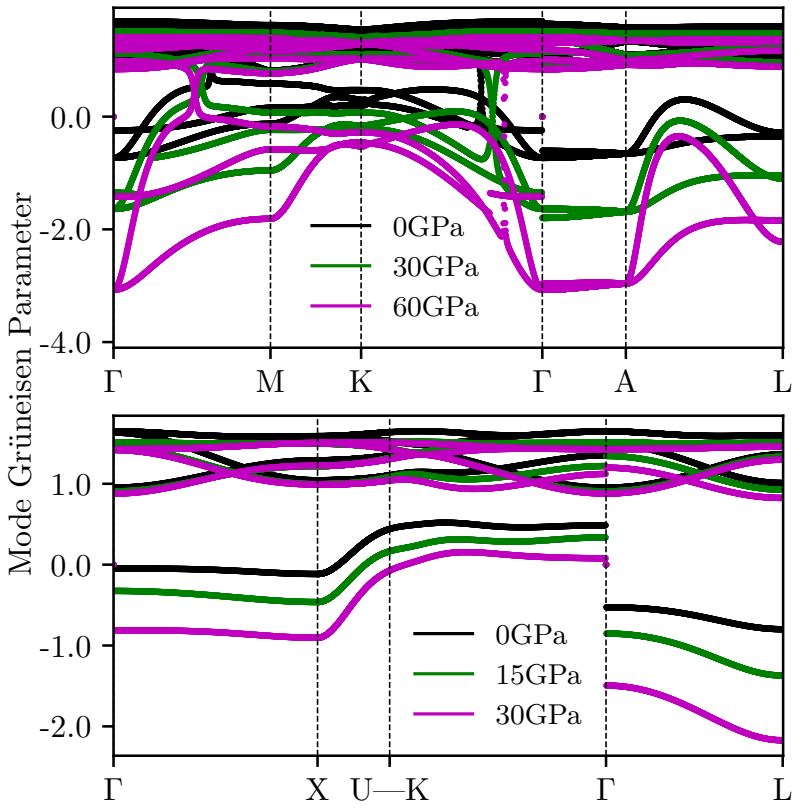

Figure 3.15: Similar to Fig. 6 of the main paper, mode Grüneisen parameters for all phonon branches at 1120 K for various pressures. In both panels, pressure increases from the black to green to pink curves.

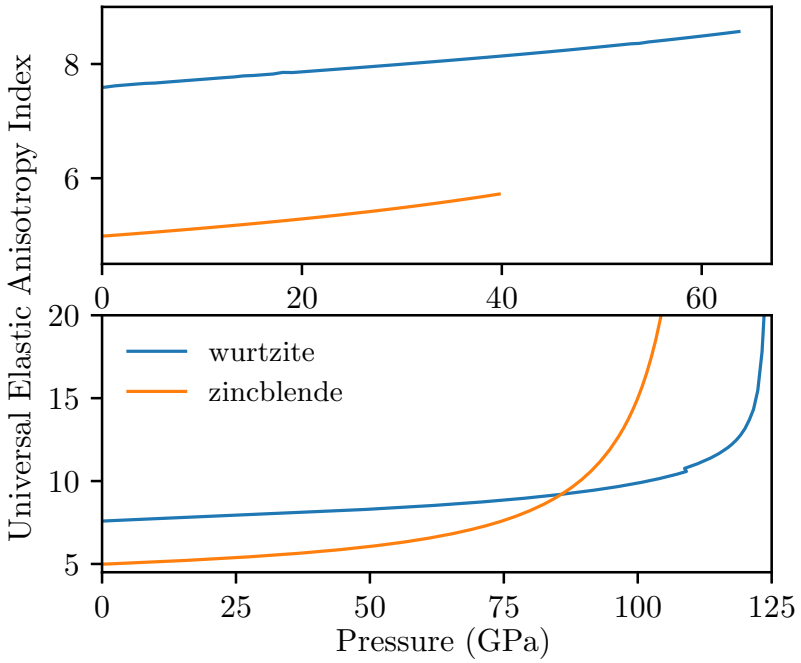

Figure 3.16: The universal elastic anisotropy index A^U of wurtzite and zinc blende GaN vs. pressure in the regime of elastic stability (top), and into the regime of elastic instability (bottom).

Chapter 4

GALLIUM ARSENIDE

4.1 Introduction

Gallium arsenide, GaAs, is a well-studied semiconductor with important technological applications in transistors[42–44], photovoltaic devices[45], and photon detectors[46]. Although less earth-abundant and more expensive than silicon, gallium arsenide offers several advantages. It has a higher electron mobility than silicon, allowing for devices with higher operating frequencies. Today, GaAs dominates the circuitry in critical mobile phone components, such as power amplifiers[47]. Unlike Si, GaAs has a direct bandgap that suppresses phonon creation during photon emission, enabling its use in light emitting diodes (LEDs)[48], laser diodes[49], and optical communications[50]. The bandgap of GaAs is wider than that of Si, making it more resistant to radiation damage, and a more attractive material for satellites[45] and deep space electronics[43].

Like many III-V materials, GaAs is polytypic[51, 52]. It has the zinc blende crystal structure under ambient conditions, but the wurtzite phase is metastable and has been observed experimentally[52] (Fig. 4.1). Both zinc blende and wurtzite crystal structures consist of two interpenetrating face-centered cubic (fcc) or hexagonal close-packed (hcp) sublattices, separately populated by Ga and As atoms (Fig. 4.1). High pressure induces a structural phase transition in zinc blende GaAs to an

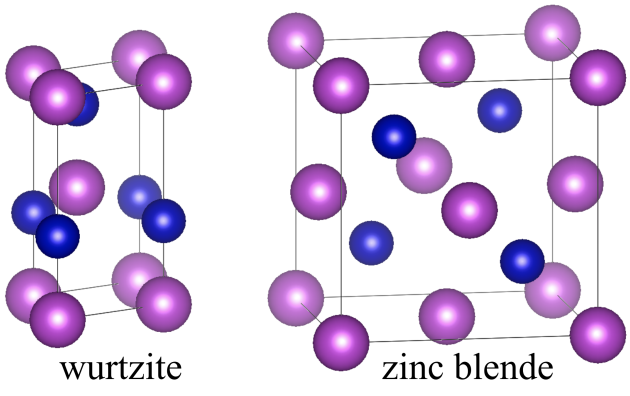

Figure 4.1: Unit cells of wurtzite (left) and zinc blende (right) GaAs. [41] This wurtzite unit cell is primitive; the larger, non-primitive unit cell for zinc blende more clearly shows its cubicity.

orthorhombic structure between 12 GPa[53] and 17 GPa[54].

Modeling thermophysical properties of materials is an important and active part of materials physics and materials engineering. Modeling can enable explorations of extreme conditions, including extreme pressures and temperatures, and quick transversals of parameter spaces. The temperature and pressure evolution of phonon spectra and elastic properties are of interest because they are closely related to the Gibbs free energy and crystal stability. Phonon spectra also offer a microscopic probe into thermal conductivity, thermal expansion, and the temperature dependence of elastic constants. The widely used quasi-harmonic approximation (QHA) extends the harmonic approximation by including effects of volume on phonon frequencies. The QHA ignores explicit anharmonic effects from the anharmonic potentials in which atoms vibrate, where displacements from their equilibrium positions cause forces that do not obey Hooke's law. These anharmonic effects increase with temperature, and can prevent the QHA from correctly modeling thermal expansion[16] or phase stability[17].

Here we report elastic and phonon properties of wurtzite and zinc blende GaAs at simultaneously elevated temperature and pressure. From the elastic constants, we predict changes with pressure of the elastic stability, elastic anisotropy (see Supplemental Information), and anharmonic effects on phonon frequencies and linewidths. Our methods are described in Section 4.2, results in Section 4.3, and the context for, and implications of, these results are given in Section 4.4. Most notably, we report that the lattice stabilities of both wurtzite and zinc blende GaAs are not predicted by the Born stability criteria because the early onset of shorter wavelength phonon instabilities precede elastic collapse. These instabilities are shown to change with temperature owing to effects of phonon anharmonicity. We also report a large effect of pressure on phonon anharmonicity.

4.2 Computational

Projector augmented wave (PAW) potentials and the linear density approximation (LDA) were used in the Vienna Ab-initio Simulation Package (VASP)[4, 5], an implementation of density functional theory (DFT)[18], to perform first principles calculations on GaAs. All calculations used an energy cut-off of 600 eV and a minimum of 13,824 k-points×atoms. The work required calculations for both unit cells and supercells. In wurtzite GaAs, four atom unit (primitive) cells were used with a $20 \times 20 \times 12$ k-point mesh, and supercells of 192 atoms used a $5 \times 5 \times 4$

k-point mesh. In zinc blende GaAs, unit cells with two atoms unit (primitive) cells were used with a $22 \times 22 \times 22$ k-point mesh and supercells with 216 atoms used a $4 \times 4 \times 4$ k-point mesh. The supercells had approximately the same lengths across all three dimensions. The k-point meshes were generated with a Monkhorst-Pack[20] scheme.

For each material, the total energies of static unit cells were calculated with relaxed shapes and ionic positions of varying size, with volumes scaled between approximately 69% and 108% of the equilibrium volume. The resulting energy-volume relationships were used with a Birch-Murnaghan equation of state, allowing the determination of pressure for any volume within this range. The elastic constants for unit cells held at pressures between about –5 GPa and 65 GPa in 0.5 GPa steps were calculated, using stress-strain calculations in VASP through the flag IBRION=6.

With supercells, the phonon properties (phonon dispersion relations, densities of states, and linewidths) of each material were calculated at 0 K, 600 K, and 1200 K for pressures of 0.0, 5.0, 7.5, 10.0, and 15.0 GPa, accounting for both quasiharmonic effects of volume and anharmonic effects of temperature. Separately, phonon properties for these temperatures and pressures were calculated quasiharmonically by ignoring the effects of finite temperature except for thermal expansion. At each temperature, pressure-volume relationships and selected volumes corresponding to each pressure of interest were determined by fitting a Birch-Murnaghan equation of state to Helmholtz free energy versus volume trends of that isotherm. The phonon spectral weight from the small Brillouin zones of the supercells was unfolded into the first Brillouin zone of the primitive cells using tools in the TDEP package[21–23, 55].

Helmholtz free energies, $F(V,T)$, were calculated by summing the ground state total energy surface, $E_0(V)$ (derived from the energy-volume relationships from static unit cells), and the temperature-dependent phonon free energies, calculated at several volumes for a given temperature:

$$F(V,T) = E_0(V) + F_{ph}(V,T) \; . \tag{4.1}$$

We calculated finite temperature phonon properties using the temperature dependent effective potential (TDEP) method[21–23]. For an ensemble of supercells with thermal displacement patterns and their interatomic forces as calculated by VASP,

TDEP generates a model potential energy as

$$U = U_0 + \frac{1}{2!}\sum_{ij\alpha\beta}\phi_{ij}^{\alpha\beta}u_i^{\alpha}u_j^{\beta} + \frac{1}{3!}\sum_{ijk\alpha\beta\gamma}\phi_{ijk}^{\alpha\beta\gamma}u_i^{\alpha}u_j^{\beta}u_k^{\gamma}\ . \tag{4.2}$$

The TDEP method optimizes U_0 and $\phi_{ij}^{\alpha\beta}$ and $\phi_{ijk}^{\alpha\beta\gamma}$, which are interatomic force constants for two- and three-body interactions. These model parameters are chosen to minimize the difference between the set of interatomic forces determined by VASP and those predicted by the model potential of Eq. 4.2. The TDEP calculations used Born effective charge tensors from VASP with the correction scheme of Gonze and Lee[27, 28] to account for long-range interactions in polar GaAs.

A stochastic sampling method (s-TDEP)[24] was used to generate an ensemble of (typically 20 to 40, depending on structural symmetries and temperature) supercells with thermal atomic displacements. The scheme generates position vectors for the i^{th} atom, $\{\vec{u}_i\}$, consistent with phonon displacements and Bose-Einstein statistics

$$\vec{u}_i = \sum_{s=1}^{3N_a}\vec{\epsilon}_{is}\,\langle A_{is}\rangle\,\sqrt{-2\ln\xi_1}\,\sin 2\pi\xi_2\ , \tag{4.3}$$

where $\{\vec{\epsilon}_{is}\}$ are the eigenvectors corresponding to the $\{s\}$ phonon modes in a system of N_a atoms. The embedded expression $\sqrt{-2\ln\xi_1}\sin 2\pi\xi_2$ is a Box-Muller transform generating a random variable with a standard normal distribution, given two uniformly distributed random numbers, ξ_n, between 0 and 1. Finally, $\langle A_{is}\rangle$ [56, 57] is the temperature-dependent expectation value of the normal mode amplitude of the s^{th} phonon mode of the i^{th} atom, given by

$$\langle A_{is}\rangle = \sqrt{\frac{\hbar(2n_s+1)}{2m_i\,\omega_s}}\ , \tag{4.4}$$

which in the classical limit becomes

$$\langle A_{is}\rangle \approx \frac{1}{\omega_s}\sqrt{\frac{k_BT}{m_i}}\ , \tag{4.5}$$

where ω_s and n_s are the eigenvalue and thermal occupation of the s^{th} phonon mode and m_i is the mass of the i^{th} atom.

Each atomic displacement, $\vec{u}_i$, is therefore a thermally-weighted superposition of all vibrational modes, with randomness injected to simulate sampling atomic positions at different times. Zero-point contributions are included with Eq. 4.4 [58]. Generating these atomic positions requires prior knowledge of the phonon mode eigenvectors

and eigenvalues, accessible given interatomic force constants. We therefore began by seeding these calculations with force constants either from frozen phonon calculations or pre-existing work on similar systems; phonon calculations consisting of stochastically-generated ensembles were then performed for two to four iterations until the interatomic force constants converged.

4.3 Results

Figure 4.2 presents elastic constants for wGaAs (panels (a)-(e)) and zGaAs (panels (f)-(h)) as functions of pressure. These results were obtained from VASP without accounting for any temperature effects, i.e., from relaxed unit cells with volumes at each pressure determined by a Birch-Murnaghan equation of state fit to energy-volume relationships that did not account for any phonon free energy. The elastic constants for both materials increase with pressure, except for C_{44}, which decreases.

We do not show values for C_{11} and C_{12} between about 15 and 20 GPa in wGaAs, for reasons that will be explained below using Figs. 4.4 and 4.5. Figure 4.3 presents results pertaining to elastic stability that derive from the elastic constants shown in Fig. 4.2. As for C_{11} and C_{12} in Fig. 4.2, we do not plot real data from about 15 to 20 GPa in Fig. 4.3.

We predicted when wGaAs and zGaAs would become elastically unstable using Born stability criteria that account for pressure[34–37]. The three stability conditions that must be met for cubic crystals such as zinc blende are

$$B_{11} - B_{12} > 0,\ B_{44} > 0,\ B_{11} + 2B_{12} > 0\,, \tag{4.6}$$

and for hexagonal crystals such as wurtzite

$$B_{11} - |B_{12}| > 0,\ B_{44} > 0,\ B_{33}(B_{11} + B_{12}) > 2B_{13}^2\,. \tag{4.7}$$

The elastic stiffnesses B_{ij} are the corresponding values of elastic constants C_{ij} with pressure

$$B_{ii} = C_{ii} - P,\ i = 1, 2, ...6\,, \tag{4.8}$$

$$B_{1j} = C_{1j} + P,\ j = 2, 3\,. \tag{4.9}$$

The third stability conditions of Eqs. 4.6 and 4.7 remain true across our entire pressure range of 0 to 65 GPa for both wGaAs and zGaAs. Figure 4.3 shows the first two Born instabilities in wGaAs and zGaAs. The first stability condition fails when $B_{11} - B_{12}$ ($B_{11} - |B_{12}|$ for wurtzite) falls to zero. Similarly, the second stability

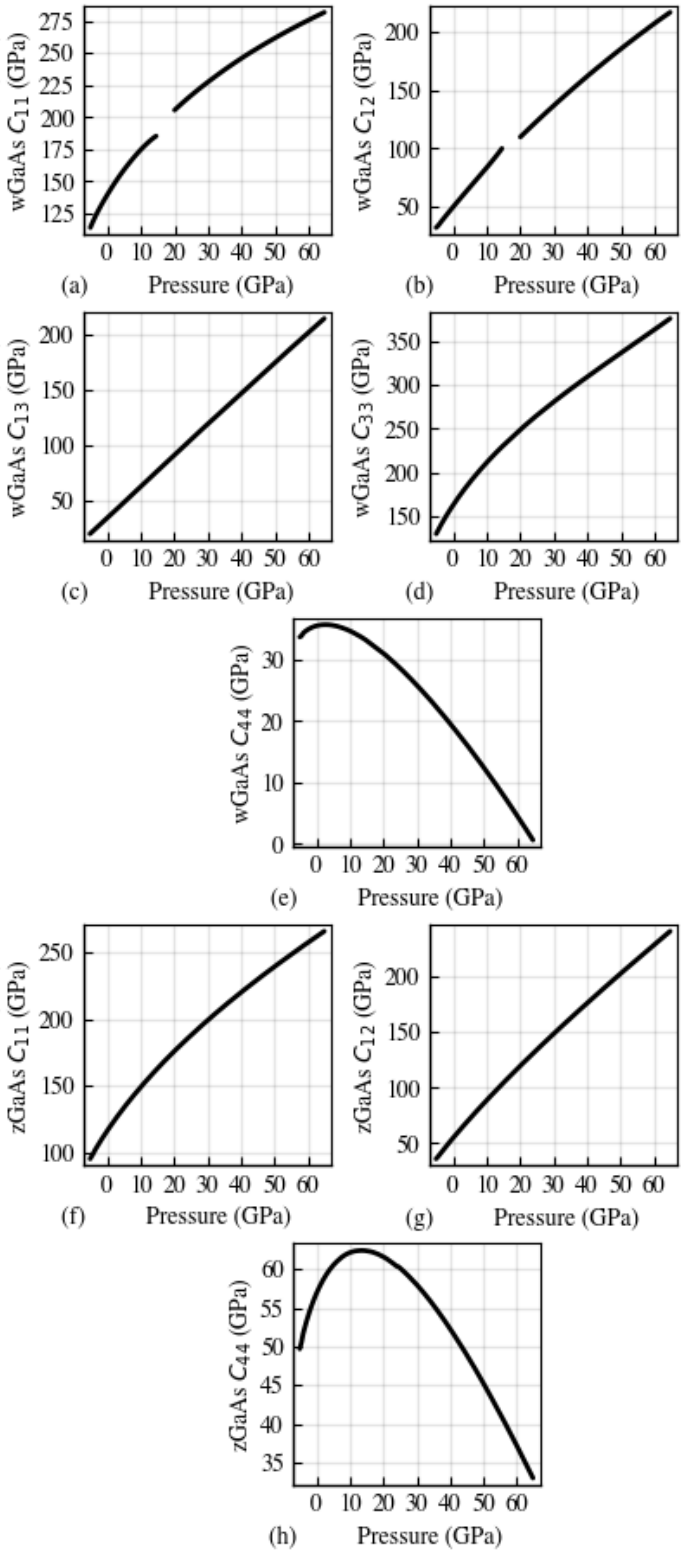

Figure 4.2: Elastic moduli in GPa plotted versus pressure, also in GPa, for wGaAs (panels (a) to (e)) and for zGaAs (panels (f) to (h)). For C_{11} and C_{12} in wGaAs, we have omitted data from approximately 15 to 20 GPa, where evidence of a phonon instability emerges, as shown in Fig. 4.4, to artificially decouple results on the elastic properties from this instability.

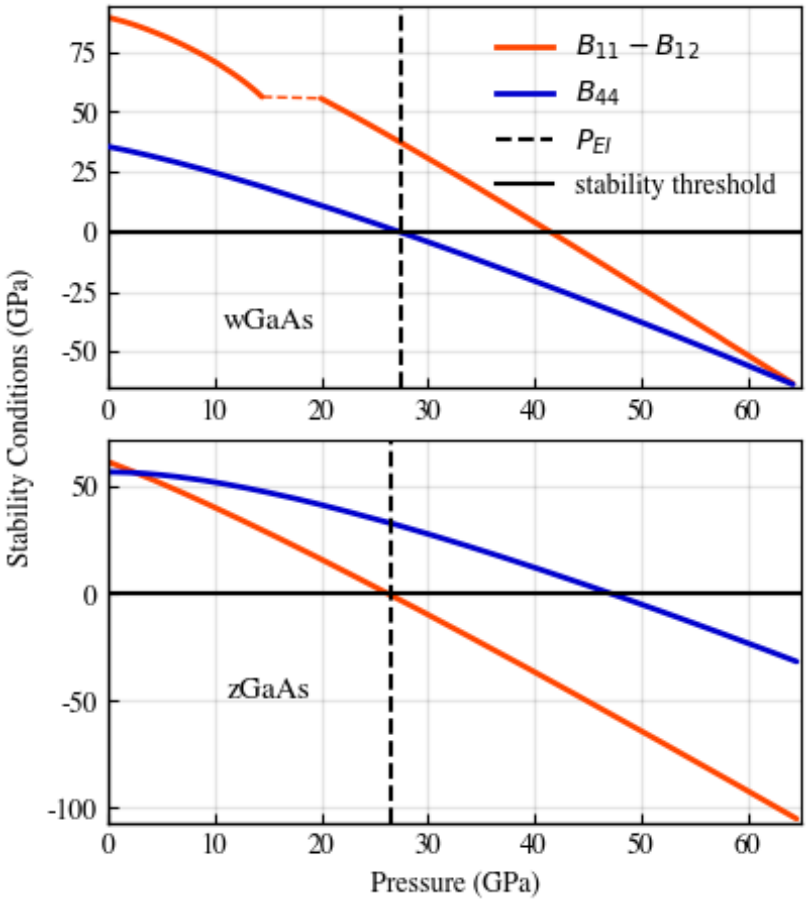

Figure 4.3: Illustration of the first two Born stability criteria versus pressure for wGaAs (top) and zGaAs (bottom). The dashed orange line is a guide to the eye spanning the region where data has been omitted from Fig. 4.2 for C_{11} and C_{12}. A dashed vertical black line at 27 GPa, labeled P_{EI}, indicates the pressure at which elastic instability occurs in each phase.

condition fails when B_{44} crosses zero. According to the Born stability criteria, both wGaAs and zGaAs become unstable at 27 GPa, denoted by the vertical dashed lines. For wGaAs this occurs when B_{44} falls to zero; for zGaAs there is a "tetragonal shear instability"[36] that occurs when B_{12} becomes greater than B_{11}.

Finally we address the omitted data from 15 to 20 GPa in the trends for C_{11} and C_{12} of wGaAs in Fig. 4.2, and phonon phenomena in this range of pressure. Panels (a) and (b) of Fig. 4.4 show the full pressure trends for C_{11} and C_{12} of wGaAs. Between 15 to 20 GPa, C_{11} exhibits an anomalous dip; simultaneously C_{12} exhibits an anomalous spike. While the observed dip and spike are themselves non-physical, they reflect a phonon instability. The dip and spike are side effects of the way VASP calculates elastic constants. With IBRION = 6, VASP distorts the crystal unit

cell and obtains the elastic constants from the resulting stress-strain relationships. The output is a version of the elastic tensor containing symmetrized elastic moduli. However, these symmetrized elastic moduli do not account for the fact that the ionic positions of the unit cell are no longer relaxed once each distortion is applied. To correct for this, VASP calculates the contribution to the elastic tensor from ionic relaxation and adds this contribution to the symmetrized elastic moduli, giving the total elastic moduli. VASP calculates the contributions from the ionic relaxation using a dynamical matrix constructed from phonon frequencies at the Γ point. In wGaAs, the dip in C_{11} and spike in C_{12} correspond to the contributions to elastic moduli from ionic relaxation. These contributions to the ionic relaxation are made nonphysical by a phonon instability as seen in Fig. 4.4, panels (c) and (d), where the phonon frequencies for the lowest energy transverse optical modes at Γ become imaginary at 20 GPa.

More direct evidence of phonon instabilities occurring at pressures below the Born instabilities is seen in Fig. 4.5, where phonon dispersions are shown for wGaAs and zGaAs. In wGaAs we see significant phonon softening with pressure, not only for the lowest frequency transverse optical modes at Γ, but also from the transverse acoustic mode at M. At both these phonon wavevectors, the modes soften until their frequencies go imaginary. Figure 4.5 presents the onset of phonon instability at the M point only, showing that it occurs at a lower pressure than the phonon instability at Γ. The first phonon instability in wGaAs occurs at about 18 GPa. Similarly, in zGaAs there is a large softening of transverse acoustic modes at X and at L. In zGaAs the first phonon instability occurs at X, near 20 GPa. Because zGaAs exhibits no phonon instability at Γ and only Γ frequencies contribute to determinations of the elastic constants in VASP, no strange discontinuities are observed in the elastic constants of zGaAs in Fig. 4.2.

The temperature dependence of the Grüneisen parameters of the unstable phonon modes are shown in Fig. 4.6. At 0, 600, and 1200 K, the Grüneisen parameters for the lowest-energy transverse acoustic modes at the M point in wGaAs and at X in zGaAs are negative. They become increasingly negative with pressure, meaning that their frequencies become more sensitive to pressure, accelerating the onset of instability. At higher temperatures, the Grüneisen parameters of these modes are smaller in magnitude, and change less rapidly with increasing pressure. Because the pressure sensitivities of these phonon frequencies decrease with temperature, the onsets of the phonon instabilities are shifted to higher pressures at higher temperatures.

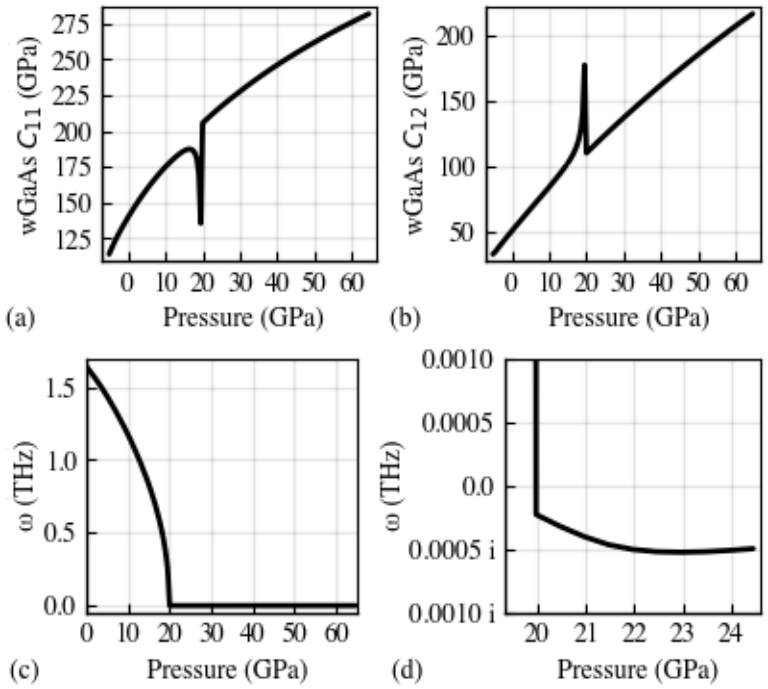

Figure 4.4: In panels (a) and (b), C_{11} and C_{12} are plotted against pressure for wGaAs without omitting data from 15 to 20 GPa as done in Fig. 4.2. The respective dip and spike shown correspond to contributions to these elastic moduli that scale roughly inversely with certain Γ-point phonon frequencies as they approach zero. Below, in (c) and (d), frequencies for the degenerate transverse optical phonon modes at Γ are plotted against pressure. Panel (c) shows that these phonon modes soften considerably until approaching 0 THz at 20 GPa. In (d) an expanded plot shows us that at 20 GPa frequencies for this phonon mode become imaginary, giving the onset of a phonon instability.

Figure 4.7 shows the phonon densities of states for wGaAs and zGaAs. Each panel shows the phonon DOS at 0 K, at 1200 K from the QHA, and at 1200 K with both quasiharmonic and explicitly anharmonic effects. At 0 GPa, the quasiharmonic phonon DOS at 1200 K is more similar to the phonon DOS at 1200 K with explicit anharmonicity than it is to the phonon DOS at 0 K. At 10 GPa, this is no longer true and the quasiharmonic phonon DOS at 1200 K are much more similar to results at 0 K than at 1200 K. At elevated pressure, the QHA becomes less effective at approximating the effects of temperature.

Figure 4.8 shows that the effects of pressure on thermal phonon linewidths are mode-dependent. Here we overlay phonon dispersions for wGaAs and zGaAs, respectively, with pressure and temperature dependent broadening at 1200 K and 0 and 10 GPa. The thicknesses of the phonon branches are the phonon linewidths.

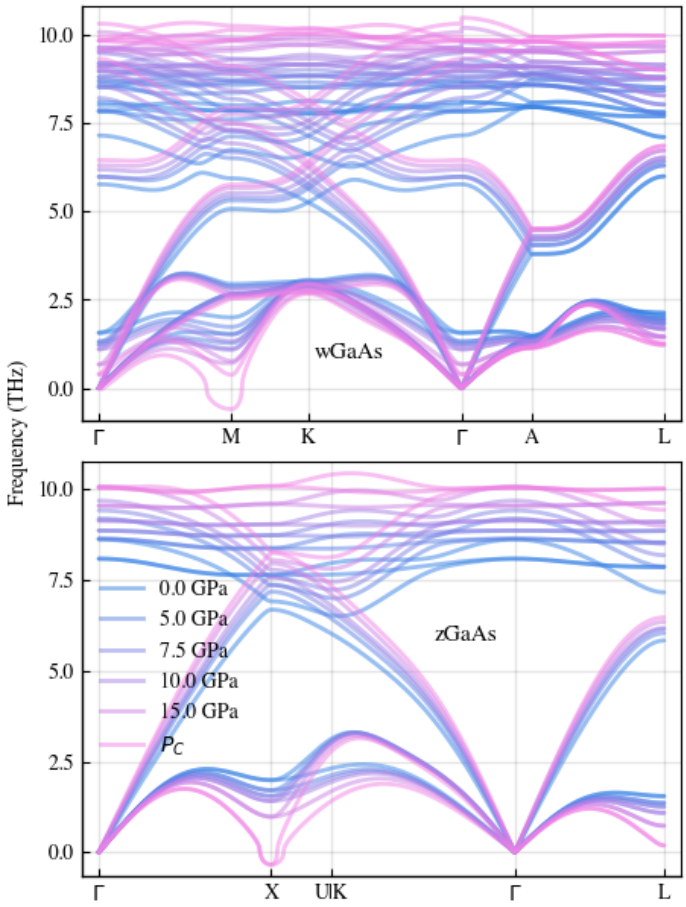

Figure 4.5: Phonon dispersion relations at 0 K for wGaAs (top) and zGaAs (bottom) with frequencies on the vertical axis plotted against phonon wavevectors along high symmetry directions. Phonon dispersion relations at various pressures are overlaid, with increasing pressure from blue to purple to pink. In wGaAs, we see pressure-induced softening of the longitudinal acoustic mode at M and of the degenerate transverse optical modes at Γ, until an instability occurs around 18 GPa at M, denoted by P_C. In zGaAs, the transverse acoustic modes soften at X and L with increasing pressure, until a phonon instability occurs around 20 GPa at X.

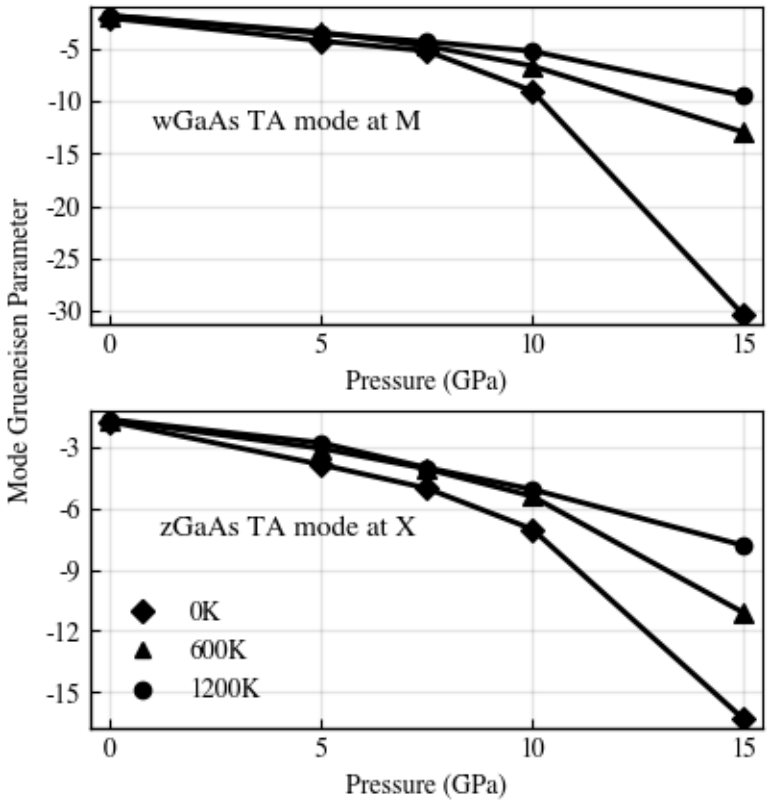

Figure 4.6: Mode Grüneisen parameters that are the most sensitive to volume changes are plotted against pressure for 0, 600, and 1200 K in wGaAs (top) and zGaAs (bottom).

(The linewidths are nearly 0 THz at 0 K in both materials.) The purple and gray lines in each panel show the broadening at 1200 K for 0 GPa and at 1200 K for 10 GPa, respectively. Increasing the pressure at high temperature causes the spectral shape of some phonon modes to broaden in energy, and others to narrow. In wGaAs, for example, the broadening of modes at Γ near 5 THz decreases with pressure, whereas the broadening of modes at A near 4 THz increases with pressure. Similarly in zGaAs, pressure can cause broadening to increase, as at X near 7 GPa, or to decrease, as at L near 5 THz.

Figure 4.9 compares the average effect of pressure on phonon broadening in wGaAs and zGaAs to that in wGaN and zGaN, using data from our previous work[59]. The graph shows the ratio of the values between high pressure and low pressure of the average phonon linewidths. The average linewidth was from all phonon branches across the high symmetry paths in the dispersion curves of Fig. 4.8. In wGaAs and zGaAs, our high and low pressures are 10 GPa and 0 GPa; in wGaN and

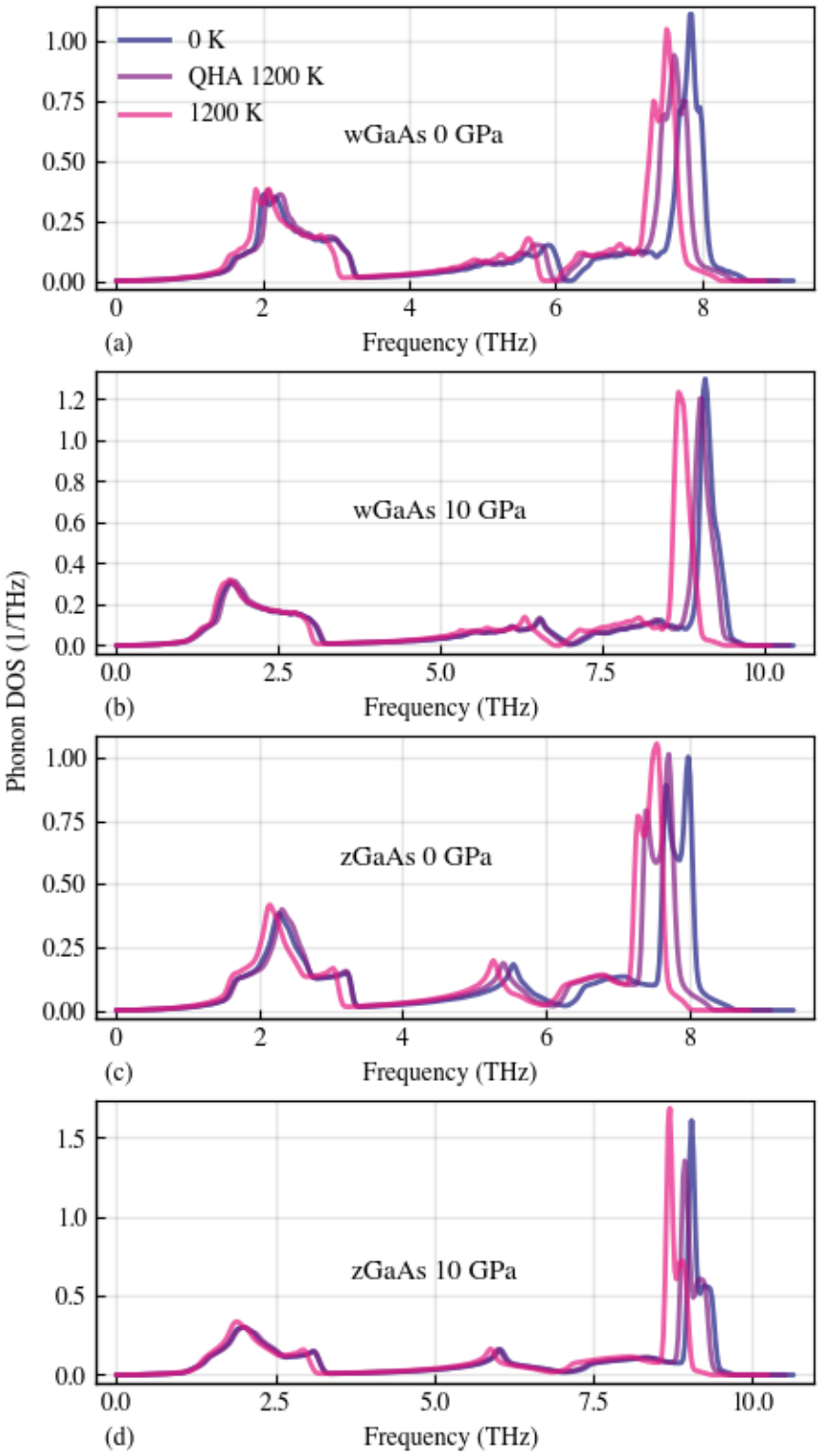

Figure 4.7: Overlays of phonon DOS at 0 K and at 1200 K per a QHA and with full anharmonic phonon effects are shown at (a) 0.0 GPa in wGaAs, (b) 10.0 GPa in wGaAs, (c) 0.0 GPa in zGaAs, and (d) 10.0 GPa in zGaAs. At elevated pressures, the QHA is less reliable for predicting thermal shifts.

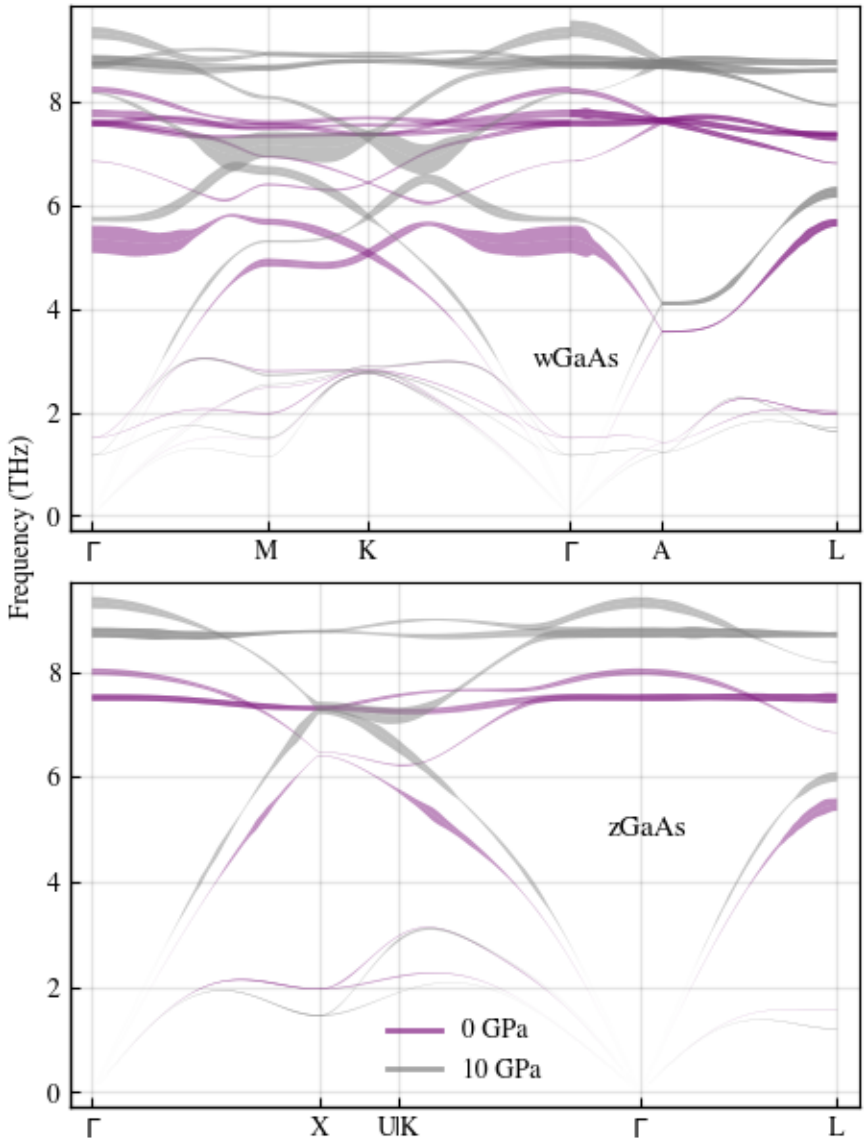

Figure 4.8: Calculated spectral weights showing phonon dispersions for wGaAs (top) and zGaAs (bottom), showing broadening from phonon-phonon processes at 1200 K for 0.0 GPa (purple) and 10.0 GPa (gray).

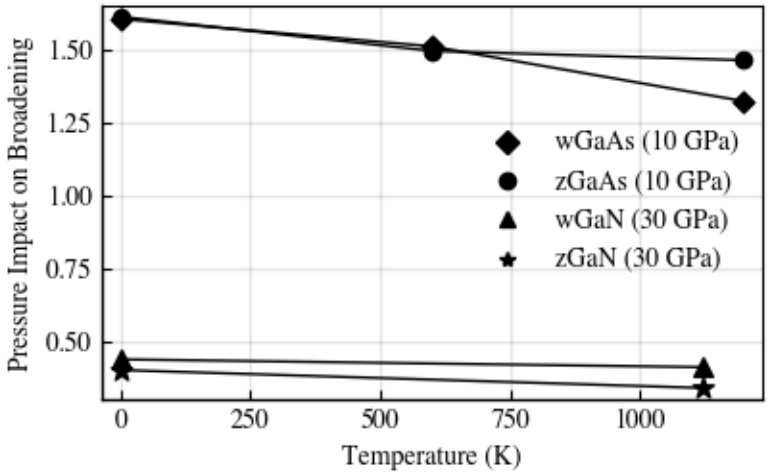

Figure 4.9: The factor by which average linewidth across high symmetry paths for all phonon branches changes with a pressure of either 10 GPa (GaAs) or 30 GPa (GaN)[59] versus temperature for wGaAs, zGaAs, wGaN, and zGaN. Values greater than 1 show that pressure increases broadening. Values less than 1 indicate that pressure decreases broadening.

zGaN they are 30 GPa and 0 GPa. For both wGaAs and zGaAs, this ratio is greater than 1 for 0, 600, and 1200 K and modestly decreases with temperature, indicating a temperature-dependent increase in broadening with increasing pressure. Conversely in both wGaN and zGaN, this ratio is smaller than 1 at both 0 and 1120 K, indicating a decrease in thermal phonon broadening with increasing pressure.

4.4 Discussion

4.4.1 Elastic properties and origin of lattice instability

The Born stability criteria implicitly account for the behavior of long-wavelength acoustic phonon modes near Γ, but assume the stability of shorter-wavelength phonon modes. There is a correspondence between elastic constants and interatomic force constants in the long wavelength limit. As explained in other work [2, 60], the elastic constants can be used to construct an analog to the dynamical matrix, $\mathbf{A}(\vec{q})$

$$A_{ij}(\vec{q}) = \sum_{kl} C_{ikjl} q_k q_l \ , \tag{4.10}$$

where $\vec{q}$ is a point in reciprocal space and C_{ikjl} is an element of the elastic tensor, equivalent in Voigt notation to C_{ij}. The linear eigenvalue equation

$$\mathbf{A}(\vec{q})\vec{u}(\vec{q}) = \rho\omega^2(\vec{q})\vec{u}(\vec{q}) \ , \tag{4.11}$$

holds near $\vec{q}$=0, giving frequencies of long wavelength phonon modes, scaled by the density ρ, where $\vec{u}(\vec{q})$ is the corresponding eigenvector at $\vec{q}$.

In wGaAs a phonon instability occurs near the Γ-point. It is revealed by imaginary frequencies in Eq. 4.11, and gives a strange dip and spike in C_{11} and C_{12} at 20 GPa when VASP calculates elastic constants. Nevertheless, these transverse acoustic modes at Γ are not the first to become unstable in wGaAs. The first instability is at 18 GPa in the transverse acoustic modes at M. This is evident in the phonon dispersions in Fig. 4.5, but not in the elastic constants of Figs. 4.2 or 4.3 (because VASP reports and uses Γ frequencies but not others to calculate C_{ij}). This phonon instability in wGaAs at 18 GPa is approximately 9 GPa below the Born instability at 27 GPa. In zGaAs, the first instability occurs at 20 GPa for a transverse acoustic mode at X. By examining the eigenvectors of the unstable transverse mode at M in wGaAs, we found that it has atom displacements in the basal plane, perpendicular to the z-direction. Likewise, the unstable transverse acoustic mode in zGaAs at L has atom displacements in its close-packed {111} planes. Other reports that short wavelength modes can become unstable before the onset of Born instabilities include Refs. [61, 62], and an older analysis with Morse potentials predicted that this would cause amorphization of GaAs [63].

It is interesting to compare these results on GaAs to the elastic properties of wurtzite and zinc blende gallium nitride, GaN. In contrast to wGaAs and zGaAs, wGaN and zGaN did not exhibit phonon instabilities prior to the onset of Born instabilities. The phonon modes that soften to zero in GaAs under pressure show only a small tendency towards softening for both wGaN and zGaN. A trend, or at least a mnemonic, is that the closer match of atom sizes in GaAs causes its close-packed planes to be smoother, with greater tendency for large shears under transverse displacements. Nevertheless, the first Born instability was the same across crystal structures, with wGaAs and wGaN becoming unstable when B_{44} becomes nonpositive, and zGaAs and zGaN exhibiting a tetragonal shear instability[59].

4.4.2 Coupled effects from pressure and temperature

Temperature effects on pressure-driven lattice instability

Mode Grüneisen parameters, $\{\gamma_i\}$, defined as

$$\gamma_i \equiv \frac{-V}{\omega_i}\frac{\partial \omega_i}{\partial V}\,, \tag{4.12}$$

give the volume sensitivity for the frequency of a phonon mode. In quantifying how phonon frequencies shift with volume, mode Grüneisen parameters provide a way to predict the onset of phonon instabilities in wGaAs and zGaAs by estimating the volumes (and thereby the pressures) at which frequencies become nonpositive (explained further in the Supplemental Information). Qualitatively, Grüneisen parameters of larger magnitude indicate greater sensitivity to pressure, and faster progression towards a lattice instability. Figure 4.6 shows that the negative γ become increasingly negative with pressure for both wGaAs and zGaAs at all temperatures. As pressure is applied, transverse acoustic modes at M in wGaAs and at X in zGaAs accelerate towards instability. This trend is reduced by temperature, however. By extrapolating phonon frequencies with volume, and using Grüneisen parameters from the sTDEP calculations, we estimate that at 0, 600, and 1200 K respectively, the onset of shorter wavelength phonon instabilities will occur in wGaAs at 20, 27, and 30 GPa, and in zGaAs at 25, 30, and 38 GPa.

This temperature dependence is poorly described by the quasiharmonic approximation, which attributes all change in phonon frequencies to changes in volume. Using mode Grüneisen parameters from quasiharmonic phonon calculations at 1200 K (with 1200 K volumes and 0 K potentials), the onset of lattice stability occurs at approximately 23 GPa in wGaAs and at 25 GPa in zGaAs. The QHA accounts for only about 30% and 0% of the temperature-driven elevation in pressure of the lattice instabilities in wGaAs and zGaAs. Explicit anharmonicity in wGaAs and zGaAs dominates the temperature dependence of the phonon instabilities, and increases the pressure range of stability.

The Born stability criteria overestimates the pressure at which instability would occur by several GPa in both wGaAs and zGaAs, according to phonon data at 0 K. Temperature suppresses the phonon instability, and should decrease the elastic constants. We did not calculate the temperature dependence of the elastic constants, so we do not know if the elastic instability from the Born criteria would overtake the phonon instability at temperatures below the melting temperature.

Pressure effects on phonon anharmonicity

The Grüneisen parameters of Eq. 4.12 change with temperature as

$$\frac{\partial \gamma_i}{\partial T} = \gamma_i \left[\beta - \frac{1}{\omega_i} \frac{\partial \omega_i}{\partial T} \right] - \frac{V}{\omega_i} \frac{\partial^2 \omega_i}{\partial T \partial V} , \tag{4.13}$$

so the effect of pressure on individual phonon frequencies is also temperature dependent. (Here β is the coefficient of volume thermal expansion, but it can probably be neglected.) The second and third terms in Eq. 4.13 give phonon frequency shifts proportional to the product $\Delta T \times \Delta P$. (The third term in Eq. 4.13 is also obtained when the pure anharmonicity, proportional to $(\partial\omega_i/\partial T)_V$, has a volume dependence[64].)

If pressure and temperature were to cause additive effects on phonon frequencies, the changes of phonon frequencies and broadenings with temperature should be independent of the effects of pressure, and vice-versa. This is the prediction of the quasiharmonic approximation (QHA), where all frequency shifts depend only on volume. However, Fig. 4.7 shows that a temperature of 1200 K causes shifts in the phonon spectra that differ between the QHA and the full sTDEP calculations, and furthermore, these discrepancies increase with pressure for both wGaAs and zGas. The QHA phonon spectra at 1200 K become more similar to 0 K phonon spectra at 10 GPa than at 0 GPa. This is an effect of reduced thermal expansion at elevated pressures.

Figure 4.8 shows that the effects of pressure on the thermal broadening of phonon spectra are not simple. Adding 10 GPa of pressure at 1200 K changes the phonon linewidths, but with mixed results; sometimes pressure increases the magnitude of the thermal broadening, but sometimes pressure decreases the phonon broadening, indicating the disappearance of previously accessible phonon decay channels. (Phonon linewidths, which are inversely proportional to phonon lifetimes, reflect the availability of opportunities for phonons to decay into combinations of lower frequency modes. The QHA does not account for broadenings of phonon spectra.) If all phonon modes had the same Grüneisen parameter, pressure would cause a proportional shift in all phonon dispersions. In this hypothetical case, the downscattering channels would remain unchanged, and the phonon anharmonicity would be unchanged by pressure. For both zGaAs and wGaAs the effect of pressure is quite different for the transverse acoustic branches and all others, which have negative and positive Grüneisen parameters, respectively. Pressure-induced changes to the phonon dispersions cause the three-phonon processes to change, thus changing the phonon anharmonicity.

Examples of how pressure alters downscattering channels are shown in Fig. 4.10. Pressure changes both the "source" modes, depicted as four-point stars, and the "destination" modes, the thick dots (that appear as short, thick purple and gray lines).

The source modes are kept at the same k-vector, but as their frequencies increase with pressure, energy and momentum conservation cause substantial changes in the allowed k-vectors of the destination modes. In wGaAs, a source mode is shown near M along the path from Γ, $[0,0,0]$, to M, $[\frac{1}{2},0,0]$, and another near K along the path from Γ to K, $[\frac{2}{3},\frac{-1}{3},0]$. Each of these source modes decays into two destination modes along the same high symmetry direction — one just under 6 THz and one near 1 THz. (There are several destination modes near 6 THz, each with a partner mode near 1 THz.) In zGaAs, longitudinal acoustic source modes are shown near K along the path from K ($[\frac{3}{8},\frac{3}{8},\frac{3}{4}]$ in zinc blende) to Γ, and near L along the path from Γ to L at $[\frac{1}{2},\frac{1}{2},\frac{1}{2}]$. Each of these source modes can decay into one longitudinal acoustic mode on the same branch and one transverse acoustic mode along the same high symmetry direction, but these destination modes change significantly with pressure. On the other hand, the decay channels for the source modes in zGaAs near L do not change much with pressure. The source modes have, of course, additional destination modes that lie off the high symmetry directions, but these examples are typical in that they show the mode-to-mode variations of how pressure alters the anharmonicity. More detail is presented in a table in the Supplemental Information[].

Figure 4.9 shows that pressure increases the average thermal broadening in wGaAs and zGaAs at all temperatures. In contrast, for wGaN and zGaN, pressure decreases the average phonon linewidth. Both wGaN and zGaN have a phonon bandgap that increases with pressure. For GaN, increasing the distance between acoustic and optical modes leaves the optical modes with fewer combinations of acoustic modes into which they can decay, increasing phonon lifetimes and making GaN more harmonic with pressure, in contrast to GaAs.

4.5 Conclusions

The phonons and elastic properties of GaAs were calculated at simultaneous temperature and pressure using sTDEP, a fully anharmonic method, and the approximate quasiharmonic method (QHA, where all changes are attributed to effects of volume). It was found that the Born stability criteria, which implicitly account for the behavior of long wavelength phonon modes near Γ, are not the appropriate criteria for the lattice stability of either wGaAs or zGaAs because shorter-wavelength phonon instabilities occurred at lower pressures. In particular, the pressure-induced softening of transverse acoustic modes at the M and X points in k-space cause lattice instabilities in wGaAs and zGaAs at 18 and 20 GPa at 0 K, whereas the Born stability criteria

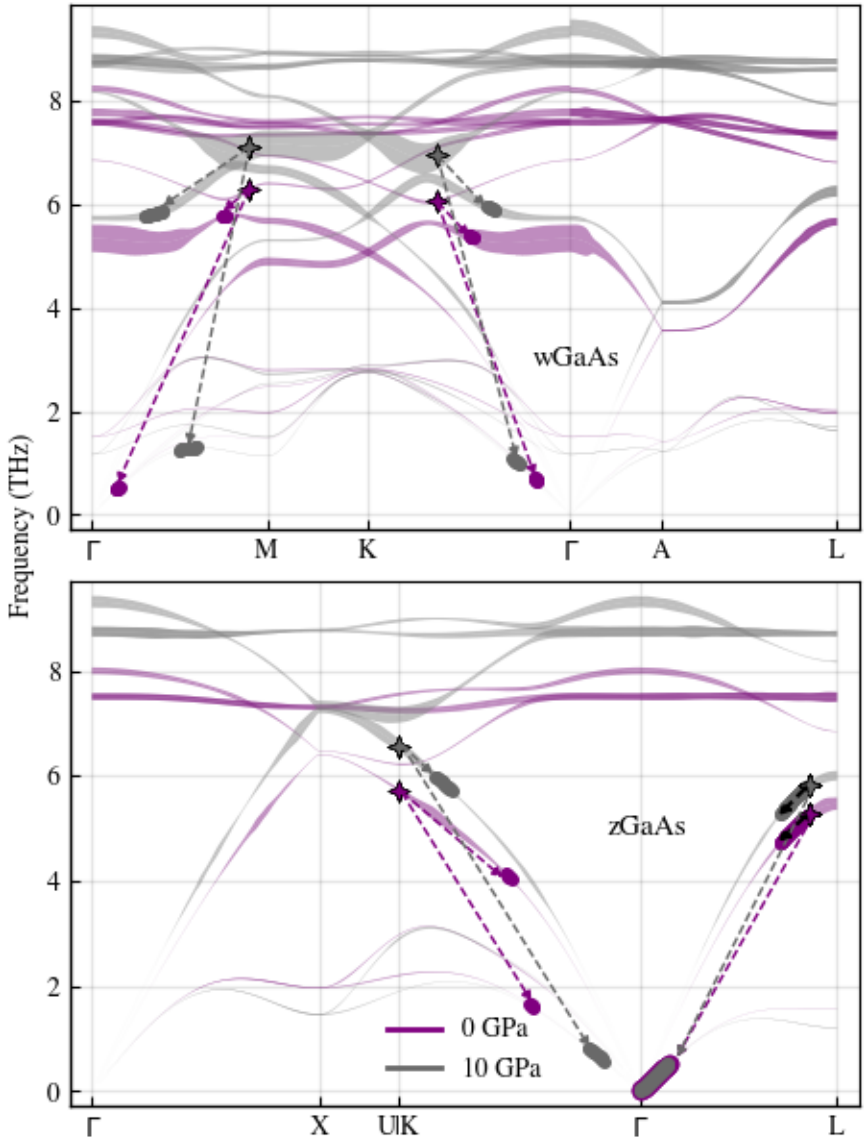

Figure 4.10: Examples of decay channels that conserve crystal momenta and energy in downscattering. Pairs of source modes are marked by four-point stars, and dashed arrows point from source modes to their various decay products, shown as circular points. These modes overlay the phonon dispersions of Fig. 4.8. These three-phonon processes are changed by pressure.

predict lattice stability until 27 GPa in each material. Temperature causes a significant stabilization of these phonon modes, however, slowing their softening with pressure. The mode Grüneisen parameters depend significantly on temperature, causing changes in thermophysical properties that depend on the product $\Delta T \times \Delta P$.

Pressure-temperature coupling changed the anharmonic thermal broadening of phonon modes. On average for GaAs, pressure tends to increase the thermal broadening between 0 and 1200 K. The independent shifts of phonon branches induced by pressure tend to increase the number of phonon-phonon interactions and phonon linewidths at 1200 K by creating more downscattering channels for phonon decay. In comparison to GaN with the same crystal structures, pressure had a larger effect on the average phonon broadening in GaAs than in GaN, with GaN becoming more quasiharmonic with pressure, but GaAs less so. Although the Born criteria for elastic instability failed similarly in both GaAs and GaN, for GaN the Born instabilities occur at pressures before the onset of phonon instabilities.

4.6 Supplemental Information for Phonon thermodynamics and elastic behavior of GaAs at high temperatures and pressures

4.6.1 Elastic anisotropy

In Fig. 4.11 the universal elastic anisotropy index[32], A^U, derived from elastic constants, is shown as a function of pressure in wGaAs (purple) and zGaAs (blue). As in Figs. 4.2 and 4.3 of the main paper, a dashed line spanning the region between 15 and 20 GPa for wGaAs is a guide to the eye where real data has been omitted for the purpose of decoupling elastic constant calculations from the onset of a shorter wavelength phonon instability. A^U quantifies elastic anisotropy via

$$A^U = 5\frac{G_V}{G_R} + \frac{K_V}{K_R} - 6\,, \tag{4.14}$$

where K and G are the bulk and shear moduli, and subscripts R and V denote Reuss and Voigt bounds on these quantities, respectively. While Reuss places lower limits on these quantities by assuming uniform stress, Voigt defines upper bounds on these quantities by assuming the material is under constant strain[33]. In a perfectly elastically isotropic crystal, Reuss and Voigt bounds are equivalent and A_U is 0. Unlike more commonly used metrics for quantifying elastic anisotropy like the Zener ratio, A^U is independent of crystal structure.

Figure 4.11 shows that elastic anisotropy increases with pressure in both wGaAs and zGaAs. On the left we see that zGaAs is more elastically anisotropic at low pressures

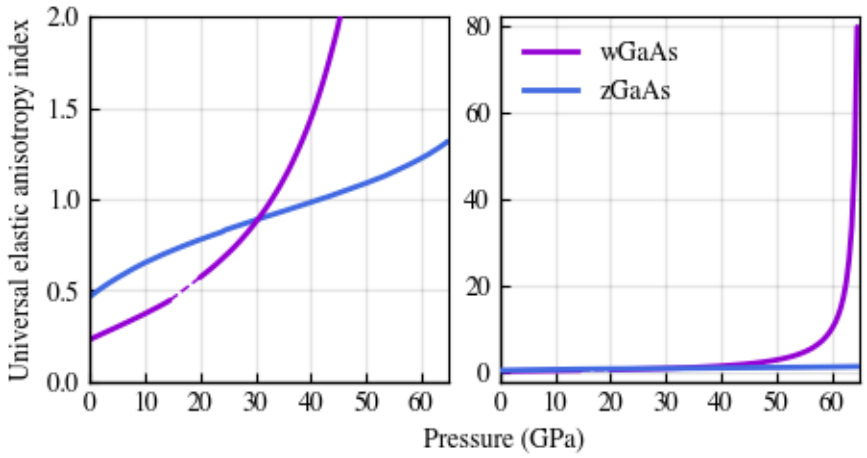

Figure 4.11: Values for the universal elastic anisotropy index versus pressure for wGaAs in purple and zGaAs in blue. Elastic anisotropy increases with pressure for both materials, with zGaAs exhibiting greater elastic anisotropy than wGaAs in the regime where both phases are metastable. The dashed line in purple from 15 to 20 GPa spans the region of omitted data for C_{11} and C_{12}, as shown in Fig. 4.2.

but wGaAs becomes more anisotropic at 30 GPa. Elastic anisotropy increases with pressure exponentially in wGaAs. The graph at right shows how A^U for wGaAs far exceeds the elastic anisotropy of zGaAs with increasing pressure.

Prior to the onset of instability, Fig. 4.11 shows that zGaAs is more elastically anisotropic than wGaAs. This is unlike the trend seen in GaN, where the wurtzite form, wGaN, was more elastically anisotropic than the zinc blende form, zGaN. Like the wurtzite and zinc blende forms of GaN, wGaAs and zGaAs become less elastically isotropic with increasing pressure. Nevertheless, we found wGaAs and zGaAs to be much less elastically anisotropic than GaN; even by the upper bound of lattice stability in wGaAs and zGaAs, the values for A^U in GaAs are approximately an order-of-magnitude smaller than those in GaN at 0 GPa[59].

4.6.2 Purely temperature-driven anharmonicity

Figure 4.12 presents phonon dispersion relations for wGaAs and zGaAs at 0 and 1200 K, showing the effect of temperature on phonon frequencies; in each panel, differences between the blue and magenta curves indicate temperature-driven phonon frequency shifts. Across high symmetry directions, all phonon branches soften or do not change with temperature. In particular, the phonon modes that drive instability in each material do not seem to change with temperature between 0 and 1200 K.

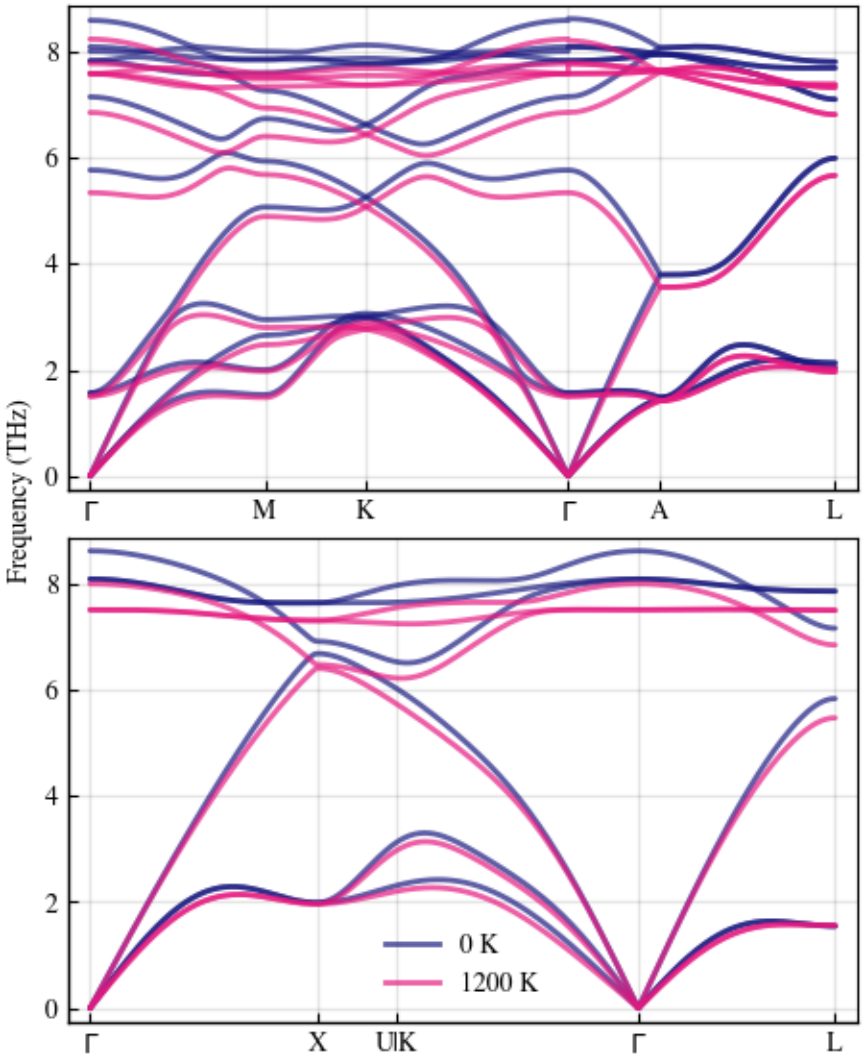

Figure 4.12: Effect of temperature on the phonon dispersion relations of wGaAs (top) and zGaAs (bottom) at 0.0 GPa. For all phonon modes, temperature either has no effect, or induces softening, as the red curves are at lower frequencies than the purple curves.

4.6.3 Pressure-induced frequency shifts

Figure 4.13 compares the effects of pressure on phonon spectra of both wGaAs and zGaAs. All panels show overlays of phonon spectra at pressures of 0.0, 5.0, and 10.0 GPa, all at 0 K. Panels (a) and (c) show phonon densities of states (DOS) for wGaAs and zGaAs, respectively, while (b) and (d) show phonon dispersions. Panels (a) and (c) show that higher frequency phonon modes shift even higher with increasing pressure. In contrast, lower frequency modes (i.e., below 4 THz) shift to even lower frequencies with increasing pressure, indicating negative Grüneisen parameters for some phonon modes. Panels (b) and (d) show more about the pressure-induced frequency shifts of modes along high symmetry directions. In wGaAs, the strongest softening with pressure occurs for the transverse acoustic modes at the M point and the lowest frequency transverse optical modes at Γ, each around 2 THz. In zGaAs, the most notable pressure-induced softening occurs for transverse acoustic modes at X and L, near and just below 2 THz. From results discussed in the main text, we know that pressure will cause the phonon frequencies of these modes to decrease until they become imaginary at the onset of instability.

4.6.4 Anharmonic Calculations of Phonon Decay Channels

The momenta and frequencies of decay channels depicted in Fig. 4.10 are summarized in Table 4.1. Because several decay channels are depicted for each source mode and destination modes are consequently shown to have ranges, the frequencies and coordinates listed in Table 4.1 correspond to an average of those ranges.

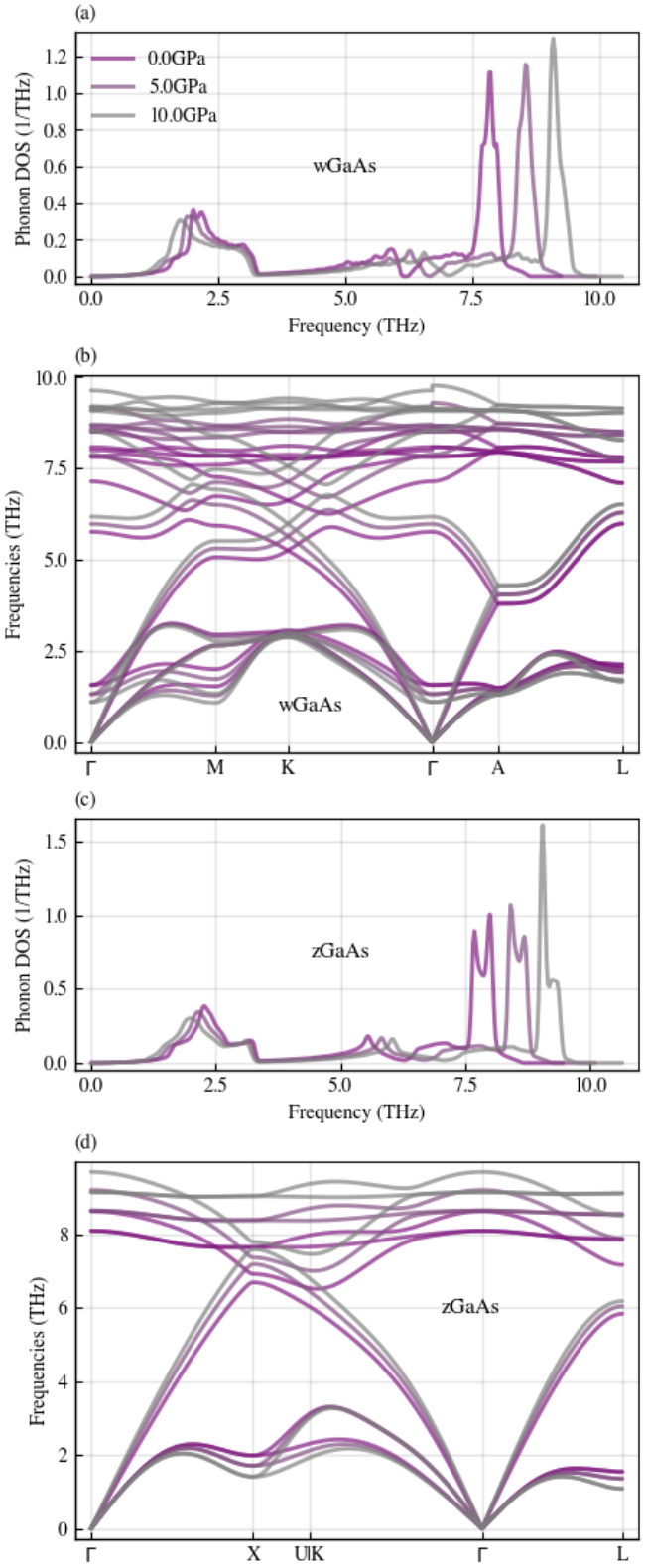

Figure 4.13: Phonon DOS and dispersion relations at 0 K for three pressures for wGaAs ((a) and (b)) and zGaAs ((c) and (d)). Panels (c) and (d) show that the pressure-induced softening of the lower energy portions of the spectra from the transverse acoustic modes and, in (c), of one set of transverse optical modes. The most apparent softening occurs at the M and Γ points in wGaAs and at X and L in zGaAs.

		q-coordinates			**frequencies (THz)**		
material	*pressure*	*source*	*dest 1*	*dest 2*	*source*	*dest 1*	*dest 2*
wGaAs	0 GPa	0.436667 * [1, -0.5, 0]	0.111667 * [1, -0.5, 0]	0.325 * [1, -0.5, 0], 5.4 THz	6.1	0.7	5.4
	10 GPa	0.436667 * [1, -0.5, 0]	0.176667 * [1, -0.5, 0]	0.26 * [1, -0.5, 0]	6.9	1.0	5.9
	0 GPa	0.449749 * [1, 0, 0]	0.0728643 * [1, 0, 0]	0.376884 * [1, 0, 0]	6.3	0.5	5.8
	10 GPa	0.449749 * [1, 0, 0]	0.175879 * [1, 0, 0]	0.273869 * [1, 0, 0]	7.1	5.8	1.3
zGaAs	0 GPa	0.74625 * [0.5, 0.5, 1]	0.3375 * [0.5, 0.5, 1]	0.40875 * [0.5, 0.5, 1]	5.7	1.6	4.1
	10 GPa	0.74625 * [0.5, 0.5, 1]	0.136875 * [0.5, 0.5, 1]	0.609375 * [0.5, 0.5, 1]	6.6	0.7	5.9
	0 GPa	0.43 * [1, 1, 1]	0.04 * [1, 1, 1]	0.39 * [1, 1, 1]	5.3	0.3	5.0
	10 GPa	0.43 * [1, 1, 1]	0.0375 * [1, 1, 1]	0.3925 * [1, 1, 1]	5.8	0.3	5.6

Table 4.1: This table summarizes the decay channels depicted in Fig. 4.10. For each material and pressure, "destination" modes sum to "source" modes, conserving both energy (via additive frequencies) and crystal momenta (via additive q-coordinates).

4.6.5 Negative Grüneisen parameters

Phonon modes that stiffen with increasing pressure, and thereby decreasing volume, have positive Grüneisen parameters; those that soften under the same conditions have negative Grüneisen parameters. Figure 4.5 shows that most phonons in wGaAs and zGaAs stiffen with increasing pressure, indicating positive Grüneisen mode parameters, and that transverse acoustic phonon branches along certain high symmetry directions have negative Grüneisen parameters. In most materials, the stiffening of phonon modes with decreasing volume is typical, and drives thermal expansion. After all, as temperature increases, it alters the free energy landscape of the material; if the equilibrium volume that minimized the free energy at T no longer minimizes the free energy at $T + \delta T$, the material changes its volume to increase entropy.

For a set of N 3D classical harmonic oscillators, the vibrational entropy, S_{vib}, can be expressed cleanly as

$$S_{vib} = -\frac{\partial F_{vib}}{\partial T} = -k_B \ln\left(\prod_{i=1}^{3N} \frac{\hbar\omega_i}{k_B T}\right) . \tag{4.15}$$

Because for $y = -\ln(x)$, y increases as x decreases, the vibrational entropy increases (and free energy decreases) when changes in volume reduce the phonon frequencies, $\{\omega_i\}$. If a phonon mode stiffens with increasing pressure, shifting to lower frequencies with increasing volume, it will help to drive (positive) thermal expansion. On the other hand, decreasing volume with increasing temperature lowers the vibrational energy contribution to the free energy of phonon modes with negative Grüneisen parameters. For this reason, negative Grüneisen parameters are often associated with negative thermal expansion (NTE), though NTE occurs only when the contributions to the free energy from those modes with negative Grüneisen parameters dominate the modes with positive Grüneisen parameters. Pressure-induced softening of transverse acoustic modes in GaAs is consistent with findings that zGaAs exhibits negative thermal expansion up to about 60 K.[65]. However, there may be a role for anharmonicity and the zero point atom displacements at low temperature, as was recently shown for silicon[58].

4.6.6 Comparison with $P - T$ coupling effects in gallium nitride

Figure 4.7 of the main text shows that in both wGaAs and zGaAs, the QHA less accurately accounts for thermal frequency shifts at high pressures. In GaAs, pressure seems to enhance the importance of explicitly anharmonic phonon effects in accounting for temperature-driven phonon behavior. Figure 4.14 is an analog to Fig.

4.7 of the main text, using GaN phonon data from our previous work[59]. In GaN, the effect of pressure on the reliability of the QHA is less important than in GaAs. Panel (b) shows that pressure slightly augments phonon stiffening around 20 THz caused by explicit temperature-driven anharmonicity in wGaN; on the other hand, effects of pressure on temperature-driven anharmonicity in zGaN are hard to detect with panels (c) and (d). Our use of more extreme pressures in GaN than in GaAs makes it more likely that we would observe the $P-T$ coupling effects in GaN than in GaAs.

Instead of comparing $P-T$ coupling results in GaAs at 1200 K to GaN at 1120 K, it may be better to compare at temperatures scaled by their Debye temperatures. The Debye temperature of GaN ($\approx$ 600 K) is about 1.67 times that of GaAs ($\approx$ 360 K). Temperature effects in GaAs by 600 K may be a better comparison to those in GaN by 1120 K. In Fig. 4.15, we see that even at 600 K, the impact of pressure on temperature-driven anharmonicity in GaAs is clear, and much more evident than in Fig. 4.14. Although we observed other pressure-temperature coupling effects in both wGaN and zGaN[59], pressure-temperature coupling in wGaAs and zGaAs seems more pronounced.

4.6.7 Estimating phonon instability onset from γ

The i^{th} mode Grüneisen parameter is defined as

$$\gamma_i = \frac{-V}{\omega_i}\frac{\partial \omega_i}{\partial V} \approx \frac{-V}{\omega_i}\frac{\Delta \omega_i}{\Delta V} \ . \tag{4.16}$$

We can use this equation to estimate the volume at which phonon instability occurs by calculating the volume change associated with a phonon frequency shift to 0 THz.

Assume that pressure "H" is the highest pressure for which we have stable data and that pressure "I" is the pressure at which the first phonon mode to become unstable softens to 0 THz. Call that first phonon "X" (as in the case of zGaAs). Its Grüneisen parameter is

$$\gamma_{X,H} \approx \frac{-V_H}{\omega_{X,H}}\frac{\omega_{X,I}-\omega_{X,H}}{V_I - V_H} \ . \tag{4.17}$$

Here, $\omega_{X,I}$ is 0 THz, the frequency at which the X mode first becomes unstable, and V_I is the associated volume. Similarly, $\omega_{X,H}$, V_H, and $\gamma_{X,H}$ are the frequency, volume, and grünesien parameter at X of the phonon branch to go unstable at the highest pressure for which we have data. Equation 4.16 becomes

$$\gamma_{X,H} \approx \frac{-V_H}{\omega_{X,H}}\frac{-\omega_{X,H}}{V_I - V_H} \approx \frac{V_H}{V_I - V_H} \ . \tag{4.18}$$

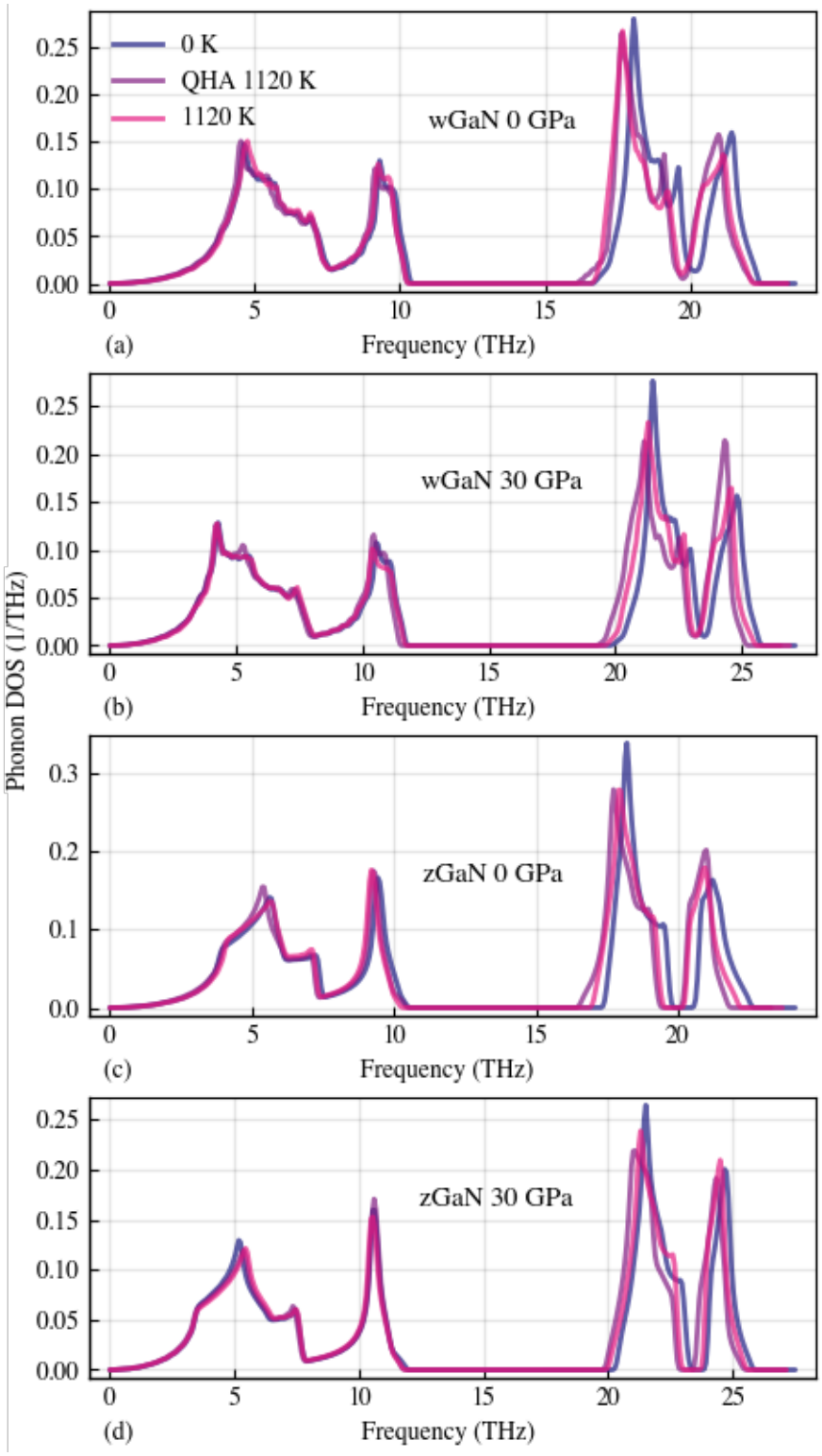

Figure 4.14: Overlays of phonon DOS at 0 K and at 1120 K per a QHA and with full anharmonic phonon effects are shown at (a) 0.0 GPa in wGaN, (b) 30.0 GPa in wGaN, (c) 0.0 GPa in zGaN, and (d) 30.0 GPa in zGaN.

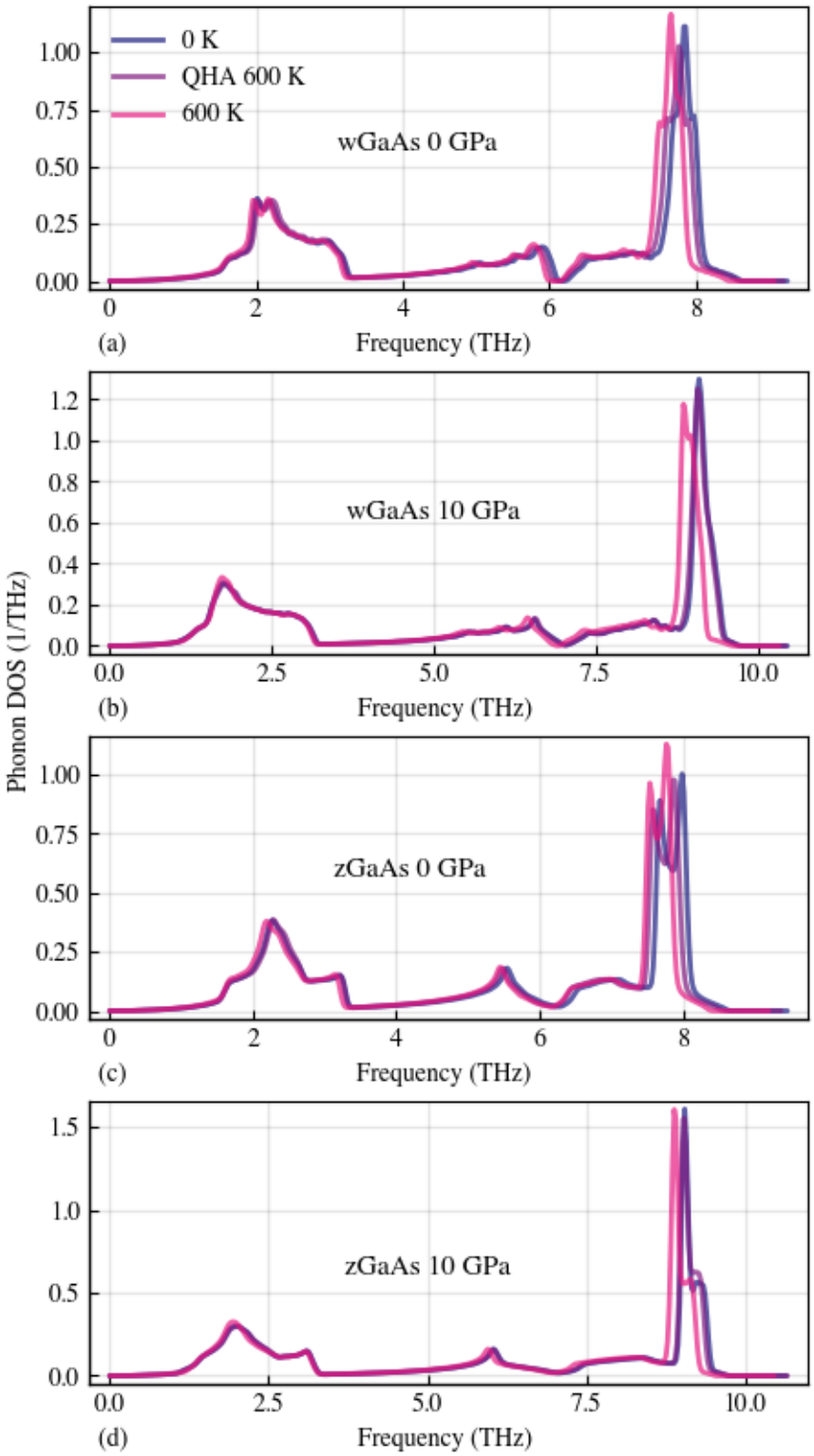

Figure 4.15: Overlays of phonon DOS at 0 K and at 600 K per a QHA and with full anharmonic phonon effects are shown at (a) 0.0 GPa in wGaAs, (b) 10.0 GPa in wGaAs, (c) 0.0 GPa in zGaAs, and (d) 10.0 GPa in zGaAs.

The volume of the onset of lattice instability is V_I

$$V_I \approx \frac{V_H}{\gamma_{X,H}} + V_H \ . \tag{4.19}$$

With V_I, the associated pressure, P_I is found by fitting to a Birch-Murnaghan equation of state.

The two largest sources of error in using this approximation come from extrapolation of pressure-volume relations, and the inequality of $\gamma_{X,H}$ and $\gamma_{X,I}$. When we use $\gamma_{X,H}$ to approximate the volume change until instability, we assume that the Grüneisen parameter at X will not change with volume, though we know that it does. Our estimates for V_I should place lower bounds on V_I (upper bounds on P_I). We used phonon data to estimate the pressures of instability onset. These estimates are approximate. Pressure-volume relationships come from a Birch-Murnaghan equation of state fitted to the sum of the 0 K static total energy and the phonon free energies versus volume, and depends on accurate phonon free energies. Once the phonon dispersion relations show a clear instability, the corresponding phonon free energies cannot reliably be used to determine the pressure at that volume; this means that we can calculate the pressures for volumes smaller than those for which we have obtained stable phonon data only by extrapolation. Extrapolating the free energy surface of each material to slightly smaller volumes than those for which we have stable phonon dispersion relations does allow a general understanding of material behavior.

Chapter 5

SUMMARY & FUTURE DIRECTIONS

5.1 Summary

5.1.1 Approach

In this work, I used computational tools to investigate how phonon thermodynamic and elastic properties of Gallium Nitride (GaN) and Gallium Arsenide (GaAs), in both the wurtzite and zinc blende structures, evolve with pressure and temperature.

VASP, an implementation of density functional theory (DFT), and TDEP, a method and its software implementation for studying temperature-dependent lattice dynamics, are the primary computational tools I used. DFT allowed me to perform ab-initio ground state electronic structure calculations on individual configurations of atoms that could be thought of as snapshots of a material's atoms for a given point in that material's temperature-pressure phase space. Interatomic forces are one of the outputs of a DFT calculation and one of the inputs to TDEP. By modeling the interatomic bonds as interatomic springs that connect neighboring billiard ball-like atoms, TDEP uses these forces, as well as the temperature and pressure-dependent atomic configurations for which they are generated, to determine the force constants describing the interatomic springs. With TDEP's lattice dynamical formalism, these force constants can then be used to determine a host of thermodynamic properties. The combination of DFT and TDEP allowed us to determine how pressure and temperature impact the elastic constants and phonon spectra of GaN and GaAs without any experimental inputs.

Comparing the temperature and pressure responses of GaN and GaAs in the wurtzite and zinc blende structures — their equilibrium and lowest energy metastable phases at ambient conditions — allowed us to identify relationships between the effects observed and either the chemical composition or the crystal structure of the material.

5.1.2 Findings

This work highlights failures of the Born stability criteria to predict the onset of pressure-induced lattice instability and of the quasiharmonic approximation (QHA) to predict the evolution of phonon spectra with either elevated temperature or jointly elevated temperature and pressure.

The Born stability criteria assume that lattice stability can be determined from knowledge of a material's elastic constants, which are related to the near-Γ acoustic branches of the phonon dispersion relations, and that knowledge of shorter wavelength phonon behavior is unnecessary. In both wurtzite and zinc blende GaAs, increasing pressure caused shorter wavelength phonon instabilities that preceded the onset of lattice instability per the Born stability criteria at 0 K. On the other hand, the Born stability criteria predicted elastic instabilities in wurtzite and zinc blende GaN prior to the onset of shorter wavelength phonon instabilities.

The QHA assumes that the effects of changing temperature can be reduced to the effects of associated temperature-induced volume changes. We observed explicitly anharmonic effects — temperature-driven effects not predicted by a QHA — in both phases of GaAs and GaN investigated. In addition to finding anharmonic phonon frequency shifts and phonon linewidth broadening caused by temperature in all materials, we also found that the impact of temperature and pressure on these properties were not additive. The degree of temperature-driven anharmonicity exhibited by each material depended upon the pressure considered. QHAs do not account for this pressure-temperature coupling.

Next, it is interesting to consider how the usefulness of the Born stability criteria and QHA varied for each of the four materials — wGaAs, zGaAs, wGaN, and zGaN — considered.

Dissimilar atomic masses for Ga (69.7 amu/atom) and N (14.0 amu/atom) creates a phonon bandgap in GaN, whereas more similar atomic masses for Ga and As (74.9 amu/atom) prevent GaAs from exhibiting a true phonon bandgap. Resulting proximity between optical and acoustic modes in GaAs creates accessible down-conversion processes and drove anharmonic effects across all pressures investigated (up to 15 GPa and 1200 K); increasing pressure increased the degree of material anharmonicity observed. In GaN, on the other hand, the phonon bandgap increased with increasing pressure; the increased energetic distance between optical and acoustic modes decreased the availability of down-conversion processes and GaN became more quasiharmonic with increasing pressure.

The Grüneisen parameters of the transverse acoustic modes for all four materials considered were negative, whereas Grüneisen parameters for all other phonon modes were positive. (This is typical of both the wurtzite and zinc blende crystal structures.) This characteristic drove increasing elastic anisotropy with pressure and greater pressure-temperature coupling of anharmonic effects exhibited. First, because of

the relationship between near-Γ acoustic modes and the elastic constants, large differences in the Grüneisen parameters of acoustic modes (such as negative γ_i for transverse modes and positive γ_i for the longitudinal mode) cause the elastic anisotropy of a material to increase with increasing pressure, as different elastic constants are pulled in different directions. Second, anharmonic temperature effects would be independent of pressure if pressure did not impact the availability of phonon decay channels by shifting the frequencies of phonon branches by varying degrees. Pressure can both create and eliminate down-conversion processes when the Grüneisen parameters for higher frequency (mostly optical) phonon modes and the lower frequency (acoustic and some optical) modes into which they decay are dissimilar.

The temperature (between 0 and 1120 K) of GaN, for which we used the Born stability criteria to determine lattice stability at 0 K, did not greatly impact the frequencies of its long wavelength acoustic phonons. Therefore we do not expect either the elastic constants or the lattice stability to change much with temperature. Conversely, temperature slows the pressure-induced softening of transverse acoustic modes that leads to lattice instability in GaAs. Though our data is not precise enough to know if this softening slows enough to make the Born stability criteria relevant at temperatures below melting, we can see that temperature partially stabilizes the onset of lattice stability by increasing the pressure through which wGaAs and zGaAs are stable at increasing temperatures.

5.2 Future directions

5.2.1 Further investigations of pressure-temperature coupling

The wurtzite and zinc blende crystal structures are known for the negative Grüneisen parameters of their transverse acoustic modes. Given positive Grüneisen parameters for all other modes, this characteristic results in very dissimilar Grüneisen parameters and drives the pressure dependence of anharmonic temperature effects. It would be interesting to study the extent to which pressure-temperature coupling of phonon properties occurs in other crystal systems, especially those with more consistent mode Grüneisen parameter. Heuristics such as groups of crystal systems identified as more or less likely to exhibit pressure-temperature coupling would help illuminate the degree of brute force likely needed to traverse the temperature-pressure phase space of materials. For example, additivity of pressure and temperature effects will be a less reasonable assumption in some materials than others; greater understanding of these trends will help scientists to better evaluate trade-offs when considering

their resources and the degree of accuracy required in their research.

5.2.2 Extending simulation timescales for Ehrenfest dynamics to include phonons

As our computational power increases, so does our ability to move beyond approximations that often fail. For example, Born Oppenheimer molecular dynamics (BOMD) often better accounts for the effect of temperature on phonons than do analytic models that add anharmonic corrections to quasiharmonic approximations. Today BOMD or even sTDEP, which is less computationally intensive than BOMD, is much more easily accomplished than several years ago. One limitation of methods based on DFT outputs, such as BOMD and sTDEP, is that they always allow electrons to equilibrate. Time-dependent density functional theory (TDDFT), on the other hand, allows electrons to leave the ground state, permitting investigations of excited-state electron properties in materials interacting with, for example, laser pulses or fast particles. Just as BOMD is built upon DFT, *Ehrenfest dynamics* is built upon TDDFT, capturing non-equilibrium electron behavior in a system with moving atomic nuclei. Studying the temperature and pressure evolution of anharmonic phonon behavior with Ehrenfest dynamics would allow us to probe the effects of potential electron-phonon coupling. For example, Ehrenfest dynamics could account for the impact of radiation damage caused by quickly moving ions on thermodynamic properties; studies of the impact of radiation damage on heat transfer in GaAs would be particularly relevant to space mission technology. Unfortunately, the use of Ehrenfest dynamics for phonon calculations is currently computationally intractable. The Born-Oppenheimer approximation is effective because of widely different timescales for electronic and atomic "movements". Time steps in BOMD (order of 10^{-15} seconds) are usually about 100 times longer than Ehrenfest time steps (10^{-17} or 10^{-18} seconds). If each time step in an Ehrenfest dynamics simulation were as time intensive as those in BOMD, Ehrenfest dynamics would take 100 times as long, making it prohibitive for phonon calculations. (Things are not really quite this bad because wavefunctions do not need to be re-orthogonalized at each step in Ehrenfest dynamics.) As the power of our computational resources expand and the world's fastest machines approach exascale capabilities (with Argonne National Lab planning to launch Aurora, the first exascale machine next year in 2021), research problems like those pursued herein may one day be tractable with either Ehrenfest dynamics or similarly high-fidelity methods for simulating excited state electrons.

Appendix A

ELASTIC CONSTANTS

In this section, I review the origin of the elastic constants and a method for calculating them. Elastic constants are traditionally calculated either by energy-strain or stress-strain methods. Here I review an energy-strain method.

Let's assume a coordinate system defined by three mutually orthogonal vectors $\vec{x}$, $\vec{y}$, and $\vec{z}$, each of length 1. If we imagine this coordinate system embedded within a solid, applying a strain to that solid will strain the coordinate system, resulting in new axes $\vec{x'}$, $\vec{y'}$, and $\vec{z'}$. We can tie these new axes to their predecessors as follows:

$$\vec{x'} = (1 + e_{xx})\vec{x} + e_{xy}\vec{y} + e_{xz}\vec{z}$$

$$\vec{y'} = e_{yx}\vec{x} + (1 + e_{yy})\vec{y} + e_{yz}\vec{z}$$

$$\vec{z'} = e_{zx}\vec{x} + e_{zy}\vec{y} + (1 + e_{zz})\vec{z}$$

A strain applied to a solid is typically defined in terms of quantities ϵ_{ij} (elements of the strain tensor, $\bar{\epsilon}$) rather than e_{ij}, where ϵ_{ij} are defined as

$$\epsilon_{xx} = e_{xx}$$

$$\epsilon_{yy} = e_{yy}$$

$$\epsilon_{zz} = e_{zz}$$

$$\epsilon_{xy} = \vec{x'} \cdot \vec{y'} e_{yx} + e_{xy}$$

$$\epsilon_{yz} = \vec{y'} \cdot \vec{z'} e_{zy} + e_{yz}$$

$$\epsilon_{zx} = \vec{z'} \cdot \vec{x'} e_{zx} + e_{xz}$$

Once we have all ϵ_{ij} allowing us to quantify the strain, Taylor expanding the energy of the crystal under strain, $E(\bar{\epsilon})$, gives us

$$E(\bar{\epsilon}) = E(0) + \sum_{i,j} \frac{\partial E}{\partial \epsilon_{ij}} \,|_0\, \epsilon_{ij} + \frac{1}{2} \sum_{i,j,k,l} \frac{\partial^2 E}{\partial \epsilon_{ij} \partial \epsilon_{kl}} \epsilon_{ij} \epsilon_{kl} \tag{A.1}$$

where $\sum_{i,j}$ means we should sequentially set each of i and j equal to x, y, and z, while accumulating the result. The above can also be written as

$$E(\bar{\epsilon}) = E(0) + V \sum_{i,j} \sigma_i \mid_0 \epsilon_{ij} + \frac{V}{2} \sum_{i,j,k,l} C_{ijkl} \epsilon_{ij} \epsilon_{kl} \tag{A.2}$$

where our elastic constants have now entered as the elements $C_{ijkl} = \frac{1}{V} \frac{\partial^2 E}{\partial \epsilon_{ij} \partial \epsilon_{kl}}$ of the rank-four tensor $\bar{C}$. Also note that σ is the stress tensor, and V the volume.

Luckily, some symmetries and natural redundancies allow our rank-four tensor $\bar{C}$ to be reduced to a 6×6 matrix. This is done using Voigt notation, where

$xx \rightarrow 1$

$yy \rightarrow 2$

$zz \rightarrow 3$

$xy \rightarrow 4$

$yz \rightarrow 5$

$xz \rightarrow 6$

In Voigt notation, the energy of a crystal under strain, $E(\epsilon)$, may be Taylor expanded as

$$E(\bar{\epsilon}) = E(0) + \sum_{i=1}^{6} \frac{\partial E}{\partial \epsilon_i} \mid_0 \epsilon_i + \frac{1}{2} \sum_{i,j=1}^{6} \frac{\partial^2 E}{\partial \epsilon_i \partial \epsilon_j} \epsilon_i \epsilon_j \tag{A.3}$$

or equivalently as

$$E(\bar{\epsilon}) = E(0) + V \sum_{i=1}^{6} \sigma_i \mid_0 \epsilon_i + \frac{V}{2} \sum_{i,j=1}^{6} C_{ij} \epsilon_i \epsilon_j \tag{A.4}$$

Ignoring the stress, $\sigma_k = 0$, this reduces to

$$\frac{\Delta E}{V} = \frac{E(\bar{\epsilon}) - E(0)}{V} = \frac{1}{2} \sum_{i,j=1}^{6} C_{ij} \epsilon_i \epsilon_j \tag{A.5}$$

To determine the values of C_{ij}, we could determine how the energy changes in response to straining the lattice vectors of a crystal unit cell.

The general form of the strain tensor that we use is

$$\bar{\epsilon} = \begin{bmatrix} \epsilon_1 & \frac{1}{2}\epsilon_6 & \frac{1}{2}\epsilon_5 \\ \frac{1}{2}\epsilon_6 & \epsilon_2 & \frac{1}{2}\epsilon_4 \\ \frac{1}{2}\epsilon_5 & \frac{1}{2}\epsilon_4 & \epsilon_3 \end{bmatrix} \tag{A.6}$$

and we will consider strains from the work of Beckstein[66]. For a tetragonal structure, we could use the following strains to calculate C_{ij}:

$$\bar{\epsilon}_1(\delta) = \delta \begin{bmatrix} 2 & 0 & 0 \\ 0 & -1 & 0 \\ 0 & 0 & -1 \end{bmatrix} \tag{A.7}$$

$$\bar{\epsilon}_2(\delta) = \delta \begin{bmatrix} -1 & 0 & 0 \\ 0 & -1 & 0 \\ 0 & 0 & 2 \end{bmatrix} \tag{A.8}$$

$$\bar{\epsilon}_3(\delta) = \delta \begin{bmatrix} 1 & 1 & 0 \\ 1 & 1 & 0 \\ 0 & 0 & -2 \end{bmatrix} \tag{A.9}$$

$$\bar{\epsilon}_4(\delta) = \delta \begin{bmatrix} 1 & 0 & 0 \\ 0 & 0 & 0 \\ 0 & 0 & 0 \end{bmatrix} \tag{A.10}$$

$$\bar{\epsilon}_5(\delta) = \delta \begin{bmatrix} 0 & 0 & 0 \\ 0 & 0 & 0 \\ 0 & 0 & 1 \end{bmatrix} \tag{A.11}$$

$$\bar{\epsilon}_6(\delta) = \delta \begin{bmatrix} 0 & 0 & 0 \\ 0 & 0 & 1 \\ 0 & 1 & 0 \end{bmatrix} \tag{A.12}$$

Note that these strains could be used for the wurtzite structure, as the wurtzite lattice is a type of hexagonal lattice and hexagonal lattices are a special case of tetragonal lattices.

For a cubic structure, we could use the following strains:

$$\bar{\epsilon}_7(\delta) = \begin{bmatrix} \delta & 0 & 0 \\ 0 & \delta & 0 \\ 0 & 0 & \frac{1}{(1+\delta)^2} - 1 \end{bmatrix} \tag{A.13}$$

$$\bar{\epsilon}_8(\delta) = \delta \begin{bmatrix} 1 & 0 & 0 \\ 0 & 1 & 0 \\ 0 & 0 & 1 \end{bmatrix} \tag{A.14}$$

$$\bar{\epsilon}_9(\delta) = \begin{bmatrix} 0 & \frac{\delta}{2} & 0 \\ \frac{\delta}{2} & 0 & \frac{\delta^2}{4-\delta^2} \\ 0 & 0 & 0 \end{bmatrix} \tag{A.15}$$

Each of the strain tensors,$\bar{\epsilon}_k$, given is parameterized by some variable δ. For a given δ, we can strain the lattice vectors of a unit cell $\{\vec{b}_i\}$, to generate $\{\vec{b}_i^k\}$

$$\vec{b}_i^k = (\bar{I} + \bar{\epsilon}_k) \cdot \vec{b}_i = \vec{b}_i + \bar{\epsilon}_k \cdot \vec{b}_i \tag{A.16}$$

In practice, each of the strain tensors $\bar{\epsilon}_k$ would be applied to the lattice vectors for each of several values of δ, and ab initio simulation software could be used to calculate the energies of each of the resulting strained unit cells. We could then fit the resulting energies, $E_{strain-k}$ to a quadratic function of the values of δ used

$$\frac{E_{strain-k}}{V} = a_k\delta^2 + \frac{E_{min}}{V} = a_k\delta^2 + c \tag{A.17}$$

generating coefficient a_k for each strain tensor. Following this process would generate six coefficients a_k, $\{ a_1, ...a_6\}$ for a tetragonal crystal and three coefficients a_k, $\{a_7, a_8, a_9\}$, for a cubic crystal.

A system of equations in which coefficients $\{a_k\}$ equate to linear combinations of the elastic constants would allow us to solve for the elastic constants in each crystal structure:

For cubic

$$a_1 = 3 * (C_{11} - C_{12}) \tag{A.18}$$

$$a_2 = 3/2 * (C_{11} + 2 * C_{12}) \tag{A.19}$$

$$a_3 = 1/2 * C_{44} \tag{A.20}$$

For tetragonal (with hexagonal as a subset)

$$a_1 = 1/2 * (5 * C_{11} - 4C_{12} - 2C_{13} + C_{33}) \tag{A.21}$$

$$a_2 = C_{11} + C_{12} - 4C_{13} + 2C_{33} \tag{A.22}$$

$$a_3 = C_{11} + C_{12} - 4C_{13} + 2C_{33} + 2C_{66} \tag{A.23}$$

$$a_4 = 1/2C_{11} \tag{A.24}$$

$$a_5 = 1/2C_{33} \tag{A.25}$$

$$a_6 = 2C_{44} \tag{A.26}$$

We can formulate these linear systems of equations in terms of matrix-vector multiplies as

For cubic

$$\begin{bmatrix} a_1 \\ a_2 \\ a_3 \end{bmatrix} = \begin{bmatrix} 3 & -3 & 0 \\ 3/2 & 3 & 0 \\ 0 & 0 & 1/2 \end{bmatrix} * \begin{bmatrix} C_{11} \\ C_{12} \\ C_{44} \end{bmatrix} \tag{A.27}$$

For tetragonal

$$\begin{bmatrix} a_1 \\ a_2 \\ a_3 \\ a_4 \\ a_5 \\ a_6 \end{bmatrix} = \begin{bmatrix} 5/2 & -2 & -1 & 1/2 & 0 & 0 \\ 1 & 1 & -4 & 2 & 0 & 0 \\ 1 & 1 & -4 & 2 & 0 & 2 \\ 1/2 & 0 & 0 & 0 & 0 & 0 \\ 0 & 0 & 0 & 1/2 & 0 & 0 \\ 0 & 0 & 0 & 0 & 2 & 0 \end{bmatrix} * \begin{bmatrix} C_{11} \\ C_{12} \\ C_{13} \\ C_{33} \\ C_{44} \\ C_{66} \end{bmatrix} \tag{A.28}$$

At a higher level, we might rewrite either of these linear systems of equations as

$\vec{a} = \mathbf{M} * \vec{c}$

where $\vec{a}$ is a vector holding the quadratic coefficients from fitting above, $\mathbf{M}$ is a matrix holding the coefficients as shown above, and $\vec{c}$ holds the non-zero elastic constants in a vector.

We could then solve for the elastic constants

$\vec{c} = \mathbf{M} \backslash \vec{a}$

BIBLIOGRAPHY

1. Fultz, B. Vibrational thermodynamics of materials. *Progress in Materials Science* **55,** 247–352. ISSN: 0079-6425 (2010).
2. Mauger, L. *et al.* Phonons and elasticity of cementite through the Curie temperature. *Physical Review B* **95,** 1–9 (2017).
3. Kittel, C. *Introduction to Solid State Physics, 8th edition* (John Wiley Sons, Inc., 2004).
4. Kresse, G. & Furthmüller, J. Efficient iterative schemes for ab initio total-energy calculations using a plane-wave basis set. *Physical Review B* **54,** 11169–11186 (1996).
5. Kresse, G. & Furthmüller, J. Efficiency of ab initio total energy calculations for metals and semiconductors using a plane-wave basis set. *Computational Materials Science* **6,** 15–50 (1996).
6. Gonze, X. *et al.* Recent developments in the ABINIT software package. *Computer Physics Communications* **205,** 106 (2016).
7. Plimpton, S. Fast Parallel Algorithms for Short-Range Molecular Dynamics. *Journal of Computational Physics* **117,** 1–19 (1995).
8. Wilson, M. & Madden, P. A. Transformations between tetrahedrally and octahedrally coordinated crystals: the wurtzite to rocksalt and blende to rocksalt mechanisms. *Journal of Physics: Condensed Matter* **14,** 4629 (2002).
9. Lei, T. *et al.* Epitaxial growth of zinc blende and wurtzitic gallium nitride thin films on (001) silicon. *Applied Physics Letters* **59,** 944–946 (1991).
10. Serrano, J., Rubio, A., Hernández, E., Muñoz, A. & Mujica, A. Theoretical study of the relative stability of structural phases in group-III nitrides at high pressures. *Physical Review B* **62,** 16612–16623 (2000).
11. Xia, H., Xia, Q. & Ruoff, A. L. High-pressure structure of gallium nitride: Wurtzite-to-rocksalt phase transition. *Physical Review B* **47,** 12925–12928 (19 May 1993).
12. Mujica, A., Rubio, A., Muñoz, A. & Needs, R. J. High-pressure phases of group-IV, III-V, and II-VI compounds. *Reviews of Modern Physics* **75,** 863–912 (2003).
13. Knudson, M. D., Gupta, Y. M. & Kunz, A. B. Transformation mechanism for the pressure-induced phase transition in shocked CdS. *Physical Review B* **59,** 11704–11715 (18 May 1999).
14. Zaoui, A. & Sekkal, W. Pressure-induced softening of shear modes in wurtzite ZnO: A theoretical study. *Physical Review B* **66,** 1–6 (2002).

15. Saitta, A. M. & Decremps, F. Unifying description of the wurtzite-to-rocksalt phase transition in wide-gap semiconductors: The effect of d electrons on the elastic constants. *Physical Review B* **70,** 1–5 (2004).

16. Li, C. W. *et al.* Structural relationship between negative thermal expansion and quartic anharmonicity of cubic ScF3. *Physical Review Letters* **107,** 1–5 (2011).

17. Shulumba, N. *et al.* Impact of anharmonic effects on the phase stability, thermal transport, and electronic properties of AlN. *Physical Review B* **94,** 1–8 (2016).

18. Kohn, W. & Sham, L. J. Self-Consistent Equations Including Exchange and Correlation Effects. *Physical Review* **140** (1965).

19. Blöchl, P. E. Projector augmented-wave method. *Physical Review B* **50,** 17953 (1994).

20. Monkhorst, H. & Pack, J. Special points for Brillouin-zone integrations. *Physical Review B* **13,** 5188–5192 (June 1976).

21. Hellman, O., Abrikosov, I. A. & Simak, S. I. Lattice dynamics of anharmonic solids from first principles. *Physical Review B - Condensed Matter and Materials Physics* **84,** 1–5 (2011).

22. Hellman, O. & Abrikosov, I. A. Temperature-dependent effective third-order interatomic force constants from first principles. *Physical Review B* **88,** 144301 (Oct. 2013).

23. Hellman, O., Steneteg, P., Abrikosov, I. A. & Simak, S. I. Temperature dependent effective potential method for accurate free energy calculations of solids. *Physical Review B* **87,** 104111 (2013).

24. Shulumba, N., Hellman, O. & Minnich, A. J. Intrinsic localized mode and low thermal conductivity of PbSe. *Physical Review B* **95,** 1–9 (2017).

25. Klein, M. L. & Horton, G. K. The rise of self-consistent phonon theory. *Journal of Low Temperature Physics* **9,** 151–166 (Nov. 1972).

26. Hooton, D. J. A new treatment of anharmonicity in lattice thermodynamics. *The London, Edinburgh, and Dublin Philosophical Magazine and Journal of Science* **46,** 422–432 (1955).

27. Gonze, X., Charlier, J.-C., Allan, D. & Teter, M. Interatomic force constants from first principles: The case of α-quartz. *Physical Review B* **50,** 13035–13038 (17 Nov. 1994).

28. Gonze, X. & Lee, C. Dynamical matrices, Born effective charges, dielectric permittivity tensors, and interatomic force constants from density-functional perturbation theory. *Physical Review B* **55,** 10355–10368 (16 Apr. 1997).

29. Biernacki, S. & Scheffler, M. Negative thermal expansion of diamond and zinc-blende semiconductors. *Physical Review Letters* **63,** 290–293 (3 July 1989).

30. Barrera, G. D., Bruno, J. A. O., Barron, T. H. K. & Allan, N. L. Negative thermal expansion. *Journal of Physics: Condensed Matter* **17,** 217–252 (2005).

31. Wang, L. *et al.* First-principles investigation of negative thermal expansion in II-VI semiconductors. *Materials Chemistry and Physics* **148,** 214–222 (2014).

32. Ranganathan, S. I. & Ostoja-Starzewski, M. Universal elastic anisotropy index. *Physical Review Letters* **101,** 3–6 (2008).

33. Hill, R. The Elastic Behaviour of a Crystalline Aggregate. *Proceedings of the Physical Society. Section A* **65,** 349 (1952).

34. Wang, J., Yip, S., Phillpot, S. & Wolf, D. Crystal Instabilities at Finite Strain. *Physical Review Letters* **71,** 4182–4185 (1993).

35. Wang, J., Li, J., Yip, S., Phillpot, S. & Wolf, D. Mechanical instabilities of homogenous crystals. *Physical Review B* **52,** 12 627 –12 635 (1995).

36. Karki, B. B., Ackland, G. J. & Crain, J. Elastic instabilities in crystals from ab initio stress - strain relations. *Journal of Physics: Condensed Matter* **9,** 8579–8589 (1997).

37. Sin'ko, G. V. & Smirnov, N. A. Ab initio calculations of elastic constants and thermodynamic properties of bcc, fcc, and hcp Al crystals under pressure. *Journal of Physics: Condensed Matter* **14,** 6989–7005 (2002).

38. Wallace, D. C. *Thermodynamics of Crystals* (Dover Publications, 1972).

39. Maradudin, A. A. & Fein, A. E. Scattering of Neutrons by an Anharmonic Crystal. *Physical Review* **128,** 2589–2608 (6 Dec. 1962).

40. Mouhat, F. & Coudert, F. X. Necessary and sufficient elastic stability conditions in various crystal systems. *Physical Review B* **90,** 4–7 (2014).

41. Momma, K. & Izumi, F. VESTA3 for three-dimensional visualization of crystal, volumetric and morphology data. *Journal of Applied Crystallography* **44,** 1272–1276 (Dec. 2011).

42. Zolper, J. A review of junction field effect transistors for high-temperature and high-power electronics. *Solid-State Electronics* **42,** 2153–2156. ISSN: 0038-1101 (1998).

43. Ajayan, J. *et al.* GaAs metamorphic high electron mobility transistors for future deep space-biomedical-millitary and communication system applications: A review. *Microelectronics Journal* **92,** 104604. ISSN: 0026-2692 (2019).

44. Shur, M. in. Chap. Metal Semiconductor Field Effect Transistors (CRC Press, 2007).

45. Cook, G., Billman, L. & Adcock, R. *Photovoltaic Fundamentals* (National Technical Information Service, 1995).

46. Del Papa, C., Pelfer, P. G. & Smith, K. *GaAs Detectors and Electronics for High Energy Physics* (World Scientific, 1993).

47. Cripps, S. *RF Power Amplifiers for Wireless Communications, Second Edition* (Artech House, 2006).

48. Dupont, E., Liu, H. C. & Buchanan, M. *Applied Physics Letters* **76,** 4–6 (2000).

49. Hall, R. N., Fenner, G. E., Kingsley, J. D., Soltys, T. J. & Carlson, R. O. Coherent Light Emission From GaAs Junctions. *Physical Review Letters* **9,** 366–368 (9 Nov. 1962).

50. Kincaid, B. E., Cowen, S. & Campbell, D. Application of GaAs Lasers and Silicon Avalanche Detectors to Optical Communications. *Optical Engineering* **13,** 389–395 (1974).

51. Yeh, C.-Y., Lu, Z., Froyen, S. & Zunger, A. *Physical Review B* **46,** 10086 (1992).

52. McMahon, M. & Nelmes, R. Observation of a Wurtzite Form of Gallium Arsenide. *Physical Review Letters* **95,** 215505 (2005).

53. Besson, J., Itié, J., Polian, A. & Weill, G. High-pressure phase transition and phase diagram of gallium arsenide. *Physical Review B* **44,** 4214 (1991).

54. Weir, S., Vohra, Y., Vanderborgh, C. & Ruoff, A. Structural phase transitions in GaAs to 108 GPa. *Physical Review B* **39** (1988).

55. Popescu, V. & Zunger, A. Extracting E versus k effective band structure from supercell calculations on alloys and impurities. *Physical Review B* **85,** 085201 (8 Feb. 2012).

56. West, D. & Estreicher, S. K. First-Principles Calculations of Vibrational Lifetimes and Decay Channels: Hydrogen-Related Modes in Si. *Physical Review Letters* **96,** 115504 (11 Mar. 2006).

57. Errea, I., Calandra, M. & Mauri, F. Anharmonic free energies and phonon dispersions from the stochastic self-consistent harmonic approximation: Application to platinum and palladium hydrides. *Physical Review B* **89,** 064302 (6 Feb. 2014).

58. Kim, D. S. *et al.* Nuclear quantum effect with pure anharmonicity and the anomalous thermal expansion of silicon. *Proceedings of the National Academy of Sciences* **115,** 1992–1997 (2018).

59. Herriman, J. E., Hellman, O. & Fultz, B. Phonon thermodynamics and elastic behavior of GaN at high temperatures and pressures. *Physical Review B* **98,** 214105. `https://link.aps.org/doi/10.1103/PhysRevB.98.214105` (21 Dec. 2018).

60. Venkataraman, G., Feldkamp, L. & Sahni, V. *Dynamics of Perfect Crystals* (The MIT Press, 1975).

61. Clatterbuck, D. M., Krenn, C. R., Cohen, M. L. & Morris, J. W. Phonon Instabilities and the Ideal Strength of Aluminum. *Physical Review Letters* **91,** 135501 (13 Sept. 2003).

62. Grimvall, G., Magyari-Köpe, B., Ozolins, V. & Persson, K. A. Lattice instabilities in metallic elements. *Reviews of Modern Physics* **84,** 945–986 (2 June 2012).

63. Lyapin, A. G. & Brazhkin, V. V. Pressure-induced lattice instability and solid-state amorphization. *Physical Review B* **54,** 12036–12048 (17 Nov. 1996).

64. Tong, X. *et al.* Phonons in $\mathbf{Si_{24}}$ at simultaneously elevated temperature and pressure. *Physical Review B* **95,** 094306 (9 Mar. 2017).

65. Novikova, S. I. *Soviet Physics of the Solid State 3,* 129 (1961).

66. Beckstein, O. Elastic Constants How-To (2001). `https://figshare.com/articles/Elastic_Constants_How_To/1164130` (Sept. 2014).